博士學位論文

Dynamic Phase Boundary Estimation Using Electrical Impedance Tomography

濟州大學校 大學院

電氣電子工學科

우머

2007 年 12 月

Dynamic Phase Boundary Estimation Using Electrical Impedance Tomography

指導教授 金 慶 淵

우머

이 論文을 工學 博士學位 論文으로 提出함

2007 年 12 月

우머의 工學 博士學位 論文을 認准함

審查委員長 康 珉 齊 印

委　　員 金 信 印

委　　員 金 珉 澤 印

委　　員 鄭 良 倉 印

委　　員 金 慶 淵 印

濟州大學校 大學院

2007 年 12 月

Dynamic Phase Boundary Estimation Using Electrical Impedance Tomography

Umer Zeeshan Ijaz

(Supervised by Professor Kyung Youn Kim)

A thesis submitted in partial fulfillment of the requirement for the degree of Doctor of Philosophy

2007.12

Department of Electrical and Electronic Engineering
GRADUATE SCHOOL
CHEJU NATIONAL UNIVERSITY

Dedicated to

Norma, Sidrah, and Dada Abu

ACKNOWLEDGEMENTS

The Institute for Information Technology Advancement, Korea were very generous in providing me the assistance under Korean Government IT Scholarship Program. I would like to thank my supervisor, Professor Kyung Youn Kim, for enabling me to undertake these studies, for providing me with interesting and challenging topics, for giving me so much freedom to explore and discover new areas of inverse algorithms, and for making living in a foreign country a happy and unforgettable experience. I would like to thank my co-supervisor, Professor Sin Kim. His classes and weekly meetings have proved to be one of my best learning experiences at Cheju National University. He proved to be a most thorough reviewer, as I expected, and has kept me honest about all the details. Much of the work on forward problem in electrical impedance tomography has been done under his guidance. I would like to offer special thanks to Professor Min Chan Kim who has also helped me a lot in teaching mathematical principles. I would like to express my sincere gratitude to the professors of Department of Electronic Engineering – Professors Yang Hoi Doh, Min Je Kang, Kyung Sik Kim, Kwang Man Lee, Sung Taek Ko, and Suk Joon Ko, for their encouragement and assistance in the duration of my course work.

I have been fortunate enough to have had the support of so many people in the research group without them this thesis would not have been possible – Bong Seok Kim, Jeong Hoon Kim, Anil Kumar Khambampati, Jeong Seong Lee, Soon Il Chung, Ahmar Rashid, Nauman Malik Muhammad, and Santhosh Kumar. Many of us have spent many countless late nights working on projects to meet deadlines and the spirit of our team is truly commendable. Life in Korea has been fruitful with many friends, in particular – Farrukh Aslam Khan, Shafqat-ur-rehman, Li Ying, Pham Minh Anh, Khalid Rehman, Asif Ali Rehmani, Abu Affan, and Safee Ullah Chaudhary.

I would also like to thank my family who have been extremely understanding and supportive of my studies. I feel very lucky to have a grandfather who shares my enthusiasm for academic pursuits. Finally, I would like to thank my wife Norma Javed, for bearing with me when I was too involved in my work, for taking care of me especially in the later part of Ph.D. when I was struggling through my illness, and for giving me the motivation to finish this thesis.

ABBREVIATIONS AND NOTATIONS

CT	Computed tomography
CEM	Complete electrode model
EIT	Electrical impedance tomography
EKF	Extended Kalman filter
EM	Expectation maximization
FEM	Finite element method
IMM	Interacting multiple model
KF	Kalman filter
KM	Kinematic model
LKF	Linearized Kalman filter
MNN	Multi-layered neural network
MRI	Magnetic resonance imaging
N.D.	Norm distinguishability
P.D.	Power distinguishability
GNUKF	Gauss-Newton UKF
GRV	Gaussian random variable
RMSE	Root mean square error
UKF	Unscented Kalman filter
UT	Unscented transform
UST	Ultrasound tomography
WMNN	Weighted multi-layered neural network
α_i, β_i	Parameters in FEM
α_R	Regularization parameter
$\lambda_s, \alpha_s, \kappa_s, \beta_s, \gamma_s$	Scaling parameters in UKF
σ	Conductivity
ρ	Resistivity
ϕ_i	Basis function for *i*'th node in FEM
$\gamma_n^{\alpha_k}$	Truncated Fourier coefficients to be estimated $(\alpha = x, y)$
v	Unit normal
ω	Frequency
ε	Permittivity
μ	Permeability
π_{ij}	Model transition probability between *i*'th and *j*'th model.
μ_k	Model probability
$\mu^{i\|j}$	Mixing probability between *i*'th and *j*'th model
θ_n	Basis function in Fourier coefficients approach
ς	Parameter for generation of trigonometric current patterns
Φ	Cost functional
Ω	Object to be imaged
$\partial\Omega$	Boundary of the object
Λ	Total number of front points to be estimated
χ_k	Characteristic function of the subregion A_k
χ, ψ	Sigma points
Γ_k	Augmented measurement noise covariance matrix

A	Magnetic vector potential, Stiffness matrix
A_k	*k* regions in the domain Ω
b	Unknowns to be solved in FEM
B	Magnetic induction, Component of stiffness matrix
C	Component of stiffness matrix, Open boundary
C^a	Augmented covariance matrix
C_k	Boundary of *k*-th region in the domain Ω, Error covariance matrix
d_λ	Front points to be estimated
D	Electric displacement, Component of stiffness matrix
e_l	*l*'th electrode
E	Electric field, Measurement pattern
f	Force vector containing current patterns
F_k	State transition matrix
I_l^p	Current through the *l*'th electrode at *p*'th pattern
J	Jacobian, Current densitity
J^o, J^s	Components of current density
K_k	Kalman gain
L	Total number of electrodes
L_c	Characteristic distance
L_k	Likelihood function
L_R	Regularization matrix
M	Measurement matrix, Total number of FEM elements
N	Sparse matrix used in FEM, Total number of variables to be estimated
N_d	Number of nodes in FEM
N_r	Number of regions in the domain Ω
N_m	Number of models
N_s	Number of sigma points
N_θ	Order of Fourier series
P	Number of current patterns
$P_\lambda, (X_\lambda, Y_\lambda)$	Discrete front points located on the boundary
Q_k, R_k	Process and measurement noise covariance matrices
R	Radius of pipe
$\tilde{R}$	Pseudo-resistance matrix
S	Number of phase boundaries
$u(x), u$	Potential distribution inside an object
u^h	Finite element approximation of the potential distribution
U^h	Finite element approximation of the voltages on the electrodes
$\hat{U}$	Boundary voltages calculated from the forward solver
$U_k(d_k), U_k(\gamma_k)$	Forward solver
w_k, v_k	White Gaussian process and measurement noises
$W^{(m)}, W^{(c)}$	Weighting matrices for mean and covariance
V	Vector of measured voltages on all electrodes
x^a	Augmented state vector
z_l	Contact impedance between electrolyte and *l*'th electrode

CONTENTS

LIST OF FIGURES

LIST OF TABLES

요약

전기 임피던스 단층촬영법(EIT)에서는, 물체 표면에 부착된 전극을 통하여 다양한 교류전류 패턴을 주입하여 유기된 전압을 측정하여 물체내부의 도전율(conductivity or permittivity) 분포를 추정한다. 전기 임피던스 단층촬영법에서의 영상복원은 비선형 최적화 문제로서 정문제와 역 문제 해법의 반복연산을 통하여 그 해를 구한다. 이때, 내부 도전율과 표면 전압과의 관계는 적당한 경계조건을 갖는 편미분 방정식으로 기술되며, 대부분의 경우에 정 문제에 대한 해석적인 해를 구할 수 없으므로 유한요소 해석법과 같은 수치적인 방법으로 구한다. 전기 임피던스 단층촬영법에서 영상복원 알고리즘은 크게 두 종류로 나눌 수 있는데, 정적 영상 복원법은 모든 측정데이타를 얻는 동안에 내부 도전율 분포가 시 불변인 경우에 사용되며, 이에 반하여 동적 영상 복원법에서는 모든 측정데이타를 얻는 동안에 내부 도전율 분포가 급격히 변하는 경우에 사용된다.

본 논문에서는, 표적의 도전율은 사전에 알고 있고 표적의 위치와 형태를 찾아내는 경계면 추정 기법을 기술한다. 이상혼합 시스템에서 경계면은 퓨리어 급수로 표현되는 닫힌 경계(closed boundary)와 프론트 포인터(front point)로 표현되는 열린 경계(open boundary)로 분류될 수 있는데, 본 논문에서는 두 가지 경우에 있어서 자코비안(Jacobian)을 유도한다. 동적 경계면 추정기법으로써, 칼만 형태(Kalman-type)의 역문제 기법을 이용하고자 하며, 특히 비선형 문제에 대한 확장 칼만필터(extended Kalman filter), 프로세스 공분산의 크기에 따라 여러 개의 모델을 설정한 상호작용 다중모델 (interacting multiple model) 기법, unscented 칼만필터, 그리고 Gauss-Newton unscented 칼만필터를 이용한 경계면 추정기법을 제안한다. 다양한 시나리오에 대한 컴퓨터 시뮬레이션과 팬텀 실험을 통하여 본 논문의 타당성을 확인한다.

INTRODUCTION

Flow of a mixture of two fluids in pipes is of great interest to researchers. The liquid-gas or liquid-vapor mixtures are encountered in condensers and evaporators, gas-liquid reactors, and combustion systems (Holand and Bragg 1995, Perry *et al.* 1997). In some cases, the transport of materials is accomplished by making a slurry of the solid particles in a liquid and pumping the mixture through a pipe. Liquid-liquid mixtures are encountered when dealing with emulsions as well as in liquid-liquid extraction. An example could be two-phase flow that can occur under normal and accidental conditions in various processes such as heat exchange, steam power generation, and oil or natural gas pumping systems.

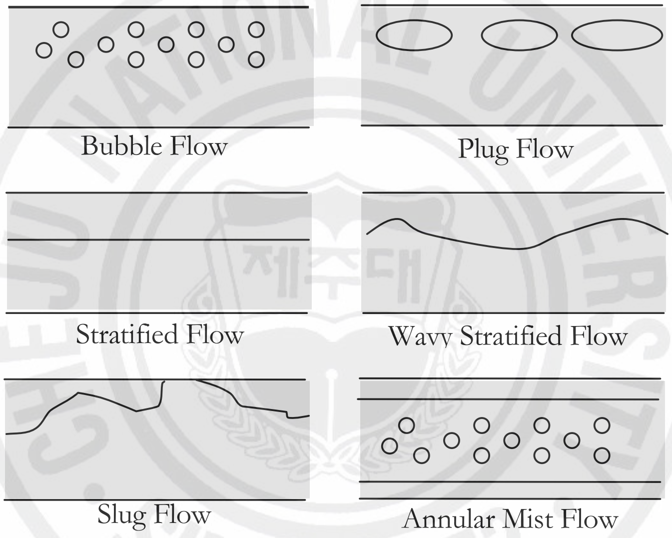

Figure i. Different flow regimes observed with varying velocities in liquid-gas flow.

Another example is the flow of two immiscible liquids in pipelines that are of particular interest in many engineering applications. As a typical example, liquid hydrocarbons transported in pipelines over a long distance (for example, crude oil, gasoline, diesel) often contain free water (Fairuzov 2000). Knowledge of the binary mixture flow is important in the design and operation of such systems. As the heterogeneous phase affects the safety, control, operation, and optimization of the process, it is important to know the phase boundaries online without disturbing the flow fields. For the visualization of two-phase flow, various tomography techniques with noninvasive and nonintrusive characteristics have been developed, for example, gamma densitometry (Shollenberger *et al.* 1997), ultrasonic imaging (Xu *et al.* 1997) and nuclear magnetic resonance imaging (Gladden and Alexander, 1996). Electrical impedance tomography (EIT) has been used quite often in the medical field as an alternative to X-ray imaging, computerized tomography (CT), gamma camera, magnetic resonance imaging (MRI) and ultrasound tomography (UST). Some of these techniques are expensive and even cause adverse health effects. EIT, therefore, has been employed to investigate two-phase flow phenomena (Jones *et al.* 1993) because it is relatively inexpensive and has good temporal resolution. However, it suffers from poor spatial resolution as it has diffusive and soft-field characteristics and this needs to be improved. At the same time, the data acquisition time in EIT is fast which makes it more suitable for fast transient processes.

In EIT, an image of the conductivity or permittivity of part of the body is inferred from surface electrical measurements. Typically, conducting electrodes are attached to the periphery of the subject and small alternating currents are applied to some or all of the electrodes. The resulting electrical potentials are measured and the process is repeated for numerous configurations of applied current. Image reconstruction in EIT is a kind of nonlinear optimization problem in which the solution is obtained iteratively through forward and inverse solvers. The physical relationship between the internal conductivity and surface voltages is governed by a partial differential equation with an appropriate boundary condition. It is, in most cases, impossible to obtain an analytical solution for the forward problem so a numerical technique such as the finite element method (FEM) is employed. Reconstruction algorithms for EIT can be classified into two categories. Firstly, the so-called *static imaging techniques* are used for the case where the internal conductivity of the body is time invariant within the time taken to acquire a full set of measurement data (Yorkey *et al.* 1988). Therefore, these static imaging techniques often fail where there are fast impedance changes. In the other category, there are the so-called *dynamic imaging techniques*, which have been introduced to enhance the temporal resolution for situations where the conductivity distribution inside the body changes rapidly. In these dynamic approaches, the temporal resolution can be improved by a factor of p (p is the number of current patterns in a conventional frame). The reduction in current patterns is also made possible by the analysis of current patterns to use only the optimal current patterns in a dynamic scenario. With regard to optimal current patterns, Isaacson (1988) showed that the best current patterns to distinguish a central concentric inhomogeneity inside an otherwise homogeneous circular conductor are trigonometric current patterns. Gisser *et al.* (1988) compared the distinguishabilities by using adjacent, opposite and cosine current patterns on a circular conductor model without a centered circular target and showed that the maximum cosine current equal to the current injected with the opposite or the adjacent electrode is the optimum current pattern. Newell *et al.* (1988) showed that cosine current patterns can distinguish smaller inhomogeneities as compared to when opposite and adjacent current patterns are used. It is generally known that opposite current patterns are optimal if the total current (sum of the amplitude of the injected currents) is kept constant. With or without using the optimal current patterns (usually the first two modes of cosine and sine patterns), many dynamic techniques were developed in which the inverse problem is treated as a nonlinear state estimation problem and the time-varying state is estimated with the aid of a linearized Kalman filter (LKF) (Vauhkonen 1997, Vauhkonen *et al.* 1998a).

Related work on phase boundary estimation using electrical impedance tomography

Having laid the foundation for two-phase flow estimation and dynamic imaging, a special class of EIT inverse problems is discussed hereafter in which the position and shape of the objects in the domains are unknown and to be identified, while the conductivities of these objects are known *a priori*. There are two types of such problems for binary mixtures according to the topology of the boundary to be estimated: open boundary problems in which the object domain can be divided into two disjoint regions which are separated by an open boundary and closed boundary problems, in which the anomalies are enclosed by the background substance and which are used in this study.

Open boundary estimation problems with EIT have been examined by Butler and Bonnecaze (2000) and by the Kuopio group (Tossavainen *et al.* 2004, 2006). In Butler and Bonnecaze (2000), an open channel filled with conducting liquid was considered and open boundary was imaged with EIT data measured by an array of electrodes at the bottom of the channel. In a two dimensional domain, the height of the liquid and the boundary shape are variable with respect to the horizontal Cartesian coordinate. The boundary was parameterized with Chebyshev polynomials, whose coefficients are the unknowns to be estimated and are embedded implicitly in the coordinate transform from the irregular domain to a square grid. In Tossavainen *et al.* (2004), a pipe which is partially filled with water is considered and has a void region with zero conductivity. The unknown open boundary is parameterized using the mesh nodes and through the coefficients of a Bézier curve. The void region is excluded from the computational domain and the domain boundary varies during the run of iterative inverse solutions. As a consequence, the mesh nodes have to be recalculated at the end of every iteration. It was further assumed that the outermost nodes, excluding those that were present in the free surface, were fixed. Furthermore, the end points of the open boundary are fixed which is not desirable. Recently, Tossavainen *et al.* (2006) proposed improved method for the free surface and admittivity (both conductivity and permittivity) estimation. They used a fixed computational domain without excluding the void region and introduced a constraint to enforce the open boundary to be confined within the object domain. By using this constraint they can eliminate the undesirable fixed-ends assumptions.

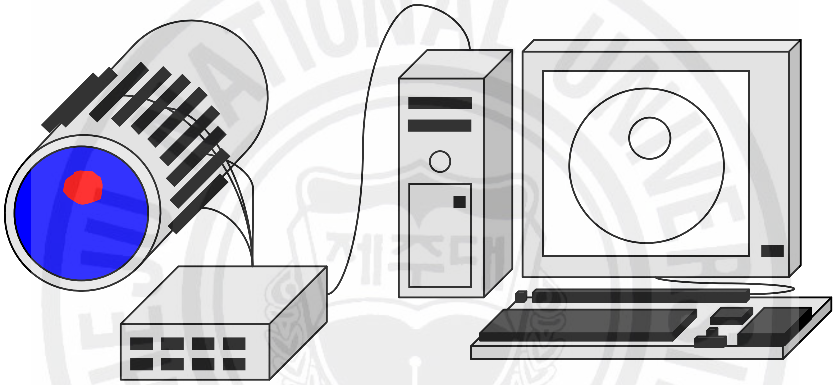

Figure ii. Desired phase boundary estimation system using electrical impedance tomography.

As for closed boundary problems, Han and Prosperetti (1999) considered a shape decomposition technique based on the boundary element method where the boundary of each target was represented in terms of Fourier coefficients rather than a point-wise discretization. Kolehmainen *et al.* (1999) developed an algorithm to recover the region boundaries of piece-wise constant coefficients of an elliptic partial differential equation (PDE) from boundary data for the application to optical tomography, which is also applicable to EIT (Kim *et al.* 2004). For an optimal solution of the Fourier coefficients, a Newton-type method is employed, which is usually time consuming although it shows good performance in many optimization problems. However, its limitation is the slow convergence rate which has an adverse effect on mixture flows undergoing fast transient changes. Jeon *et al.* (2005) estimated the Fourier coefficients with the use of a multi-layered neural network

(MNN) because of its conceptual simplicity, fast online calculation, ease of implementation, ability to control the compromise between the noise treatment and spatial resolution and most importantly, it does not require linearization of the problem (use of first derivative i.e, Jacobian). The neural network used was backpropagation neural network which is regarded as a universal approximator. At the same time, Kim *et al.* (2005) used the exact expression of Jacobian and tested it successfully with experimental data. Kim *et al.* (2006a) improves the performance by considering weighted multilayered neural networks (WMNN), each working together with a different sigmoid function. Since the higher modes of Fourier coefficients are more sensitive to noise so Kim *et al.* (2006b) proposed the use of front points in polar coordinates to estimate the closed boundary. The proposed scheme lacked analytical Jacobian and, therefore, perturbation method was used to estimate the Jacobian matrix. Because of a lack of Jacobian, Kim *et al.* (2006c) used the WMNN to estimate the front points.

Overview of the thesis

In this thesis, the 2D circular geometry in EIT is considered and Kalman-type reconstruction algorithms are applied to estimate dynamic changes in phase boundaries. The Kalman filter is an efficient recursive filter that estimates the *state* (see Gelb, 1974) of a dynamic system from a series of incomplete and noisy measurements. Kalman filtering is an important topic in control theory and control systems engineering and is modelled on a Markov chain, traditionally built on linear operators perturbed by Gaussian noise. In this thesis, the state of the system is represented as a vector of real numbers and represents the variables that model the phase boundary. In order to use the Kalman filter to estimate the internal state of a process given only a sequence of noisy observations (voltage data in this case), one must model the process in accordance with the framework of the Kalman filter. Therefore, in this thesis, finite element method is used to model the process. To date, there exist many variations of the basic Kalman filter (which was essentially based on a linear assumption). However, since most nontrivial systems are nonlinear, therefore, the nonlinearity is adopted in Kalman filter (either in the process model or with the observation model or with both) and hence many implementations appeared over the years. Therefore, in this thesis different types of Kalman-type filters have been investigated that can be used as inverse solvers for phase boundary estimation in electrical impedance tomography. These different implementations are evaluated based on simulated and experimental data. The thesis consists of six chapters.

In Chapter 1, the FEM solution of forward problem using complete electrode model is discussed. After the derivation of FEM solution, the forward solver is modified as a set of coefficients representing the boundary shapes. Two different region boundary representations are used: representation of closed boundary with truncated Fourier coefficients; and representation of open boundary with discrete front points. The Jacobian matrices are derived for both cases. In Chapter 2, the extended Kalman filter is used to recover the front points that represent the interfacial boundary in stratified flows of two immiscible liquids. The results are shown with varying measurement noises, front points and contrast ratio. Additionally, an analysis of current injection protocol is given which is helpful in limiting the number of current patterns to be used in the inverse solver. Chapter 3 introduces interacting multiple model scheme as an inverse algorithm for the recovery of front points and consists of banks of extended Kalman filter each using different process noise covariance model. Chapter 4 discusses different kinematic models for extended Kalman filter. These kinematic models are constructed using first- and second-order Markov models. Four different kinematic models are considered to estimate the shape of air bubbles in conducting medium. Chapter 5 introduces unscented Kalman filter as an improvement over extended Kalman filter. The unscented Kalman filter is based on the unscented transform which is used as a method to propagate mean and covariance information through a nonlinear transformation thus precluding the need to use the jacobian. Chapter 6 considers the Gauss-Newton measurement update in the unscented Kalman filter which improves the performance due to iterative nature of the measurement update.

Chapter 1

1 FORWARD PROBLEM

1.1 Complete electrode model

The behavior of the electromagnetic fields in the domain $\Omega \subset \mathbb{R}^2$ is described with Maxwell's equations. The equation can be written in the form

$$\nabla \times E = -\frac{\partial B}{\partial t} \tag{1.1}$$

$$\nabla \times H = J + \frac{\partial D}{\partial t} \tag{1.2}$$

where E is the electric field, H is magnetic field, B is magnetic induction, D is electric displacement, and J is electric current density.

If the injected currents are time-harmonic with frequency ω, the electric and magnetic field can be written in the form

$$E = \tilde{E}e^{i\omega t}\ ,\ B = \tilde{B}e^{i\omega t} \tag{1.3}$$

In addition, it is assumed that the domain Ω consists of linear and isotropic medium, and so the following relationships hold

$$D = \varepsilon E \tag{1.4}$$

$$B = \mu H \tag{1.5}$$

$$J = \sigma E \tag{1.6}$$

where ε is permittivity, μ is permeability, and σ is the conductivity of the medium.

Using the relations (1.4), (1.5), and (1.6), assuming that the injected currents are time harmonic and canceling out the oscillatory exponential, the equations (1.1) and (1.2) can be written in the form

$$\nabla \times E = -i\omega\mu H \tag{1.7}$$

$$\nabla \times H = J + i\omega\varepsilon E \tag{1.8}$$

Furthermore, the current density is divided into two components $J = J^o + J^s$ where $J^o = \sigma E$ is the so-called ohmic current and J^s denotes the current sources. Thus, equations (1.7) and (1.8) can be written in the form

$$\nabla \times E = -i\omega\mu H \tag{1.9}$$

$$\nabla \times H = (\sigma + i\omega\varepsilon) + J^s \tag{1.10}$$

In EIT some simplifications for these equations are made. The first one is the assumption of static conditions. This means that from the exact derivation of E,

$$E = -\nabla u - \frac{\partial A}{\partial t} \tag{1.11}$$

where u is the electric potential and A is the magnetic vector potential, the later is neglected if it holds that (Nunez 1981)

$$\omega\mu\sigma L_c \left(1 + \frac{\omega\varepsilon}{\sigma}\right) \ll 1 \tag{1.12}$$

which means that the effect of magnetic induction that causes the induced electric field is neglected. Here, L_c is a characteristic distance over which E varies significantly. Another approximation quite often used in EIT is that the capacitive effects $i\omega\varepsilon E$ in (1.8) is neglected using the approximation (Nunez 1981)

$$\frac{\omega\varepsilon}{\sigma} \ll 1 \tag{1.13}$$

With the above approximations the modified Maxwell's equations in linear, isotropic medium under quasistatic conditions are

$$E = -\nabla u \tag{1.14}$$

$$\nabla \times H = \sigma E + J^s \tag{1.15}$$

Taking the divergence on both sides of equation (1.15) and substituting (1.14) into (1.15) the equation

$$\nabla.(\sigma \nabla u) = 0\,,\ x \in \Omega \tag{1.16}$$

for EIT inside the body is obtained. This is true since in the frequency range in EIT $J^s = 0$ inside the body.

There are variety of boundary conditions that can be used in EIT. The most successful of them has been the complete electrode model (CEM) in which the boundary conditions take into account both the shunting effect of the electrodes and the contact impedances between the electrodes and the medium. The boundary conditions for the model can be written as

$$u + z_l \sigma \frac{\partial u}{\partial v} = V_l\,,\ x \in e_l\ ,\ l = 1, 2, \ldots, L \tag{1.17}$$

$$\int_{e_l} \sigma \frac{\partial u}{\partial v} dS = I_l\,,\ x \in e_l\,,\ l = 1, 2, \ldots, L \tag{1.18}$$

$$\sigma \frac{\partial u}{\partial v} = 0\,,\ x \in \partial\Omega \setminus \bigcup_{l=1}^{L} e_l \tag{1.19}$$

where e_l is the *l*th electrode, z_l is the effective contact impedance between the *l*th electrode and medium, V_l are the potentials on the electrodes, I_l are the injected currents, v is the outward unit normal, and L denotes the number of electrodes. Additionally, in order to ensure the existence and uniqueness of the solution u, the following two conditions for the injected currents and measured voltages are needed

$$\sum_{l=1}^{L} I_l = 0 \tag{1.20}$$

$$\sum_{l=1}^{L} V_l = 0 \tag{1.21}$$

1.2 Finite element discretization of the complete electrode model

In this study, the solution of the forward model is based on FEM. Hereafter, the FEM approximation shown for the model has been derived based on Vauhkonen *et al.* (1998b) and considering Somersalo *et al.* (1992).

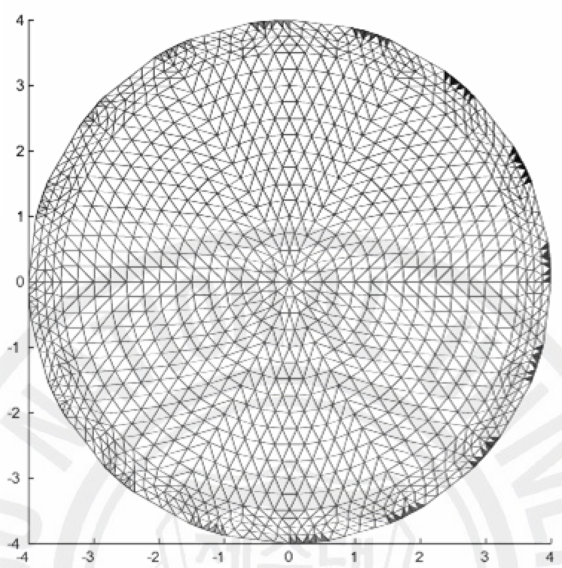

Figure 1.1. The FEM mesh with location of electrodes marked with darkened elements

The *variational* (Galerkin) formulation of the problem is used in the FEM which is also called the *weak form* of the problem. Using this approach, the continuous form of the problem is turned into a discrete formulation using the method of finite elements. In the FEM, the solution domain Ω is first divided into small elements which in this study are triangles (Figure 1.1). The vertices of the triangles are called nodes. Let N_d be the number of nodes in the finite element mesh. The potential u within the object is approximated as

$$u \approx u^h(x) = \sum_{i=1}^{N_d} \alpha_i \varphi_i(x) \tag{1.22}$$

and the potential on the electrodes represented as

$$U^h = \sum_{j=1}^{L-1} \beta_j n_j \tag{1.23}$$

where the function φ_i is the two-dimensional first-order basis function and the bases for the measurement are $n_1 = [1, -1, 0, \ldots, 0]^T$, $n_2 = [1, 0, -1, \ldots, 0]^T$,... $\in \mathbb{R}^L$, etc. That is, the potentials U_l^h on the electrodes are obtained as

$$\begin{aligned}
U_1^h &= \sum_{l=1}^{L-1} \beta_l \\
U_2^h &= -\beta_1 \\
U_3^h &= -\beta_2 \\
&\vdots \\
U_L^h &= -\beta_{L-1}
\end{aligned} \tag{1.24}$$

This can be written in the matrix form as

$$U^h = N\beta \tag{1.25}$$

where $N \in \mathbb{R}^{L\times(L-1)}$ is a sparse matrix such that

$$N = (n_1, n_2, ..., n_{L-1}) = \begin{bmatrix} 1 & 1 & \cdots & 1 \\ -1 & 0 & \cdots & 0 \\ 0 & -1 & \cdots & 0 \\ \vdots & \vdots & \ddots & \vdots \\ 0 & 0 & \cdots & -1 \end{bmatrix} \tag{1.26}$$

The choice for n_j's ensures that the condition of equation (1.21) is fulfilled. The linear equation obtained from the finite element formulation $Ab = f$ is constructed such that

$$b = \begin{pmatrix} \alpha \\ \beta \end{pmatrix} \in \mathbb{R}^{N_d + L - 1} \tag{1.27}$$

$$A = \begin{pmatrix} B & CN \\ (CN)^T & N^T DN \end{pmatrix} \in \mathbb{R}^{(N_d + L - 1)\times(N_d + L - 1)} \tag{1.28}$$

$$\tilde{I} = \begin{pmatrix} 0 \\ N^T \hat{I} \end{pmatrix} \in \mathbb{R}^{N_d + L - 1} \tag{1.29}$$

where $0=(0,\ldots,0)^T \in \mathbb{R}^{N_d}$, $\hat{I}=(I_1-I_2, I_1-I_3, \ldots I_1-I_L)^T \in \mathbb{R}^{L-1}$, $\alpha=(\alpha_1,\ldots,\alpha_{N_d})^T$ and $\beta=(\beta_1,\ldots,\beta_{L-1})^T$. The elements of the system matrix A (Vauhkonen, 1997) are

$$B(i,j)=\int_\Omega \sigma\nabla\varphi_i.\nabla\varphi_j dr+\sum_{l=1}^{L}\frac{1}{z_l}\int_{e_l}\varphi_i\varphi_j dS\ ,\ \ i,j=1,2,\ldots,N_d \tag{1.30}$$

$$C(i,j)=-\left(\frac{1}{z_l}\int_{e_1}\varphi_i dS-\frac{1}{z_{j+1}}\int_{e_{j+1}}\varphi_i dS\right),\ \begin{matrix} i=1,2,\ldots,N_d \\ j=1,2,\ldots,L-1\end{matrix} \tag{1.31}$$

$$\begin{aligned} D(i,j) &= \sum_{l=1}^{L}\frac{1}{z_l}\int_{e_l}(n_i)_l(n_j)_l\, dS \\ &= \begin{cases} \dfrac{|e_1|}{z_1}, & i\neq j \\ \dfrac{|e_1|}{z_1}+\dfrac{|e_{j+1}|}{z_{j+1}}, & i=j \end{cases}\ ,\ i,j=1,2,\ldots,L-1 \end{aligned} \tag{1.32}$$

where $|e_j|$ is the measure (length) of the *j*th electrode.

1.3 Representation of region boundaries

In this study the recovery of sufficiently smooth region boundaries is considered. The assumption made is that the conductivity profile is known *a priori*, but the information about the geometry and shape is missing. This leads to a nonlinear and ill-posed inverse problem in which the coefficients representing the boundary shape are the unknowns to be estimated. Therefore, the forward solver has to be modified as a set of coefficients representing the boundary shapes to the data on $\partial\Omega$. Two types of boundary regions are considered: closed boundary and open boundary (also known as *free surface*) as illustrated in Figure 1.2.

Lets assume that the region Ω is divided into disjoint, simply connected domains A_k

$$\Omega=\bigcup_{k=0}^{N_r}A_k \tag{1.33}$$

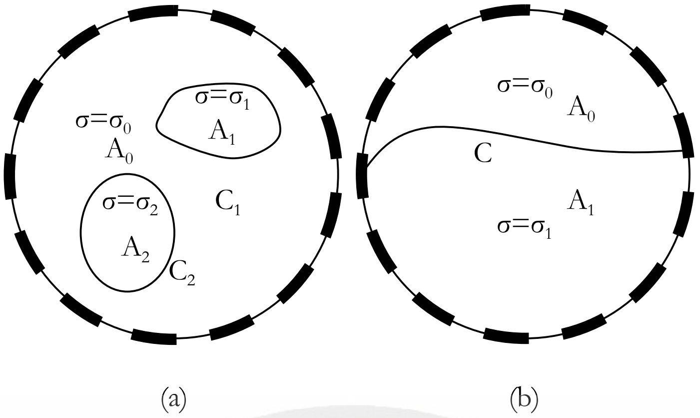

Figure 1.2. Examples of smooth region boundaries: (a) regions with closed boundaries; and (b) open boundary between regions.

where $k = 0,1$ for open boundary representation and up to N_r regions exist in closed boundary representation. Assuming the region boundaries in closed boundary strategy is represented by C_k and in open boundary by C, denoting by $\chi_k(r)$ the characteristic function of subregion A_k, we can write

$$\sigma = \sum_{k=0}^{N_r} \sigma_k \chi_k(r) \tag{1.34}$$

By substituting (1.34) into (1.30), we obtain

$$B(i,j) = \sum_{k=0}^{N_r} \int_{\mathrm{supp}(\varphi_i\varphi_j)\cap A_k} \sigma_k \nabla\varphi_i \nabla\varphi_j dr + \sum_{l=1}^{L} \frac{1}{z_l} \int_{e_l} \varphi_i \varphi_j dS \tag{1.35}$$

where $\mathrm{supp}(\varphi_i\varphi_j)$ is the part of domain Ω where both the basis function φ_i and φ_j are non-zero. The implementation of the integrals of the form (1.35) has been described previously in Kolehmainen *et al.* (1999) and Tossavainen *et al.* (2006).

In the first step, the mesh elements Ω_m are classified to sets of elements inside the region $A_k\,(k = 0,1)$ and to the set of elements intercepted by the boundary C_k. For the elements that lie in the region A_k, they are assigned their corresponding conductivity values σ_k, however for the elements that lie on the boundary C_k, the area weighted conductivity values are assigned as (Kolehmainen *et al.* 1999)

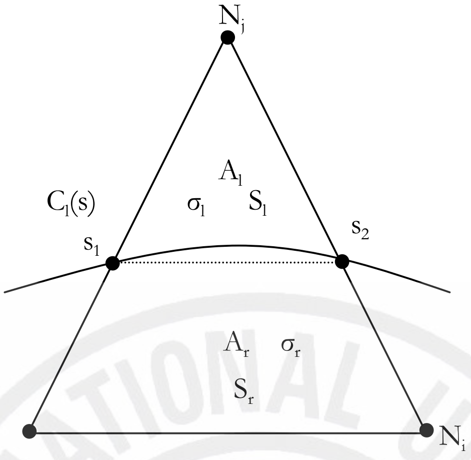

Figure 1.3. A schematic representation of FEM element Ω_e intercepted by the phase boundary $C_l(s)$.

$$\sigma_e = \frac{\sigma_l S_l + \sigma_r S_r}{S_e (= S_l + S_r)} \tag{1.36}$$

1.3.1 *Phase boundary representation with discrete front points*

Let us suppose a stratified flow of two immiscible liquids through a circular pipe of radius R as shown in Figure 1.4. The open boundary between two immiscible liquids is approximated as an interpolation with discrete front points P_λ, $\lambda = 1, 2, \ldots, \Lambda$, located on the boundary. The total number of the front points is Λ. P_1 and P_Λ are the leftmost and rightmost front points, respectively, i.e., they are on the outer boundary of the object. The front point is parameterized in terms of d_λ. For the front points inside the object $(\lambda = 2, \ldots, \Lambda - 1)$, d_λ is simply defined as the vertical distance from the corresponding reference point $(x_\lambda, 0)$ located on the central horizon and the coordinate of P_λ is $(X_\lambda, Y_\lambda) = (x_\lambda, d_\lambda)$, where the reference points are predetermined and known. For the end front points, on the other hand, d_λ cannot be defined in the same manner. Instead, d_1 and d_Λ are defined as the path lengths along the outer boundary from the reference points $(x_1, 0) = (-R, 0)$ and $(x_\Lambda, 0) = (R, 0)$, respectively. With this definition, both end front points are confined to the outer boundary. In essence, the front points are expressed in terms of d_λ, the parameter to be estimated:

$$(X_1, Y_1) = \left(-R\cos\frac{d_1}{R}, R\sin\frac{d_1}{R}\right)$$

$$(X_\lambda, Y_\lambda) = (x_\lambda, d_\lambda)\,,\ \lambda = 2, \ldots, \Lambda - 1 \qquad (1.37)$$

$$(X_\Lambda, Y_\Lambda) = \left(R\cos\frac{d_\Lambda}{R}, R\sin\frac{d_\Lambda}{R}\right)$$

The unknown parameter is then written in the form

$$d = (d_1, d_2, \ldots, d_\Lambda)^T \in \mathbb{R}^{\Lambda\times 1} \qquad (1.38)$$

1.3.1.1 Calculation of Jacobian

In order to complete the procedure to estimate the unknown state variables d_λ, $(\lambda = 1, 2, \ldots, \Lambda)$, the Jacobian should be formulated. In some cases, the voltages are measured only at some selected electrodes, not every electrode. Also, the selected electrodes may be different at each current pattern. The measured voltages at the measurement electrodes $\hat{U}$ can thus be obtained as

$$\hat{U} = M^T U^h = M^T N\beta \in \mathbb{R}^{E\times P} \qquad (1.39)$$

where E is the number of the measurement electrodes, P is the number of current patterns, and $M \in \mathbb{R}^{L\times E}$ is the measurement matrix. The element $M(l, p)$ is set to '1' if the *l*'th electrode is measured at the *p*'th current pattern and otherwise set to zero. Furthermore, U^h can be extracted directly from b by introducing the extended maping matrix $\tilde{N}$,

$$\tilde{N} = (0, N) \in \mathbb{R}^{L\times(N_d+L-1)} \text{ and } U^h = \tilde{N}b \qquad (1.40)$$

where $0 \in \mathbb{R}^{L\times N_d}$. Therefore, we have

$$\hat{U} = M^T U^h = M^T \tilde{N}b = \tilde{M}b = \tilde{M}A^{-1}\tilde{I} \qquad (1.41)$$

where the extended measurement matrix is defined as

$$\tilde{M} = M^T \tilde{N} \in \mathbb{R}^{E\times(N_d+L-1)} \tag{1.42}$$

If the pseudo-resistance matrix defined as

$$\tilde{R} = A^{-1}\tilde{M}^T \in \mathbb{R}^{(N_d+L-1)\times E} \text{ or } A\tilde{R} = \tilde{M}^T \tag{1.43}$$

is given we can calculate the Jacobian matrix. The pseudo-resistance matrix can be easily obtained by the solution of the system equation

$$A\begin{pmatrix} \tilde{R} & b \end{pmatrix} = \begin{pmatrix} \tilde{M}^T & \tilde{I} \end{pmatrix} \tag{1.44}$$

or

$$A\begin{pmatrix} \tilde{R}_1 & \alpha \\ \tilde{R}_2 & \beta \end{pmatrix} = \begin{pmatrix} 0 & 0 \\ N^T M & N^T \tilde{I} \end{pmatrix} \tag{1.45}$$

where

$$\tilde{R}_1 = \tilde{R}(1:N_d,:) \in \mathbb{R}^{N_d\times E} \text{ and}$$

$$\tilde{R}_2 = \tilde{R}(N_d+1:N_d+L-1,:) \in \mathbb{R}^{(L-1)\times E} \tag{1.46}$$

The Jacobian $\partial\hat{U}/\partial d_\lambda \quad (\lambda = 1,2,\ldots,\Lambda)$ will be

$$\frac{\partial \hat{U}}{\partial d_\lambda} = -\tilde{M}A^{-1}\frac{\partial A}{\partial d_\lambda}A^{-1}\tilde{I} = -\tilde{R}^T\frac{\partial A}{\partial d_\lambda}b \tag{1.47}$$

due to the symmetry of the stiffness matrix A. In A, the matrix B is the only term dependent on d_λ and the Jacobian will be

$$\frac{\partial \hat{U}}{\partial d_\lambda} = -\begin{pmatrix} \tilde{R}_1 \\ \tilde{R}_2 \end{pmatrix}^T \begin{pmatrix} \frac{\partial B}{\partial d_\lambda} & 0 \\ 0 & 0 \end{pmatrix}\begin{pmatrix} \alpha \\ \beta \end{pmatrix} = -\begin{pmatrix} \tilde{R}_1^T & \tilde{R}_2^T \end{pmatrix}\begin{pmatrix} \frac{\partial B}{\partial d_\lambda}\alpha \\ 0 \end{pmatrix}$$

$$= -\tilde{R}_1^T \frac{\partial B}{\partial d_\lambda}\alpha \tag{1.48}$$

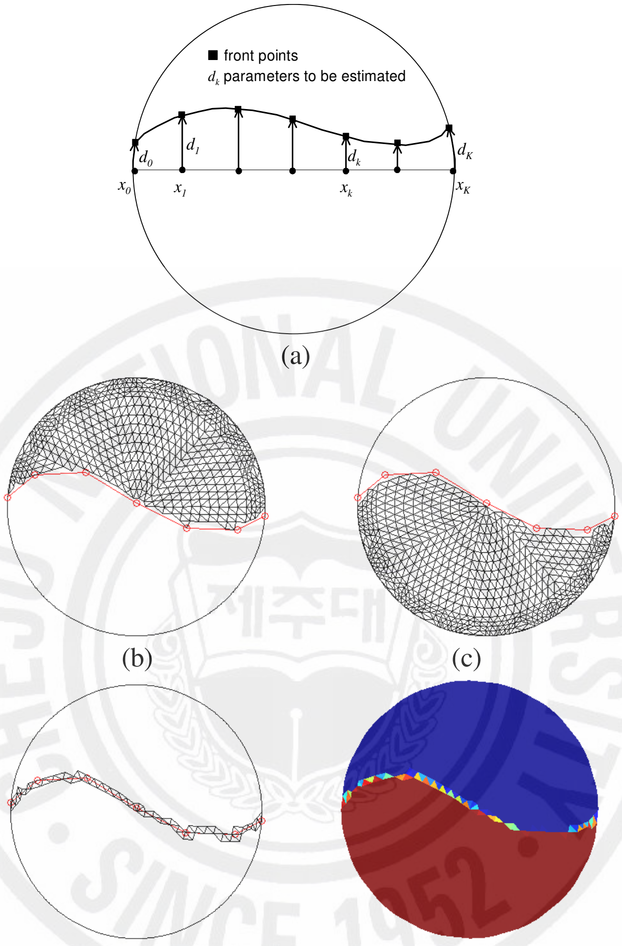

(a)

(b) (c)

(d) (e)

Figure 1.4. Problem representation: (a) description of interface with front points; (b) mesh elements above the interface are assigned σ_u; (c) mesh elements below the interface are assigned σ_l; (d) mesh elements lying on the interface are assigned area average conductivity values assigned using equation (1.36); and (e) final conductivity values at the end of assignment.

From (1.37) the derivative $\partial B/\partial d_\lambda$ is written as

$$\frac{\partial B}{\partial d_1} = \frac{\partial B}{\partial X_1}\frac{\partial X_1}{\partial d_1} + \frac{\partial B}{\partial Y_1}\frac{\partial Y_1}{\partial d_1} = \frac{Y_1}{R}\frac{\partial B}{\partial X_1} - \frac{X_1}{R}\frac{\partial B}{\partial Y_1}$$

$$\frac{\partial B}{\partial d_\lambda} = \frac{\partial B}{\partial Y_\lambda}\,,\ \lambda = 2,\ldots,\Lambda - 1 \tag{1.49}$$

$$\frac{\partial B}{\partial d_\Lambda} = -\frac{Y_\Lambda}{R}\frac{\partial B}{\partial X_\Lambda} + \frac{X_\Lambda}{R}\frac{\partial B}{\partial Y_\Lambda}$$

Since we are considering a stratified flow of two immiscible liquids with distinct electrical properties, so the matrix B will be

$$B(i,j) = \sum_{r=l,u} \sigma_r \int_{A_r} \nabla\varphi_i.\nabla\varphi_j d\Omega + \sum_{l=1}^{L}\frac{1}{z_l}\int_{e_l}\varphi_i\varphi_j dS\,,\ i,j = 1,2,\ldots,N_d \tag{1.50}$$

where the subscripts l and u denote the lower and the upper region, respectively (see Figure 1.4). The derivative $\partial B/\partial d_\lambda$ can then be obtained as

$$\frac{\partial B}{\partial d_\lambda} = \lim_{\delta d_\lambda \to 0}\frac{B(X_\lambda + \delta X_\lambda, Y_\lambda + \delta Y_\lambda) - B(X_\lambda, Y_\lambda)}{\delta d_\lambda}$$

$$= \lim_{\delta d_\lambda \to 0}\frac{(\sigma_l - \sigma_u)}{\delta d_\lambda}\sum_{m|\Omega_m \subset \mathrm{supp}(\varphi_i\varphi_j)}\int_{\delta A_u \cap \Omega_m}\nabla\varphi_i.\nabla\varphi_j d\Omega \tag{1.51}$$

Assuming that the interface C is represented by a set of piecewise linear interpolation functions:

$$C(x) = \sum_{\lambda=2}^{\Lambda} S_\lambda(x)\chi(x, X_{\lambda-1}, X_\lambda)\,,\ x \in [X_1, X_\Lambda] \tag{1.52}$$

where

$S_\lambda(x) = \dfrac{Y_\lambda - Y_{\lambda-1}}{X_\lambda - X_{\lambda-1}}(x - X_{\lambda-1}) + Y_{\lambda-1}$, $\lambda = 2,\ldots,\Lambda$ and $\chi(x, X_{\lambda-1}, X_\lambda)$ is a unit pulse defined for $x \in [X_{\lambda-1}, X_\lambda]$. An arbitrary small perturbation of δd_λ results in a small perturbation δX_λ in X_λ and δY_λ in Y_λ, which will cause a small change in the interface for $x \in [X_{\lambda-1}, X_{\lambda+1}]$.

$$\delta C_1(x) = \delta S_2(x)\chi(x, X_1, X_2) + O(\delta^2)$$

$$\delta C_{\lambda}(x) = \delta S_{\lambda}(x)\chi(x, X_{\lambda-1}, X_{\lambda}) + \delta S_{\lambda+1}(x)\times\chi(x, X_{\lambda}, X_{\lambda+1}) + O(\delta^2)\,, \lambda = 2, \ldots, \Lambda-1$$

$$\delta C_{\Lambda}(x) = \delta S_{\Lambda}(x)\chi(x, X_{\Lambda-1}, X_{\Lambda}) + O(\delta^2) \tag{1.53}$$

where

$$\delta S_{\lambda}(x) = \left(-\frac{Y_{\lambda} - Y_{\lambda-1}}{X_{\lambda} - X_{\lambda-1}} \delta X_{\lambda} + \delta Y_{\lambda} \right) \frac{x - X_{\lambda-1}}{X_{\lambda} - X_{\lambda-1}}\,,\ x \in [X_{\lambda-1}, X_{\lambda}]$$

$$\delta S_{\lambda+1}(x) = \left(-\frac{Y_{\lambda+1} - Y_{\lambda}}{X_{\lambda+1} - X_{\lambda}} \delta X_{\lambda} + \delta Y_{\lambda} \right) \frac{X_{\lambda+1} - x}{X_{\lambda+1} - X_{\lambda}}\,,\ x \in [X_{\lambda}, X_{\lambda+1}] \tag{1.54}$$

Now let us consider the evaluation of expression (1.51) for interface-crossing meshes Ω_m such that $\Omega_m \subset \mathrm{supp}(\varphi_i \varphi_j)$:

$$\lim_{\delta d_{\lambda} \to 0} \frac{1}{\delta d_{\lambda}} \int_{\delta A_u \cap \Omega_m} f(x, y) d\Omega \tag{1.55}$$

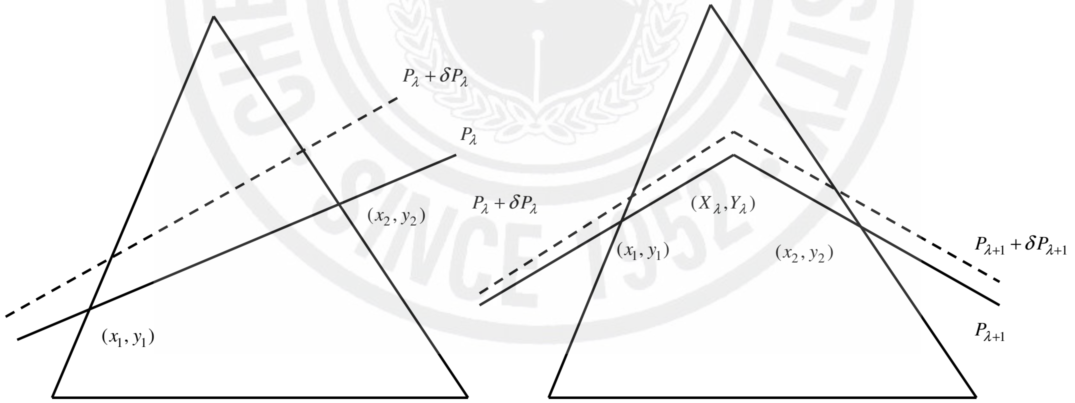

Figure 1.5. Perturbation in the interface when the interface-crossing mesh does not contain any front points (left) and when the mesh contains $(X_{\lambda}, Y_{\lambda})$ (right).

where $f(x, y) = \nabla\varphi_i . \nabla\varphi_j$. For a small perturbation in d_{λ}, only $P_{\lambda}(x)$ and $P_{\lambda+1}(x)$ will change (see Figure 1.5) and the above expression will be

$$\lim_{\delta d_\lambda \to 0} \frac{1}{\delta d_\lambda} \int_{\delta A_u \cap \Omega_m} f(x,y)\, d\Omega$$

$$= \lim_{\delta d_\lambda \to 0} \frac{1}{d_\lambda} \int_{X_{\lambda-1}}^{X_{\lambda+1}} \int_{C}^{C+\delta C_\lambda} f(x,y)\, dy\, dx \tag{1.56}$$

The function $f(x,y)$ can be expanded about the interface $C(x)$,

$$f(x,y) = f(x,C) + \left.\frac{\partial f}{\partial y}\right|_{y=C} (y-C) + O(\delta^2) \tag{1.57}$$

Inserting (1.57) into (1.56), finally we have

$$\lim_{\delta d_\lambda \to 0} \frac{1}{\delta d_\lambda} \int_{\delta A_u \cap \Omega_m} f(x,y)\, d\Omega$$

$$= -\frac{1}{R}\left(\frac{Y_2-Y_1}{X_2-X_1}Y_1 + X_1\right) \int_{X_1}^{X_2} f(x,C) \frac{X_2-x}{X_2-X_1}\, dx, \text{ for } \lambda = 1$$

$$= \int_{X_{\lambda-1}}^{X_\lambda} f(x,C) \frac{x-X_{\lambda-1}}{X_\lambda - X_{\lambda-1}}\, dx + \int_{X_\lambda}^{X_{\lambda+1}} f(x,C) \frac{X_{\lambda+1}-x}{X_{\lambda+1}-X_\lambda}\, dx, \text{ for } \lambda = 2,\dots,\Lambda-1$$

$$= \frac{1}{R}\left(\frac{Y_\Lambda - Y_{\Lambda-1}}{X_\Lambda - X_{\Lambda-1}} Y_\Lambda + X_\Lambda\right) \int_{X_{\Lambda-1}}^{X_\Lambda} f(x,C) \frac{x-X_{\Lambda-1}}{X_\Lambda - X_{\Lambda-1}}\, dx, \text{ for } \lambda = \Lambda \tag{1.58}$$

There are five types of interface-crossing elements when Y_λ is perturbed by an arbitrarily small perturbation of δY_λ. Assume that there are only two intersections of the interface and the mesh faces and the intersections are denoted as (x_1, y_1) and (x_2, y_2) where $x_1 < x_2$. Recalling that $f(x,y) = \nabla\phi_i \cdot \nabla\phi_j$ is constant in a certain mesh, the integration for each type will be evaluated as

Type 1. $$f(x,C) \int_{X_{\lambda-1}}^{x_2} \frac{x-X_{\lambda-1}}{X_\lambda - X_{\lambda-1}}\, dx = \frac{f(x,C)}{2} \frac{\left(x_2 - X_{\lambda-1}\right)^2}{X_\lambda - X_{\lambda-1}} \tag{1.59}$$

Type 2. $$f(x,C) \int_{x_1}^{x_2} \frac{x-X_{\lambda-1}}{X_\lambda - X_{\lambda-1}}\, dx = \frac{f(x,C)}{2} \frac{\left(x_2 - X_{\lambda-1} + x_1 - X_{\lambda-1}\right)\left(x_2 - x_1\right)}{X_\lambda - X_{\lambda-1}} \tag{1.60}$$

Type 3.
$$f(x,C)\left[\int_{x_1}^{X_\lambda}\frac{x-X_{\lambda-1}}{X_\lambda-X_{\lambda-1}}dx+\int_{X_\lambda}^{x_2}\frac{X_{\lambda+1}-x}{X_{\lambda+1}-X_\lambda}dx\right] = \frac{f(x,C)}{2}\left[\frac{(X_\lambda-X_{\lambda-1}+x_1-X_{\lambda-1})(X_\lambda-x_1)}{X_\lambda-X_{\lambda-1}}+\frac{(X_{\lambda+1}-x_2+X_{\lambda+1}-X_\lambda)(x_2-X_\lambda)}{X_{\lambda+1}-X_\lambda}\right] \quad (1.61)$$

Type 4.
$$f(x,C)\int_{x_1}^{x_2}\frac{X_{\lambda+1}-x}{X_{\lambda+1}-X_\lambda}dx=\frac{f(x,C)}{2}\frac{(X_{\lambda+1}-x_2+X_{\lambda+1}-x_1)(x_2-x_1)}{X_{\lambda+1}-X_\lambda} \quad (1.62)$$

Type 5.
$$f(x,C)\int_{x_1}^{X_{\lambda+1}}\frac{X_{\lambda+1}-x}{X_{\lambda+1}-X_\lambda}dx=\frac{f(x,C)}{2}\frac{(X_{\lambda+1}-x_1)^2}{X_{\lambda+1}-X_\lambda} \quad (1.63)$$

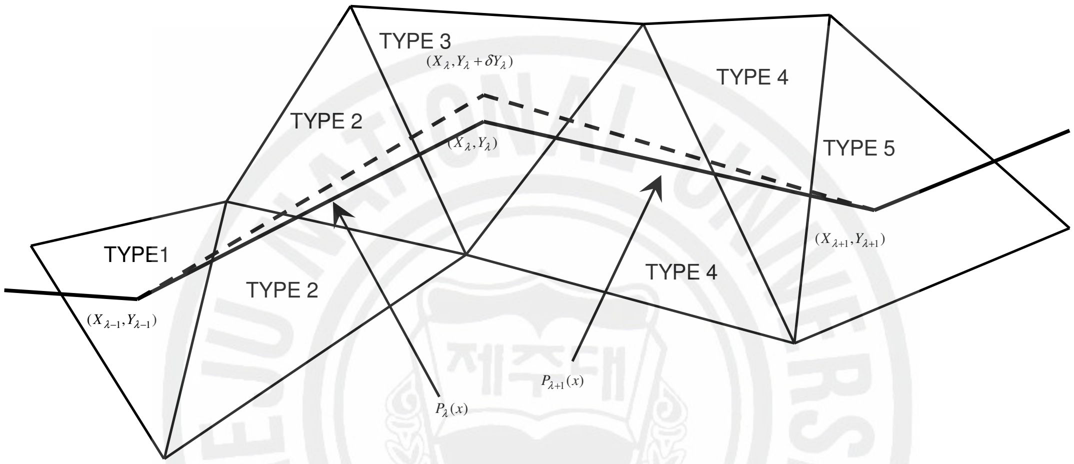

Figure 1.6. Five types of interface-crossing elements in case of an arbitrarily small perturbation of δY_λ in Y_λ.

1.3.2 Phase boundary representation with truncated Fourier coefficients

In the case where a sufficiently smooth inhomogeneity is enclosed by a surrounding medium, truncated Fourier series can be used to represent the phase boundaries $\{C_l, l=1,2,...,S\}$ as

$$C_l(s)=\begin{pmatrix} x_l(s) \\ y_l(s)\end{pmatrix}=\sum_{n=1}^{N_\theta}\begin{pmatrix}\gamma_n^{x_l}\theta_n^x(s) \\ \gamma_n^{y_l}\theta_n^y(s)\end{pmatrix},\ l=1,2,...,S \quad (1.64)$$

where N_θ and S denote the order of truncated Fourier series and the number of phase boundaries, respectively, and $\theta_n(s)$ is the periodic and smooth basis function. In this thesis we express both coordinates of the curve as the truncated Fourier series with respect to the curve parameter s, that is, we use basis function of the form

$$\theta_0^{\alpha} = 1$$

$$\theta_{2n-1}^{\alpha} = \sin(2n\pi s)\,,\ n = 1, 2, \ldots \tag{1.65}$$

$$\theta_{2n}^{\alpha} = \cos(2n\pi s)\,,\ n = 1, 2, \ldots$$

where $s \in [0,1]$, and α denotes either x or y. Furthermore, using the expansion of equations (1.64) and (1.65), the boundaries $\{C_l\}$ can be identified with the vector γ of the shape coefficients, that is,

$$\gamma = \left(\gamma_1^{x_1}, \ldots, \gamma_{N_\theta}^{x_1}, \gamma_1^{y_1}, \ldots, \gamma_{N_\theta}^{y_1}, \ldots, \gamma_{N_\theta}^{y_\Lambda}, \gamma_1^{y_\Lambda}, \ldots, \gamma_{N_\theta}^{y_\Lambda}\right) \in \mathbb{R}^{2\Lambda N_\theta} \tag{1.66}$$

1.3.2.1 *Calculation of Jacobian*

The Jacobian is defined as the relative change of the measured voltage at the *l*'th measurement electrode at the *p*'th current pattern ($\hat{U}_\ell^p$) with respect to the change of the *n*'th coefficient of the *k*'th boundary ($\gamma_n^{\alpha_k}, \alpha = x, y$), that is

$$J_{\ell p \alpha_k n} = \frac{\partial \hat{U}_\ell^p}{\partial \gamma_n^{\alpha_k}} \tag{1.67}$$

or in the matrix form

$$J = \begin{pmatrix}
\frac{\partial \hat{U}_1^1}{\partial \gamma_1^{x_1}} & \cdots & \frac{\partial \hat{U}_1^1}{\partial \gamma_{N_\theta}^{x_1}} & \frac{\partial \hat{U}_1^1}{\partial \gamma_1^{y_1}} & \cdots & \frac{\partial \hat{U}_1^1}{\partial \gamma_{N_\theta}^{y_1}} & \cdots & \frac{\partial \hat{U}_1^1}{\partial \gamma_1^{x_K}} & \cdots & \frac{\partial \hat{U}_1^1}{\partial \gamma_{N_\theta}^{x_K}} & \frac{\partial \hat{U}_1^1}{\partial \gamma_1^{y_K}} & \cdots & \frac{\partial \hat{U}_1^1}{\partial \gamma_{N_\theta}^{y_K}} \\
\vdots & \cdots & \vdots & \vdots & \cdots & \vdots & \cdots & \vdots & \cdots & \vdots & \vdots & \cdots & \vdots \\
\frac{\partial \hat{U}_E^1}{\partial \gamma_1^{x_1}} & \cdots & \frac{\partial \hat{U}_E^1}{\partial \gamma_{N_\theta}^{x_1}} & \frac{\partial \hat{U}_E^1}{\partial \gamma_1^{y_1}} & \cdots & \frac{\partial \hat{U}_E^1}{\partial \gamma_{N_\theta}^{y_1}} & \cdots & \frac{\partial \hat{U}_E^1}{\partial \gamma_1^{x_K}} & \cdots & \frac{\partial \hat{U}_E^1}{\partial \gamma_{N_\theta}^{x_K}} & \frac{\partial \hat{U}_E^1}{\partial \gamma_1^{y_K}} & \cdots & \frac{\partial \hat{U}_E^1}{\partial \gamma_{N_\theta}^{y_K}} \\
\vdots & \cdots & \vdots & \vdots & \cdots & \vdots & \cdots & \vdots & \cdots & \vdots & \vdots & \cdots & \vdots \\
\frac{\partial \hat{U}_1^P}{\partial \gamma_1^{x_1}} & \cdots & \frac{\partial \hat{U}_1^P}{\partial \gamma_{N_\theta}^{x_1}} & \frac{\partial \hat{U}_1^P}{\partial \gamma_1^{y_1}} & \cdots & \frac{\partial \hat{U}_1^P}{\partial \gamma_{N_\theta}^{y_1}} & \cdots & \frac{\partial \hat{U}_1^P}{\partial \gamma_1^{x_K}} & \cdots & \frac{\partial \hat{U}_1^P}{\partial \gamma_{N_\theta}^{x_K}} & \frac{\partial \hat{U}_1^P}{\partial \gamma_1^{y_K}} & \cdots & \frac{\partial \hat{U}_1^P}{\partial \gamma_{N_\theta}^{y_K}} \\
\vdots & \cdots & \vdots & \vdots & \cdots & \vdots & \cdots & \vdots & \cdots & \vdots & \vdots & \cdots & \vdots \\
\frac{\partial \hat{U}_E^P}{\partial \gamma_1^{x_1}} & \cdots & \frac{\partial \hat{U}_E^P}{\partial \gamma_{N_\theta}^{x_1}} & \frac{\partial \hat{U}_E^P}{\partial \gamma_1^{y_1}} & \cdots & \frac{\partial \hat{U}_E^P}{\partial \gamma_{N_\theta}^{y_1}} & \cdots & \frac{\partial \hat{U}_E^P}{\partial \gamma_1^{x_K}} & \cdots & \frac{\partial \hat{U}_E^P}{\partial \gamma_{N_\theta}^{x_K}} & \frac{\partial \hat{U}_E^P}{\partial \gamma_1^{y_K}} & \cdots & \frac{\partial \hat{U}_E^P}{\partial \gamma_{N_\theta}^{y_K}}
\end{pmatrix} \tag{1.68}$$

The Jacobian matrix can be obtained from the derivative of the system of equation

$$\frac{\partial \hat{U}}{\partial \gamma_n^{\alpha_k}} = \tilde{M}\,\frac{\partial b}{\partial \gamma_n^{\alpha_k}} = \tilde{M}\,\frac{\partial}{\partial \gamma_n^{\alpha_k}}\left(A^{-1}\tilde{I}\right) = \tilde{M}\,\frac{\partial A^{-1}}{\partial \gamma_n^{\alpha_k}}\,\tilde{I}$$

$$\frac{\partial A^{-1}}{\partial \gamma_n^{\alpha_k}}\,\tilde{I} = -A^{-1}\,\frac{\partial A}{\partial \gamma_n^{\alpha_k}}\,A^{-1}\tilde{I} = -A^{-1}\,\frac{\partial A}{\partial \gamma_n^{\alpha_k}}\,b$$

$$\frac{\partial \hat{U}}{\partial \gamma_n^{\alpha_k}} = -\tilde{M}A^{-1}\,\frac{\partial A}{\partial \gamma_n^{\alpha_k}}b = -\left((A^{-1})^T\,\tilde{M}^T\right)^T\,\frac{\partial A}{\partial \gamma_n^{\alpha_k}}b = -\left(A^{-1}\tilde{M}^T\right)^T\,\frac{\partial A}{\partial \gamma_n^{\alpha_k}}b \tag{1.69}$$

In the last equality, $(A^{-1})^T = A^{-1}$ is used because of the symmetry of the stiffness matrix. If the pseudo-resistance matrix defined as

$$\tilde{R} = A^{-1}\tilde{M}^T \in \Re^{(N_d+L-1)\times E} \ \text{ or } \ A\tilde{R} = \tilde{M}^T \tag{1.70}$$

is given, we can calculate the Jacobian matrix. The pseudo-resistance matrix can be easily obtained during the solution of the system equation

$$A\begin{pmatrix}\tilde{R} & b\end{pmatrix} = \begin{pmatrix}\tilde{M}^T & \tilde{I}\end{pmatrix} \tag{1.71}$$

or

$$A\begin{pmatrix}\tilde{R}_1 & \alpha \\ \tilde{R}_2 & \beta\end{pmatrix} = \begin{pmatrix}0 & 0 \\ N^T M & N^T\hat{I}\end{pmatrix} \tag{1.72}$$

where

$$\tilde{R}_1 = \tilde{R}(1:N_d,:) \in \Re^{N_d\times E} \ \text{ and } \ \tilde{R}_2 = \tilde{R}(N_d+1:N_d+L-1,:) \in \Re^{(L-1)\times E} \tag{1.73}$$

The derivative of the system matrix with respect to the coefficients is

$$\frac{\partial A}{\partial \gamma_n^{\alpha_k}} = \begin{pmatrix}\dfrac{\partial B}{\partial \gamma_n^{\alpha_k}} & 0 \\ 0 & 0\end{pmatrix} \tag{1.74}$$

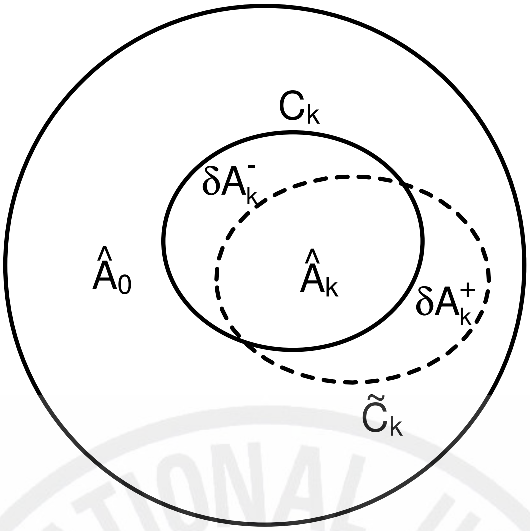

Figure 1.7. Perturbation in the interface.

where

$$\begin{aligned}
\frac{\partial B}{\partial \gamma_n^{x_k}} &= \lim_{\varepsilon \to 0} \frac{B(x_k + \varepsilon \gamma_n^{x_k}, y_k) - B(x_k, y_k)}{\varepsilon} \\
&= \lim_{\varepsilon \to 0} \frac{1}{\varepsilon} \left[\sigma_0 \int_{\tilde{A}_0} (\bullet)\, d\Omega + \sigma_k \int_{\tilde{A}_k} (\bullet)\, d\Omega - \sigma_0 \int_{A_0} (\bullet)\, d\Omega - \sigma_k \int_{A_k} (\bullet)\, d\Omega \right] \\
&= \lim_{\varepsilon \to 0} \frac{1}{\varepsilon} \left[\sigma_0 \int_{\hat{A}_0 + \delta A_k^-} (\bullet)\, d\Omega + \sigma_k \int_{\hat{A}_k + \delta A_k^+} (\bullet)\, d\Omega - \sigma_0 \int_{\hat{A}_0 + \delta A_k^+} (\bullet)\, d\Omega - \sigma_k \int_{\hat{A}_k + \delta A_k^-} (\bullet)\, d\Omega \right] \\
&= \lim_{\varepsilon \to 0} \frac{(\sigma_k - \sigma_0)}{\varepsilon} \int_{\delta A_k^+ - \delta A_k^-} (\bullet)\, d\Omega = \lim_{\varepsilon \to 0} \frac{(\sigma_k - \sigma_0)}{\varepsilon} \sum_{m|\Omega_m \in \operatorname{supp}(\phi_i \phi_j)} \int_{\delta A_k \cap \Omega_m} (\bullet)\, d\Omega
\end{aligned}$$

$$\frac{\partial B}{\partial \gamma_n^{x_k}} = \lim_{\varepsilon \to 0} \frac{(\sigma_k - \sigma_0)}{\varepsilon} \sum_{m|\Omega_m \in \operatorname{supp}(\phi_i \phi_j)} \int_{\delta A_k \cap \Omega_m} \nabla \phi_i \cdot \nabla \phi_j \, d\Omega \tag{1.75}$$

where $\operatorname{supp}(\phi_i \phi_j)$ denotes the part of the domain Ω where both basis functions ϕ_i and ϕ_j are non-zero. That is, $\sum_{m|\Omega_m \in \operatorname{supp}(\phi_i \phi_j)} \delta A_k \cap \Omega_m$ is the union of the elements crossing the boundary of A_k. $\tilde{A}_k$ and $\tilde{C}_k$ denote the *k*'th region and its boundary after the perturbation (see Figure 1.7), respectively. Also, $\hat{A}_k = \tilde{A}_k \cap A_k$, $\delta A_k^- = A_k - \tilde{A}_k$, $\delta A_k^+ = \tilde{A}_k - A_k$ and $\delta A = \delta A^+ - \delta A^-$.

In order to obtain the Jacobian, let us consider the evaluation of the expression

$$\lim_{\varepsilon \to 0} \frac{1}{\varepsilon} \int_{\delta A_k \cap \Omega_m} f(x, y) d\Omega \tag{1.76}$$

We define a new coordinate system (s, p) where s is the positively oriented coordinate along the closed curve C_k, and p is the coordinate outward normal from the region A_k

$$\begin{pmatrix} p \\ s \end{pmatrix} \mapsto \begin{pmatrix} x_k(s) \\ y_k(s) \end{pmatrix} + p \begin{pmatrix} \xi(s) \\ \eta(s) \end{pmatrix} = \begin{pmatrix} x(s) \\ y(s) \end{pmatrix} \tag{1.77}$$

The perturbed boundary $\tilde{C}_k$ will be

$$s \mapsto \begin{pmatrix} x_k(s) \\ y_k(s) \end{pmatrix} + \varepsilon \begin{pmatrix} \xi(s) \\ \eta(s) \end{pmatrix} = \begin{pmatrix} \tilde{x}_k(s) \\ \tilde{y}_k(s) \end{pmatrix} = \tilde{C}_k(s) \tag{1.78}$$

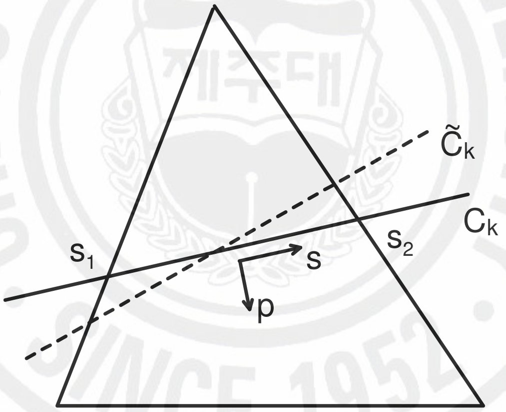

Figure 1.8. Coordinate transformation.

Therefore,

$$\lim_{\varepsilon \to 0} \frac{1}{\varepsilon} \int_{\delta A_k \cap \Omega_m} f(x, y) d\Omega = \lim_{\varepsilon \to 0} \frac{1}{\varepsilon} \int_{s=s_1}^{s_2} \int_{p=0}^{\varepsilon} f(x, y) \frac{\partial(x, y)}{\partial(p, s)} dpds \tag{1.79}$$

The Jacobian for the transformation of the coordinates will be

$$\frac{\partial(x,y)}{\partial(p,s)}=\begin{vmatrix}\frac{\partial x}{\partial p} & \frac{\partial x}{\partial s}\\ \frac{\partial y}{\partial p} & \frac{\partial y}{\partial s}\end{vmatrix}=\begin{vmatrix}\xi & \frac{dx}{ds}+p\frac{d\xi}{ds}\\ \eta & \frac{dy}{ds}+p\frac{d\eta}{ds}\end{vmatrix}=\xi\left(\dot{y}+p\dot{\eta}\right)-\eta\left(\dot{x}+p\dot{\xi}\right) \tag{1.80}$$

The dot denotes the derivative with respective to s. The function $f(x,y)$ can be expanded about the boundary C_k

$$f(x,y)=f(p,s)=f(0,s)+\left.\frac{\partial f}{\partial p}\right|_{p=0}p+O(p^2) \tag{1.81}$$

We have

$$\begin{aligned}&\lim_{\varepsilon\to 0}\frac{1}{\varepsilon}\int_{\delta A_k\cap\Omega_m} f(x,y)d\Omega\\ &=\lim_{\varepsilon\to 0}\frac{1}{\varepsilon}\int_{s=s_1}^{s_2}\int_{p=0}^{\varepsilon}\left[f(0,s)+\left.\frac{\partial f}{\partial p}\right|_{p=0}p+O(p^2)\right]\left[\xi\left(\dot{y}+p\dot{\eta}\right)-\eta\left(\dot{x}+p\dot{\xi}\right)\right]dpds\\ &=\int_{s=s_1}^{s_2}f(0,s)\left(\xi\dot{y}-\eta\dot{x}\right)ds\end{aligned} \tag{1.82}$$

In this, $f(0,s)$ is evaluated at the boundary C_k. When differentiating with respect to $\gamma_n^{x_k}$, that is perturbing $\theta_n^x(s)$, we have $\xi=\theta_n^x(s)$ and $\eta=0$. On the other hand, when differentiating with respect to $\gamma_n^{y_k}$, we have $\xi=0$ and $\eta=\theta_n^y(s)$. Finally, the derivative of the matrix with respect to the coefficients becomes

$$\frac{\partial B}{\partial\gamma_n^{x_k}}=(\sigma_k-\sigma_0)\sum_{m|\Omega_m\in B(C_k)\cap\sup p(\phi_i\phi_j)}\int_{s_1}^{s_2}\nabla\phi_i\cdot\nabla\phi_j\Big|_{x,y\in C_k}\dot{y}_k(s)\theta_n^x(s)ds \tag{1.83}$$

$$\frac{\partial B}{\partial\gamma_n^{y_k}}=-(\sigma_k-\sigma_0)\sum_{m|\Omega_m\in B(C_k)\cap\sup p(\phi_i\phi_j)}\int_{s_1}^{s_2}\nabla\phi_i\cdot\nabla\phi_j\Big|_{x,y\in C_k}\dot{x}_k(s)\theta_n^y(s)ds \tag{1.84}$$

where

$$B(C_k)=\left\{\Omega_m\mid\Omega_m\cap C_k\neq\emptyset\right\} \tag{1.85}$$

denotes the set of elements crossing C_k. If $\nabla\phi_i \cdot \nabla\phi_j$, $\dot{x}_k(s)$ and $\dot{y}_k(s)$ are constant in each mesh, we have

$$\frac{\partial B}{\partial \gamma_n^{x_k}} = (\sigma_k - \sigma_0) \sum_{m|\Omega_m \in B(C_k) \cap \mathrm{supp}(\phi_i \phi_j)} \nabla\phi_i \cdot \nabla\phi_j \Big|_{\Omega_m} \frac{y(s_2) - y(s_1)}{s_2 - s_1} \int_{s_1}^{s_2} \theta_n^x(s)ds \tag{1.86}$$

$$\frac{\partial B}{\partial \gamma_n^{y_k}} = -(\sigma_k - \sigma_0) \sum_{m|\Omega_m \in B(C_k) \cap \mathrm{supp}(\phi_i \phi_j)} \nabla\phi_i \cdot \nabla\phi_j \Big|_{\Omega_m} \frac{x(s_2) - x(s_1)}{s_2 - s_1} \int_{s_1}^{s_2} \theta_n^y(s)ds \tag{1.87}$$

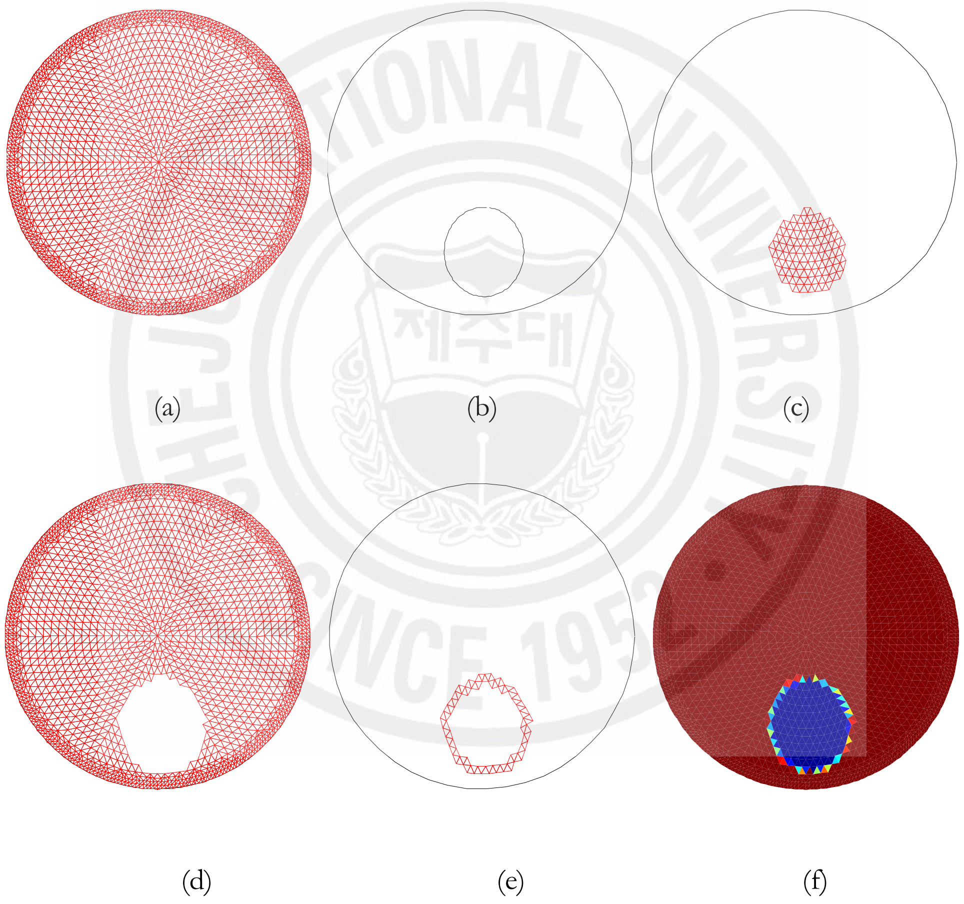
(a) (b) (c)

(d) (e) (f)

Figure 1.9. Fourier coefficients mapping to conductivity profile: (a) FEM discretization of the domain; (b) boundary represented by Fourier coefficients; (c) mesh elements belonging to target are assigned σ_l; (d) mesh elements belonging to the background are assigned σ_r; (e) mesh elements lying on the interface are assigned area average conductivity values assigned using equation (1.36); and (f) final conductivity values at the end of assignment.

Finally, from (1.69) and (1.70), the Jacobian will be obtained as

$$\frac{\partial \hat{U}}{\partial \gamma_n^{\alpha_k}} = -\begin{pmatrix} \tilde{R}_1 \\ \tilde{R}_2 \end{pmatrix}^T \begin{pmatrix} \frac{\partial B}{\partial \gamma_n^{\alpha_k}} & 0 \\ 0 & 0 \end{pmatrix} \begin{pmatrix} \alpha \\ \beta \end{pmatrix} = -\begin{pmatrix} \tilde{R}_1^T & \tilde{R}_2^T \end{pmatrix} \begin{pmatrix} \frac{\partial B}{\partial \gamma_n^{\alpha_k}} \alpha \\ 0 \end{pmatrix} = -\tilde{R}_1^T \frac{\partial B}{\partial \gamma_n^{\alpha_k}} \alpha \tag{1.88}$$

where $\tilde{R}_1^T \in \Re^{E \times N_d}$, $B \in \Re^{N_d \times N_d}$, and $\alpha \in \Re^{N_d \times P}$.

1.4 Current injection methods

In all the EIT systems, the currents are injected and voltages are measured instead of the other way around due to the fact that the contact impedance has negligible effect on voltage measurements since voltmeters have a large input impedance whereas ammeters have very small input impedance (Vauhkonen 1996). There are different types of current injection protocols that produce the most uniform sensitivity and therefore the most accurate images (discussed in Chapter 2). Perhaps the most widely used data collection method is the so-called *adjacent method* in which the current is injected through two adjacent electrodes and the voltage differences are measured from all other pair of electrodes. The adjacent method produces nonuniform current densitiy since most of the injected currents travels near the boundary. This has a low sensitivity in the center of the object. Another method is the *opposite method* in which current is injected through diametrically opposed electrodes. The voltages are measured with respect to one reference electrode adjacent to the current electrode. The advantage of the opposite method is the more uniform current density and hence good sensitivity. A combination of the above two methods is called *cross method.* In the context of this thesis, the so-called *trigonometric current patterns* (Isaacson 1986) are used most of the time in which the current through the *l*'th electrode at *p*'th pattern is

$$I_l^p = \begin{cases} I_0 \cos(p\varsigma_l), & p = 1, 2, \ldots, L/2 \\ I_0 \sin(p\varsigma_l), & 1, 2, \ldots, L/2 - 1 \end{cases} \tag{1.89}$$

where $\varsigma_l = 2\pi l / L$. These are the best current patterns to distinguish a central circular inhomogeneity inside an otherwise homogeneous circular conductor.

1.5 Performance evaluation criteria

In this thesis, root mean square error (RMSE) is used to evaluate the performance of different approaches. It is a frequently-used measure of the difference between values predicted by a model or an estimator and the values actually observed from the thing being modeled or estimated. The RMSE for the parameter *d*, $RMSE_d$, is defined as

$$RMSE_d = \frac{\| d_{estimated} - d_{true} \|}{\| d_{true} \|} \tag{1.90}$$

The RMSE for the parameter γ, $RMSE_\gamma$, is defined as

$$RMSE_\gamma = \frac{\| \gamma_{estimated} - \gamma_{true} \|}{\| \gamma_{true} \|} \tag{1.91}$$

The RMSE for the boundary voltages, $RMSE_U$, is defined as

$$RMSE_U = \frac{\| U_{estimated} - U_{meas} \|}{\| U_{meas} \|} \tag{1.92}$$

2 DYNAMIC INTERFACIAL BOUNDARY ESTIMATION USING EXTENDED KALMAN FILTER

2.1 Optimization problem for boundary parameter estimation

In this chapter, we lay down the foundation for open boundary estimation problem to find the parameter d minimizing the measured and the calculated boundary voltages in a minimum least square sense. The EIT problem needs regularization due to its ill-posedness and hence the objective functional to be minimized is expressed as

$$\Phi = \frac{1}{2} \| U_{meas} - U(d) \|^2 + \frac{\alpha_R}{2} \| L_R (d - d^*) \|^2 \tag{2.1}$$

where U_{meas} denotes the measured boundary voltage data, α_R is a regularization parameter, L_R is a regularization operator, and d^* denotes the referenced parameter vector.

2.2 Extended Kalman filter model

The estimation of the interfacial boundary in stratified flows of two immiscible liquids is considered and it is natural that the interfacial boundary varies continuously during the time taken to collect a full set of independent EIT measurement data. If the interface deforms significantly within the data collection time for a single frame of image, the image reconstruction performance will deteriorate and the conventional static image reconstruction will not be applicable. In order to enhance the temporal resolution of EIT, Kalman filter approaches have been widely accepted (Vauhkonen *et al.* 1998a, Kim *et al.* 2001, Trigo *et al.* 2004). The unknown conductivity distribution or boundary shape is regarded as state variables, and then the EIT problem is transformed into a state estimation problem. In this work, the front point locations are treated as state variables, which are tracked by EKF.

We are considering the estimation of the parameter $d \in \mathbb{R}^{\Lambda \times 1}$ of a discrete-time controlled process that is governed by the linear stochastic difference equation

$$d_k = F_{k-1} d_{k-1} + w_{k-1} \tag{2.2}$$

with a measured voltage $V \in \mathbb{R}^E$ that is

$$V_k = U_k(d_k) + v_k \tag{2.3}$$

where the subscript k is the state index, $F_k \in \mathbb{R}^{\Lambda \times \Lambda}$ is the state transition model and U_k is the observation model. E is the number of measurement electrodes. The random variables $w_k \in \mathbb{R}^{\Lambda \times 1}$ and $v_k \in \mathbb{R}^{E \times 1}$ denote the process and the measurement noise, respectively. They are assumed to be independent of each other, white and with normal probability distribution

$$p(w_k) \sim N(0, Q_k) \tag{2.4}$$

$$p(v_k) \sim N(0, R_k) \tag{2.5}$$

where $Q_k \in \mathbb{R}^{\Lambda \times \Lambda}$ and $R_k \in \mathbb{R}^{E \times E}$ are the process and the measurement noise covariances, respectively. We linearize the observation model about *a priori* state estimate at step k, $d_{k|k-1}$:

$$\begin{aligned} V_k &= U_k(d_{k|k-1}) + \left.\frac{\partial U_k}{\partial d_k}\right|_{d_{k|k-1}} (d_k - d_{k|k-1}) + v_k + HOT \\ &= V_{k|k-1} + J_k(d_k - d_{k|k-1}) + v_k + HOT \end{aligned} \tag{2.6}$$

where $V_{k|k-1} = U_k(d_{k|k-1})$ is the *a priori* measurement estimate. The higher order terms are denoted by 'HOT'. The Jacobians $J_k \in \mathbb{R}^{E \times \Lambda}$ will be defined as

$$J_k = \left.\frac{\partial U_k}{\partial d_k}\right|_{d_{k|k-1}} \tag{2.7}$$

Let us define the pseudo measurement equation $y_k \in \mathbb{R}^{E \times 1}$

$$y_k \equiv V_k - U_k(d_{k|k-1}) + J_k d_{k|k-1} = J_k d_k + \overline{v}_k \tag{2.8}$$

where $\overline{v}_k \in \mathbb{R}^E$ is the pseudo measurement noise

$$\overline{v}_k = v_k + HOT \tag{2.9}$$

with zero mean and known covariance $\overline{R}_k \in \mathbb{R}^{E \times E}$

$$E[\bar{v}_k] = 0 \text{ and } \bar{R}_k = \mathrm{cov}(v_k + HOT) \tag{2.10}$$

The second equality in equation (2.8) is from equation (2.6). The *a priori* state estimate at step *k* given knowledge of the process up to step *k-1*, $d_{k|k-1}$, and the pseudo measurement estimate at step *k*, $y_{k|k}$, will be

$$\begin{aligned} d_{k|k-1} &= E[d_k \mid y_{k-1}] = E[F_{k-1} d_{k-1} + w_k \mid y_{k-1}] = F_{k-1} E[d_{k-1} \mid y_{k-1}] \\ &= F_{k-1} d_{k-1|k-1} \end{aligned} \tag{2.11}$$

$$y_{k|k} = E[y_k \mid d_k] = E[J_k d_k + \tilde{v}_k \mid d_k] = J_k d_{k|k} \tag{2.12}$$

The predicted error $e_{k|k-1} \in \mathbb{R}^{M\times 1}$ and its covariance $C_{k|k-1} \in \mathbb{R}^{\Lambda\times\Lambda}$ will be

$$e_{k|k-1} = d_k - d_{k|k-1} = F_{k-1} e_{k-1|k-1} + w_{k-1} \tag{2.13}$$

$$C_{k|k-1} = \mathrm{cov}(e_{k|k-1}) = F_{k-1} C_{k-1|k-1} F_{k-1}^T + Q_{k-1} \tag{2.14}$$

Let the updated state estimate $d_{k|k}$ be the state maximizing the probability density d_k given y_k,

$$p\left(d_k \mid y_k\right) \sim p\left(d_k \mid y_{k-1}\right) p\left(y_k \mid d_k\right) \tag{2.15}$$

or can also be represented by minimizing the following functional that corresponds to the exponent of the probability density function

$$\begin{aligned} \Phi(d_k) &= \frac{1}{2}(d_k - d_{k|k-1})^T C_{k|k-1}^{-1} (d_k - d_{k|k-1}) \\ &\quad + \frac{1}{2}(y_k - J_k d_k)^T \tilde{R}_k^{-1} (y_k - J_k d_k) \\ &= \frac{1}{2}\left\| d_k - d_{k|k-1} \right\|_{C_{k|k-1}^{-1}} + \frac{1}{2}\left\| y_k - J_k d_k \right\|_{\tilde{R}_k^{-1}} \end{aligned} \tag{2.16}$$

where $\|x\|_R = x^T R x$. In this, regularization should be considered in the construction of the functional as given in (2.1)

$$\Phi(d_k) = \frac{1}{2}\left\| d_k - d_{k|k-1} \right\|_{C_{k|k-1}^{-1}} + \frac{1}{2}\left\| y_k - J_k d_k \right\|_{\tilde{R}_k^{-1}} + \frac{\alpha_R}{2}\left\| L_R(d_k - d^*) \right\| \tag{2.17}$$

If we define the augmented pseudo measurement $\tilde{y}_k \in \mathbb{R}^{(E+\Lambda)\times 1}$ and the augmented pseudo observation matrix $H_k \in \mathbb{R}^{(E+\Lambda)\times\Lambda}$ as

$$\tilde{y}_k = \begin{pmatrix} y_k \\ \sqrt{\alpha_R}\, L_R d^* \end{pmatrix} \tag{2.18}$$

$$H_k = \begin{pmatrix} J_k(d_{k|k-1}) \\ \sqrt{\alpha_R}\, L_R \end{pmatrix} \tag{2.19}$$

then the cost functional can be arranged as

$$\Phi(d_k) = \frac{1}{2} \| d_k - d_{k|k-1} \|_{C_{k|k-1}^{-1}} + \frac{1}{2} \| \tilde{y}_k - H_k d_k \|_{\Gamma_k^{-1}} \tag{2.20}$$

The augmented measurement model can be written as

$$\tilde{y}_k = H_k d_k + \gamma_k \tag{2.21}$$

where the augmented measurement noise $\gamma_k \in \mathbb{R}^{(E+\Lambda)\times 1}$ is assumed to be zero-mean and its covariance $\Gamma_k \in \mathbb{R}^{(E+\Lambda)\times(E+\Lambda)}$ is a block diagonal matrix defined by

$$\Gamma_k = Blockdiag[\bar{R}_k, I_\Lambda] \tag{2.22}$$

if $\bar{R}_k$ is a diagonal matrix. Then, by differentiating $\Phi(d_k)$ with respect to d_k and setting it to zero the procedure to estimate the state variable is established and the procedure is summarized as follows:

Step 1. Predicted (*a priori*) state

$$d_{k|k-1} = F_{k-1} d_{k-1|k-1} \tag{2.23}$$

Step 2. Predicted (*a priori*) error covariance

$$C_{k|k-1} = \mathrm{cov}(e_{k|k-1}) = F_{k-1}C_{k-1|k-1}F_{k-1}^{T} + Q_{k-1}\,. \tag{2.24}$$

Step 3. Predicted measurement error

$$\varepsilon_k = \tilde{y}_k - \tilde{y}_{k|k-1} = \tilde{y}_k - H_k d_{k|k-1} \tag{2.25}$$

Step 4. Predicted measurement error covariance

$$S_k = \mathrm{cov}(\varepsilon_k) = H_k C_{k|k-1} H_k^T + \Gamma_k \tag{2.26}$$

Step 5. Kalman gain

$$K_k = C_{k|k-1} H_k^T S_k^{-1} \tag{2.27}$$

Step 6. Updated (*a posteriori*) state

$$d_{k|k} = d_{k|k-1} + K_k \varepsilon_k = d_{k|k-1} + K_k(\tilde{y}_k - H_k d_{k|k-1}) \tag{2.28}$$

Step 7. Updated *(a posteriori*) error covariance

$$C_{k|k} = \left(I - K_k H_k\right) C_{k|k-1} \tag{2.29}$$

2.3 Numerical results for front points

For the verification of the proposed model, numerical experiments have been conducted. It is assumed that a stratified flow of two conducting immiscible liquids with distinct electrical properties flows through a cylindrical pipe of diameter $28cm$. The pipe is equipped with 16 electrodes of width $2.5cm$ each around its periphery. The conductivity of each region is assumed to be known and initially set to $1/(600\Omega cm)$ for the upper region and $1/(300\Omega cm)$ for the lower region.

As for the regularization, we simply use the standard Tikhonov method where $L_R = I \in \mathbb{R}^{\Lambda\times\Lambda}$ and $d^* = 0$. Proper choice of the regularization parameter α_R is a very difficult problem. While there are rational ways to choose the regularization parameter (e.g. L-curve), the so-called trial-and-error method may have practical significance (Lionheart 2004). In this work

α_R is chosen *a posteriori* by trial-and-error method. The regularization parameter depends on the noise level of the measured boundary voltages.

The state transition model equation (2.2), F_k, in the Kalman filter approach should be deduced from the dynamics of the state variables, the shape of the interfacial boundary in the present problem. In general, however, prior knowledge on the flow dynamics is often unknown unless flow variables are sufficiently available to estimate the flow dynamics. Therefore, this work adopts the so-called *random-walk* model in which $F_k = I_\Lambda \in \mathbb{R}^{\Lambda\times\Lambda}$. In the simulations, the covariance matrices of the process noise Q and the measurement noise $\bar{R}$ should be predetermined and are listed in Table 2.1. Also the initial covariance of the predicted error $C_{0|0} \in \mathbb{R}^{\Lambda\times\Lambda}$ is set to $I_\Lambda \in \mathbb{R}^{\Lambda\times\Lambda}$. If the process model is known, then the covariance Q can be estimated. However, the true process model is not known *a priori* and this parameter should be determined by trial and error. The measurement noise covariance R can be estimated if the measurement noise and the discretization error in the FEM model are given. Furthermore, the linearization error should also be included in the pseudo measurement noise covariance $\bar{R}$ in equation (2.10). So, it does not seem to be possible to determine $\bar{R}$ quantitatively. The usual way to select the magnitude of $\bar{R}$ is the trial-and-error method. Quantitatively, however, the magnitude of $\bar{R}$ depends on the boundary voltages, namely the system resistance, so that the covariance $\bar{R}$ tends to increase as the system resistance increases.

The data collection method plays an important role in better image reconstruction. A multi-referenced current injection pattern is recommended to achieve good sensitivity for arbitrary unknown conductivity distribution (Webster 1990). In this context, a detailed design of the data collection method for stratified flows would be an interesting topic. As reported in Tossavainen *et al.* (2006), the use of reference electrode located near the interfacial boundary and the concentration of electric currents on the boundary will enhance the sensitivity significantly. Since this work is concerned with the reconstruction of a moving boundary, it is assumed that the boundary varies significantly within the time taken to acquire the full set of current-voltage data to obtain a single image in the framework of the conventional static EIT. In the case of trigonometric current injection with 16 electrodes, 15 current injections and voltage measurements are used for a single static image. The present simulation assumes that only four current injections and voltage measurements are available when there is no change in the shape of the interfacial boundary, whereas for static image reconstruction, the entire independent current patterns of 15 should be used. In the trigonometric pattern (1.89), the sensitivity decreases as p increases, therefore, only the first two patterns each of sine and cosine patterns ($p = 1, 2$) are used for better sensitivity. Here, it is worth mentioning that an optimal design of the data collection method for the estimation of the interfacial boundary in stratified flows under transient is an interesting topic which we will discuss shortly.

In the numerical experiments, two different types of mesh structures are used to avoid the inverse crime. The simulated experimental data are calculated by discretizing the cross-section of the flow area into 2088 triangular meshes with 1109 nodes, while for the image reconstruction a slightly coarser mesh structure with 1968 triangular elements and 1049 nodes is used. When the synthesized data are generated, on the other hand, the interfacial boundary is described with the cubic spline. In the image reconstruction, the interfacial boundary is approximated with piecewise linear interpolation functions. The use of different descriptions of the interface will support the freedom from the inverse crime.

Table 2.1. Parameters for the extended Kalman filter for scenario 1 when the contrast ratio is 2:1.

Parameters	Noise		
	1% white Gaussian Noise	2% white Gaussian Noise	3% white Gaussian Noise
Q	$0.01I_\Lambda$	$0.01I_\Lambda$	$0.01I_\Lambda$
$\tilde{R}$	$200I_E$	$400I_E$	$600I_E$
$C_{0\|0}$	I_Λ	I_Λ	I_Λ
α_R	0.0001	0.01	0.01

Table 2.2. Parameters for the extended Kalman filter for scenario 1 for various contrast ratios with 1% noise.

Parameters	Contrast Ratio			
	5:1	10:1	100:1	1000:1
Q	$0.01I_\Lambda$	$0.01I_\Lambda$	$0.01I_\Lambda$	$0.01I_\Lambda$
$\tilde{R}$	$500I_E$	$3\times10^3 I_E$	$4\times10^4 I_E$	$5\times10^6 I_E$
$C_{0\|0}$	I_Λ	I_Λ	I_Λ	$150I_\Lambda$
α_R	0.0001	0.0001	0.0001	0.0001

Table 2.3. Parameters for the extended Kalman filter for scenario 2 when the constrast ratio is 100.

Parameters	Noise		
	1% white Gaussian Noise	2% white Gaussian Noise	3% white Gaussian Noise
Q	$0.01I_\Lambda$	$0.01I_\Lambda$	$0.01I_\Lambda$
$\tilde{R}$	$9\times10^4 I_E$	$10\times10^4 I_E$	$11\times10^4 I_E$
$C_{0\|0}$	$0.01I_\Lambda$	$0.01I_\Lambda$	$0.01I_\Lambda$
α_R	0.00001	0.0001	0.0001

We consider a scenario (scenario 1) in which the interface fairly flat in the beginning varies with time and becomes wavy eventually. The left and right end points of the interfacial boundary are not fixed and should be estimated by the inverse solver. The interface is estimated with seven front points. Numerical experiments have been conducted with various number of front points: five onwards and increasing by two. It was found that front points not less than 11 tend to deteriorate the image reconstruction performance and that seven is a good choice. Scenario 1 consists of 30 frames of images and the evolution of the interface is depicted in Figure 2.1.

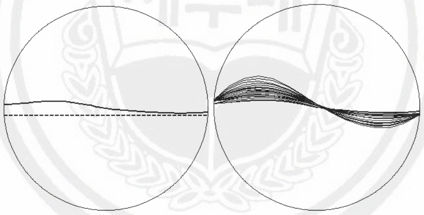

Figure 2.1. Description of the interfacial boundary movement in scenario 1 where the left part of the interface is moving up and the other part is moving down. The left profile describes the true (solid line) and the guessed (dotted line) initial boundary, respectively. The right profile shows the evolution of the interface.

The reconstructed interfacial boundaries are obtained with synthesized data contaminated by white Gaussian noise of levels 1%, 2%, and 3%, respectively. The numerical values used in the simulation are reported in Table 2.1. It is assumed that the interface is stationary during the time taken to inject four current patterns and to measure resultant boundary voltages. However, in the reconstruction, five states per single frame of image are used. The additional fifth state is updated based on the first cosine pattern in (1.89), and is repeated in the reconstruction. Namely, five consecutive states are estimated with five current patterns $\cos(\varsigma_l)$, $\cos(2\varsigma_l)$, $\sin(\varsigma_l)$, $\sin(2\varsigma_l)$, and again $\cos(\varsigma_l)$. In the present numerical experiments, the scenario consists of 30 frames of images, which means that 120 current patterns are injected and 120 boundary voltage sets are measured. So the number of states evolved for each scenario is 150.

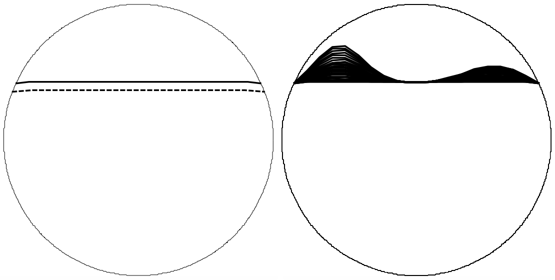

Figure 2.2. Description of the interfacial boundary movement in scenario 2 where the interface is initially nearly flat and two ripples grow with time. The left profile describes the true (solid line) and the guessed (dotted line) initial boundary, respectively. The right profile shows the evolution of the interface.

In terms of the temporal resolution, the presented image reconstruction algorithm is very advantageous. The temporal resolution of the process tomography depends on the number of measurements required to get a single frame of image and the measuring time for each measurement. For example, in static imaging with a 16-electrode system, a trigonometric method using all modes of sine and cosine functions injects 15 patterns and then the time resolution is 15τ, where τ is the time taken to inject the currents and measure the induced boundary voltages.

Figures 2.3-2.5 show the reconstructed interfacial boundary for scenario 1, in which 1%, 2%, and 3% white Gaussian noises are added to the simulated voltage measurement. As can be observed in the figures, the reconstruction performance of the proposed algorithm is fairly reasonable except in early states corresponding to the first and the second frames of the image where the improper initial guess affects the reconstruction performance. In fact, it is highly unlikely to guess the initial interface and hence higher RMSE values for the parameter d in the case of the early states are quite probable. The RMSE values as states evolve are plotted in Figure 2.6. The RMSE for the boundary voltages, $RMSE_U$, is presented in Figure 2.6 as well. The reconstructed images of Figures 2.3-2.5 and the RMSE values of Figure 1.4 indicate that as the level of measurement error increases the reconstruction performance worsens. In the above scenario, the resistivity constrast is set to 2:1. Higher contrast might be adverse to the reconstruction performance and would be more probable in real applications.

Figures 2.7-2.10 show the reconstructed results with the contrast ratios of 5:1, 10:1, 100:1, and 1000:1. The contrast ratio of 1000:1 may be considered as a binary flow of conducting and non-conducting liquids (Tossavainen *et al.* 2006). The measurement noise is set to 1%. The reconstruction performance for higher resistivity contrasts is similar to the case of contrast ratio of 2:1 although the RMSE values for the contrast ratio of 1000:1 are some what greater than those for lower contrasts especially during the early evolution states as reported in Figure 2.10. It should be noted that the pseudo measurement error covariance $\bar{R}$ should be increased to obtain converged results as listed in Table 2.2 since the system resistance increases with the contrast ratio, while other parameters remain unchanged.

For the second scenario (scenario 2) a rippled interface is considered. The contrast ratio is set to 100:1. The scenario considers a more complex interface and higher contrast ratio than scenario 1. The movement of the interfacial boundary is depicted in Figure 2.2. The interface, initially flat, is continuously varying with time and two ripples grow. Finally, the interface becomes double humped. Since the shape of the interface is much wavier compared to scenario 1, more front points are required to descrbe the interface and 10 evenly spaced front points are used. Also, the whole evolution is segmented into 280 image frames to ensure convergence. The image reconstruction with 30 frames adopted for scenario 1 was unsatisfactory and in order to determine the convergence was checked by increasing the number of frames. The increase in the number of image frames means that the interface should change less during two consecutive data collections. This may be ascribed to the increase in the number of front points to be estimated. The parameters used for the EKF model are listed in Table 2.3. Compared with scenario 1 with contrast ratio of 2:1 (see Table 2.1), larger pseudo measurement noise covariance matrices are used since the contrast ratio is increased to 100:1.

The reconstructed images are successfully compared with the true interfaces in Figures 2.12-2.14, in which the images are reconstructed every four frames. It should be noted that more deviation in the interface estimation is observed near the centre. Such deviation may explain why the centre region is less sensitive than the periphery for the usual EIT image reconstruction. Figure 19 shows the comparison of RMSE values. For the RMSE for boundary voltages, the trend according to the change of noise level is similar to that of scenario 1 with the contrast ratio of 2:1. However, the $RMSE_d$ for scenario 2 tends to be somewhat smaller than that for scenario 1. Recalling that the parameter d is measured from the centre, this difference is due to the definition of $RMSE_d$. In scenario 1 the interface is near the centre while for scenario 2 the interface is rather remote from the centre.

2.3.1 Optimal current injection protocol

In the dynamic EIT, one or only a few current injections are available and a proper selection of the current injection pattern is very important to obtain better reconstruction performance. In the conventional ERT, it has been known that the opposite method is effective in reconstructing the target near the center, while the adjacent method is good for the target near the periphery (Webster 1990). Also, the multi-referenced method like the trigonometric pattern is widely accepted as a good choice for an arbitrarily located target. In case of the estimation of the open free boundary, however, since the interface where the conductivity change occurs is located across the domain it is required that the conventional current patterns are compared and optimal current injection protocols should be designed. Therefore, the focus of this paper is to reduce the number of current injections in the inverse problem. Since, EKF is used as an inverse solver, therefore, it is also suggested to repeat the measurements in the iterative process to have a better estimate of open free boundary.

In order to find which current pattern is more sensitive to detect the interface, the distinguishability analysis is presented. Distinguishability can be defined as a measurement ability to differentiate between homogeneous and inhomogeneous conductivities inside the domain (Isaacson 1988). The distinguishability can be described in terms of norm and power. Power distinguishability is defined as the measured power change between the homogeneous and inhomogeneous cases, divided by the power applied in homogeneous case (Cheney and Isaacson 1988). The expression for norm distingusihability (N.D.) and power distinguishability (P.D.) in mean square sense is given by

$$N.D. = \sqrt{\frac{\sum_{l=1}^{L}\left|U_{meas,l} - U_{homo,l}\right|^2}{\sum_{l=1}^{L}\left|I_l\right|^2}} \tag{2.30}$$

$$P.D. = \left|\frac{\sum_{l=1}^{L}U_{homo,l}I_l - \sum_{l=1}^{L}U_{meas,l}I_l}{\sum_{l=1}^{L}U_{homo,l}I_l}\right| \tag{2.31}$$

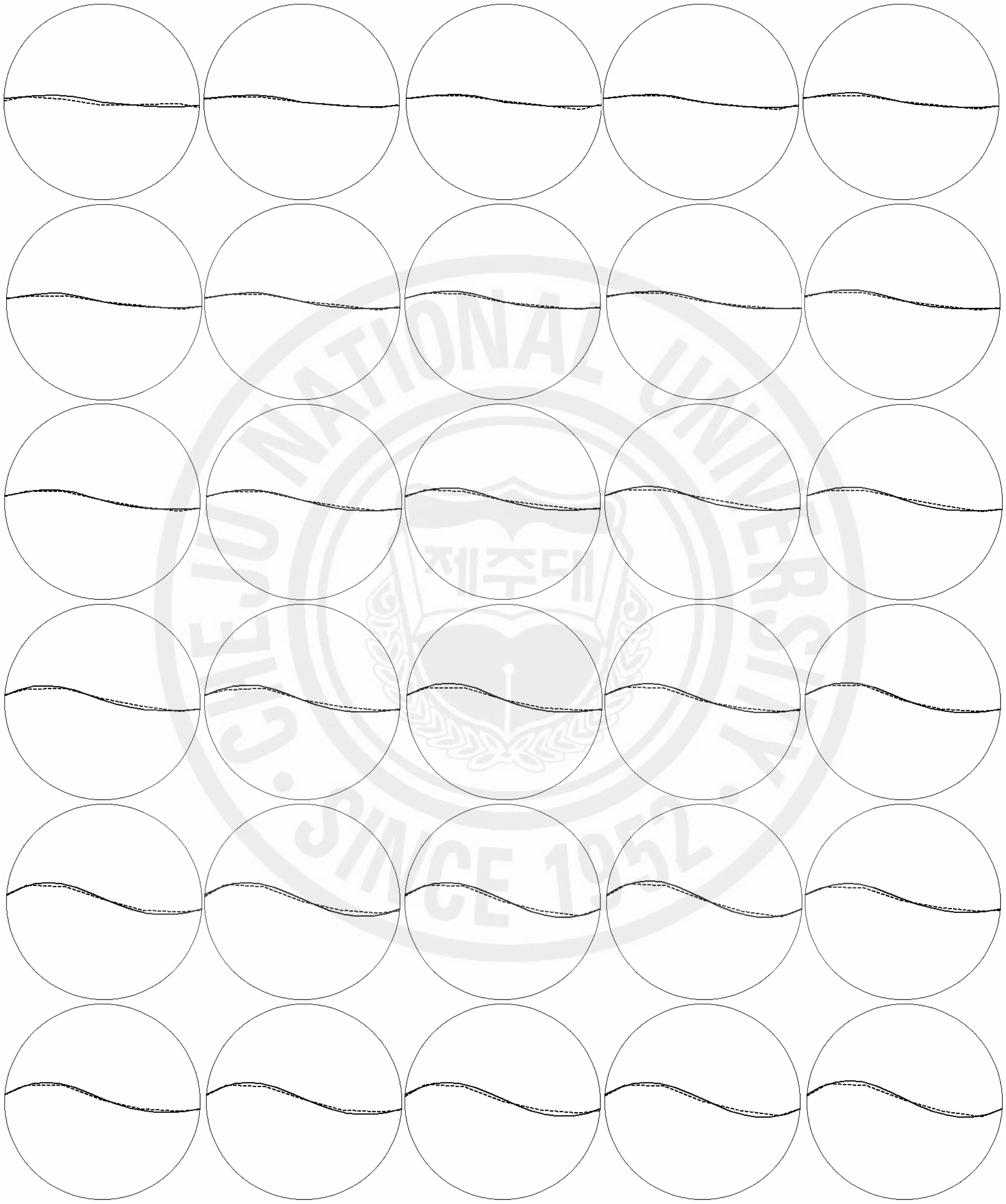

Figure 2.3. Reconstructed images for scenario 1 with 1% noise. The solid line represents the true interface and the dotted line represents the estimated interface.

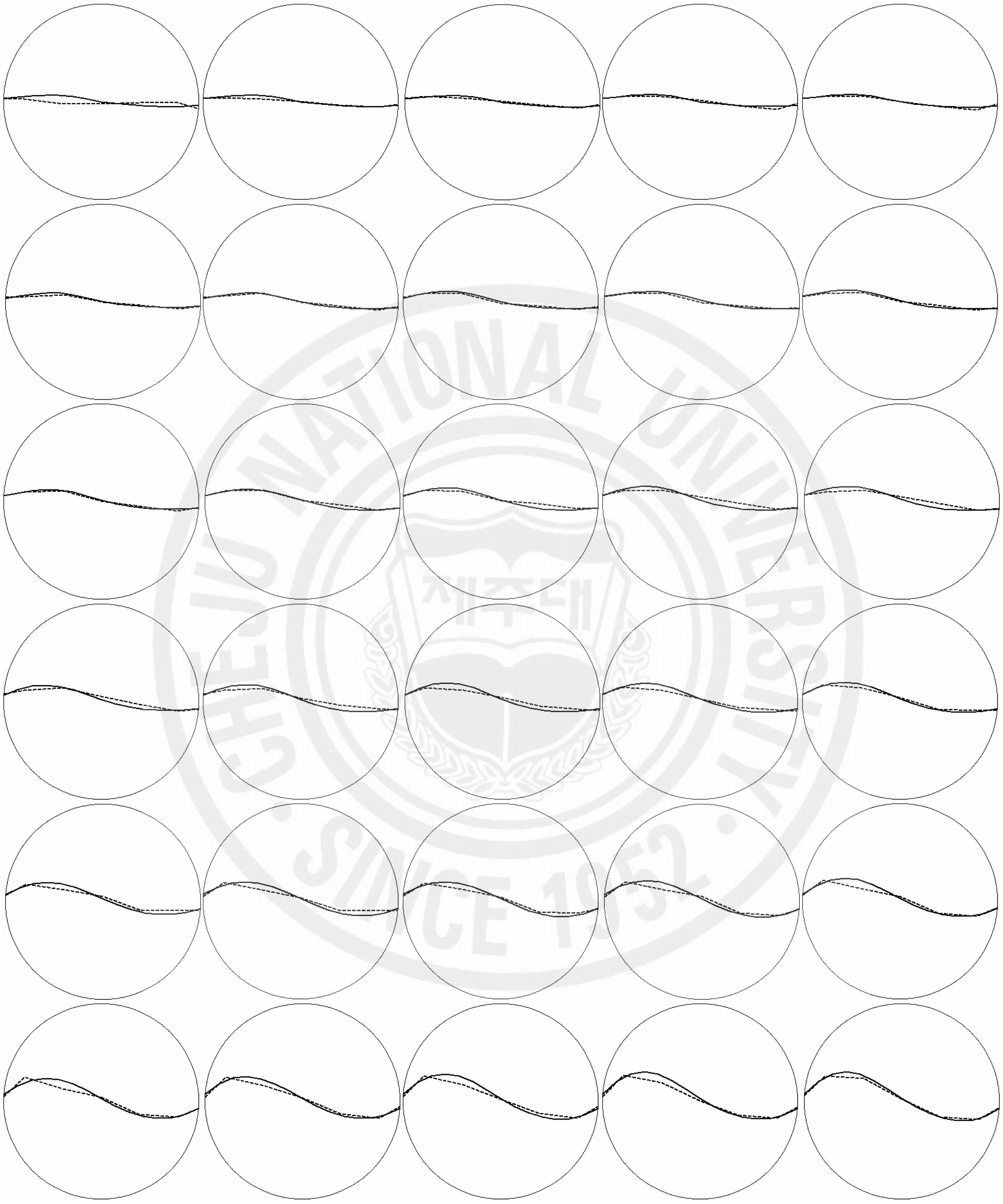

Figure 2.4. Reconstructed images for scenario 1 with 2% noise. The solid line represents the true interface and the dotted line represents the estimated interface.

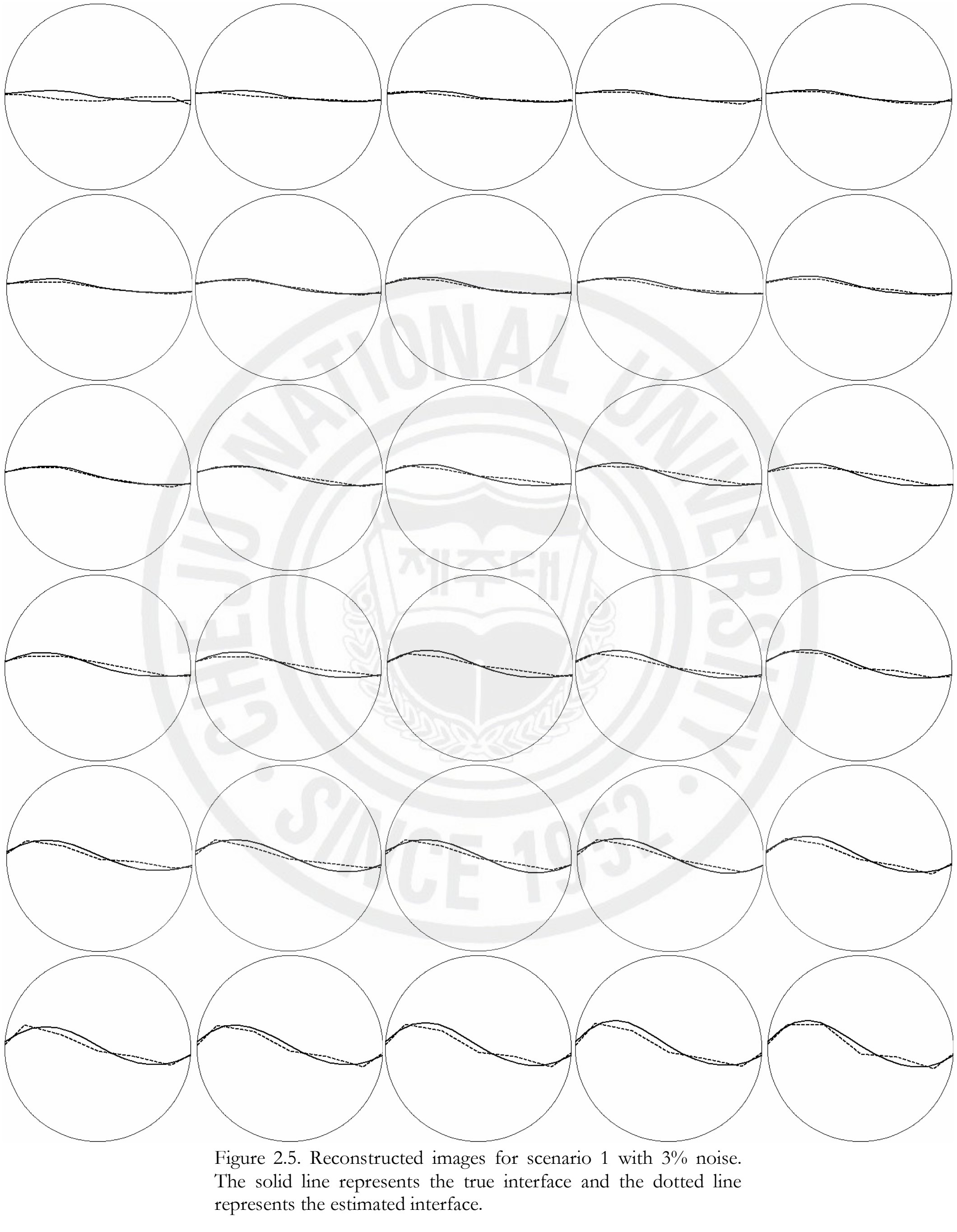

Figure 2.5. Reconstructed images for scenario 1 with 3% noise. The solid line represents the true interface and the dotted line represents the estimated interface.

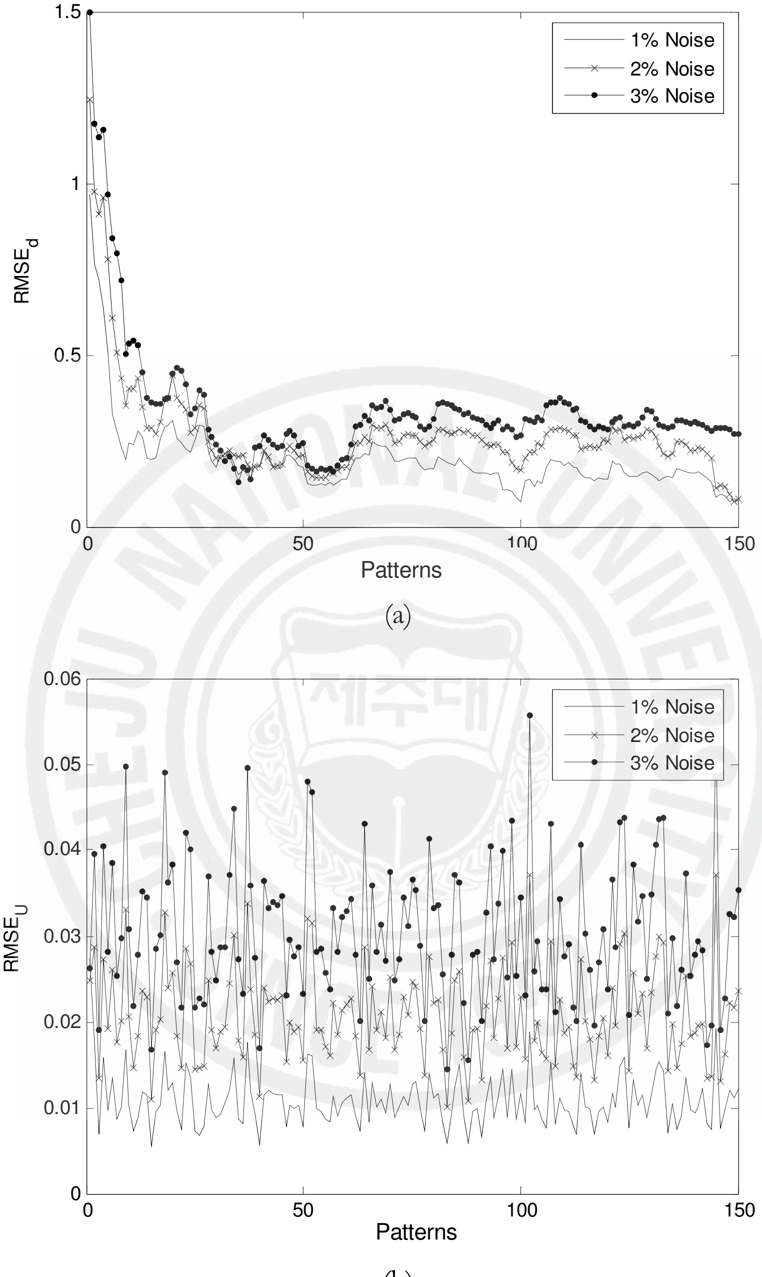

(a)

(b)

Figure 2.6. Comparison of (a) $RMSE_d$ and (b) $RMSE_U$ with 1%, 2% and 3% of noise.

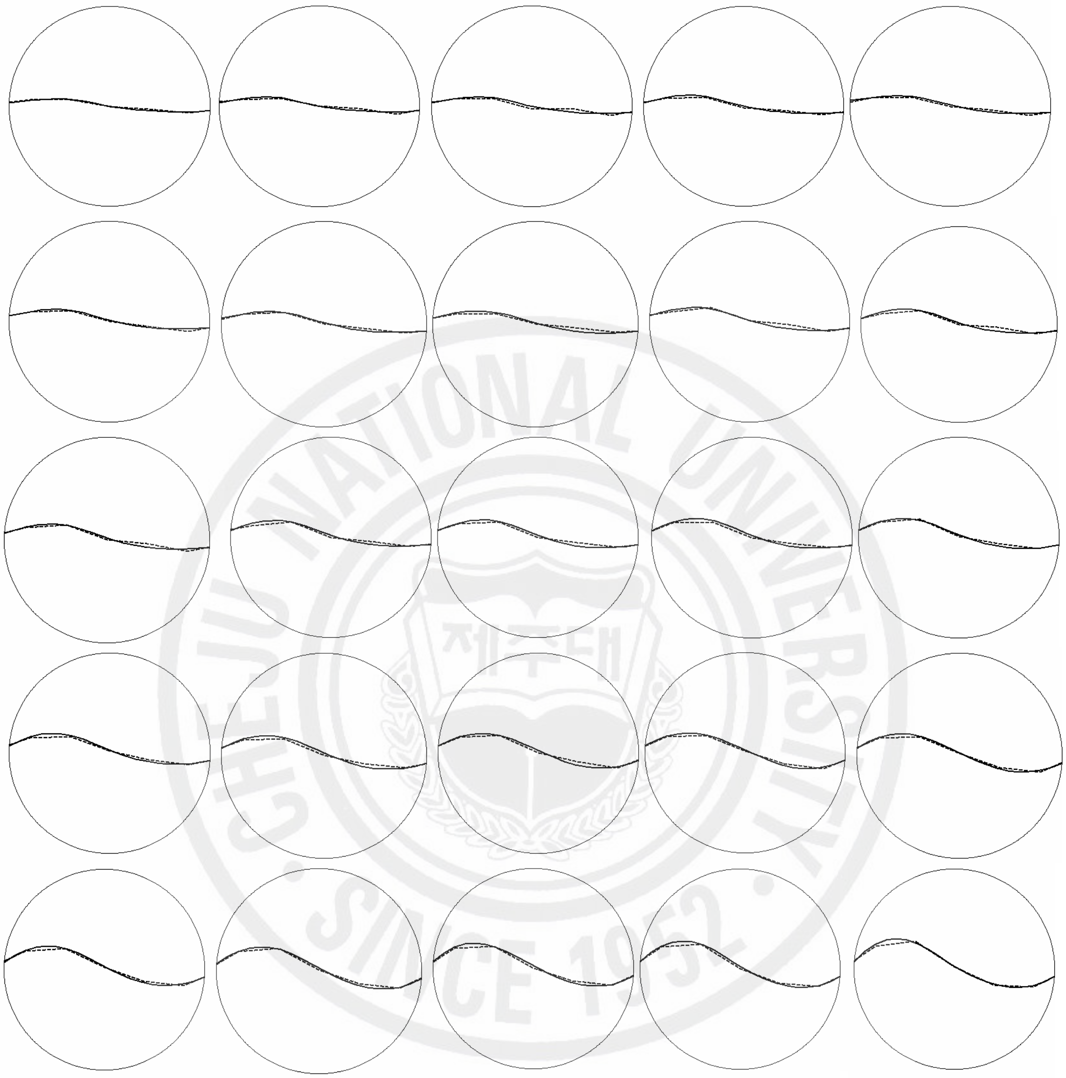

Figure 2.7. Reconstructed images for contrast ratio of 5:1 with 1% noise. The solid line represents the true interface and the dotted line represents the estimated interface.

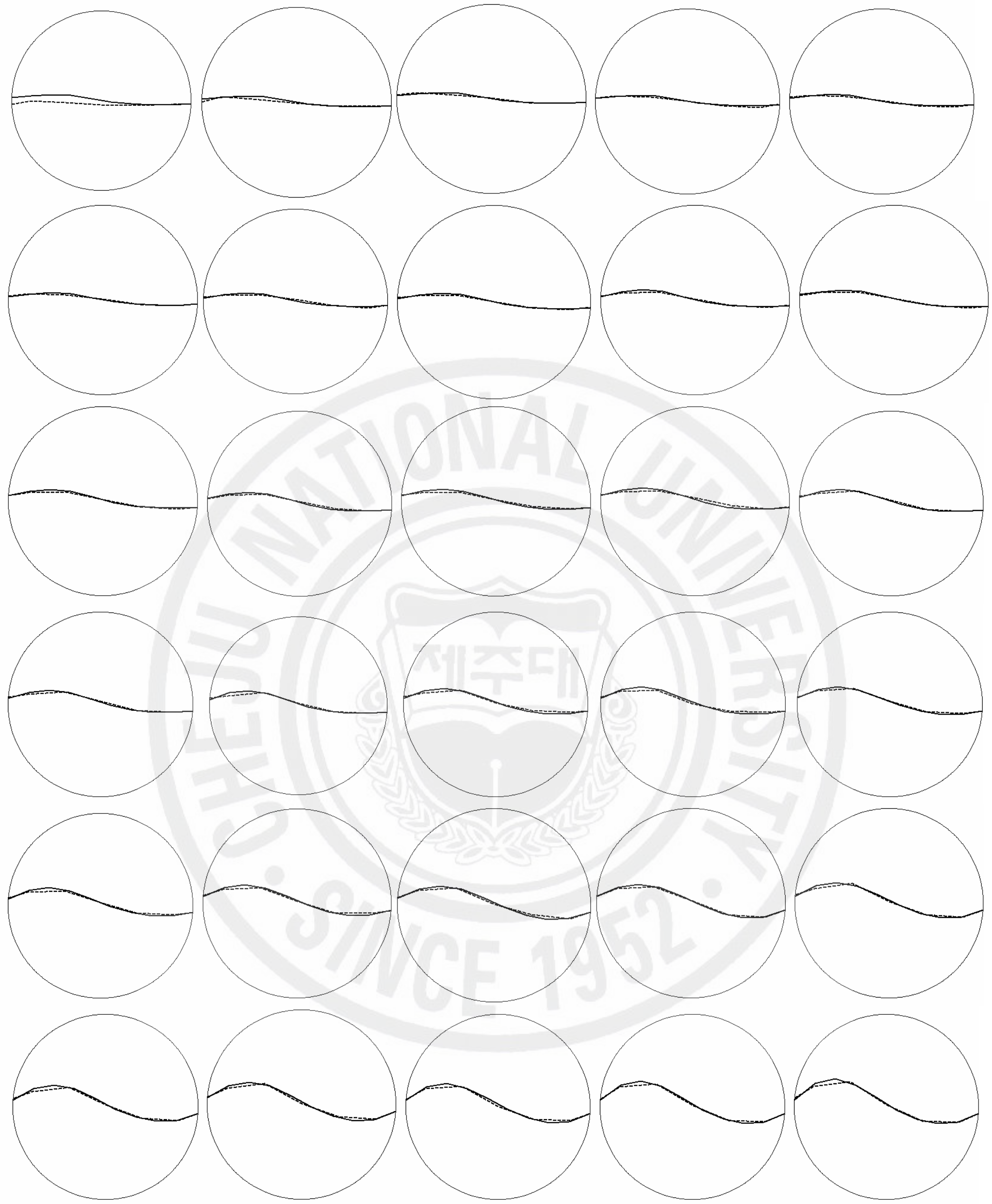

Figure 2.8. Reconstructed images for contrast ratio of 10:1 with 1% noise. The solid line represents the true interface and the dotted line represents the estimated interface.

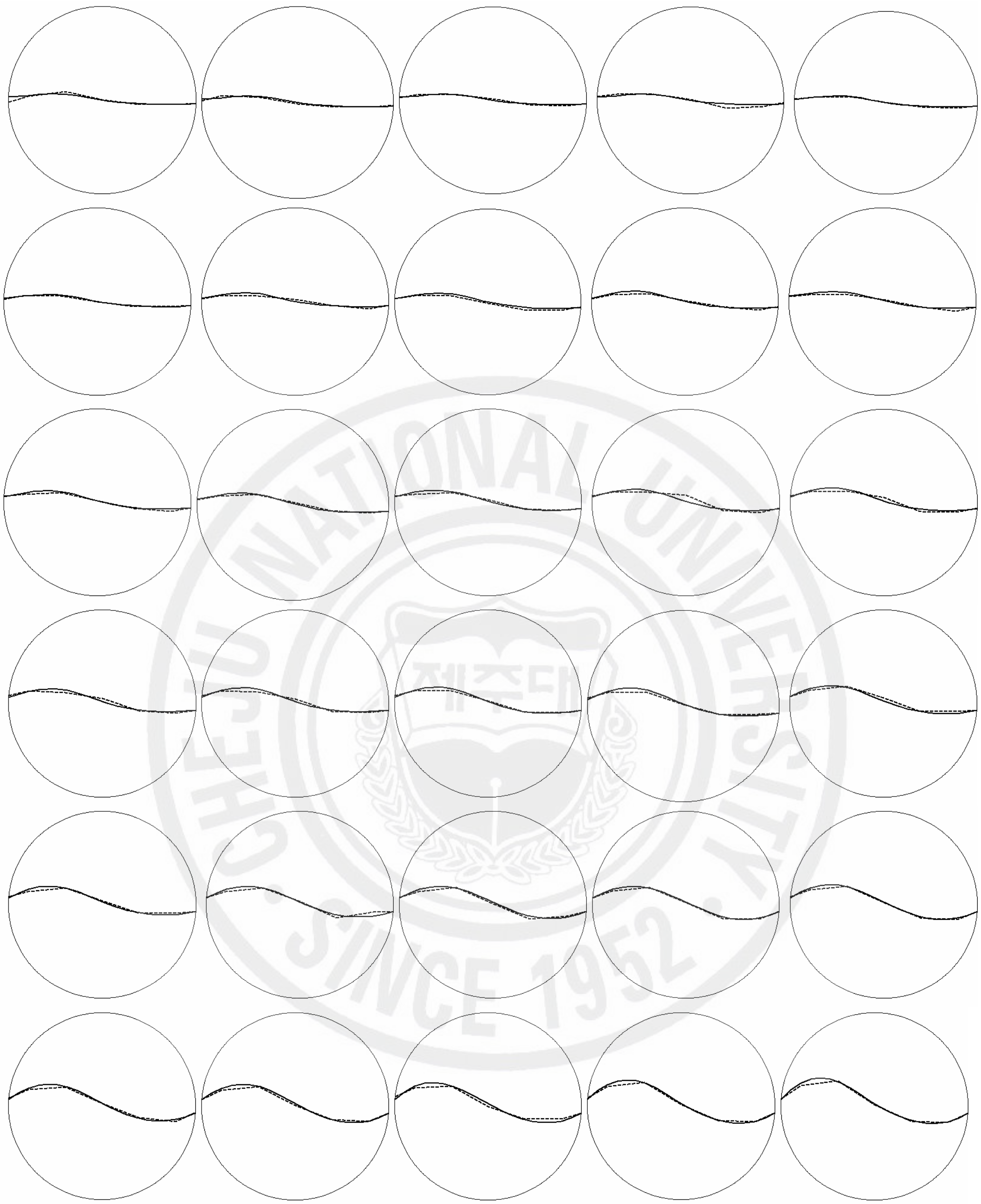

Figure 2.9. Reconstructed images for contrast ratio of 100:1 with 1% noise. The solid line represents the true interface and the dotted line represents the estimated interface.

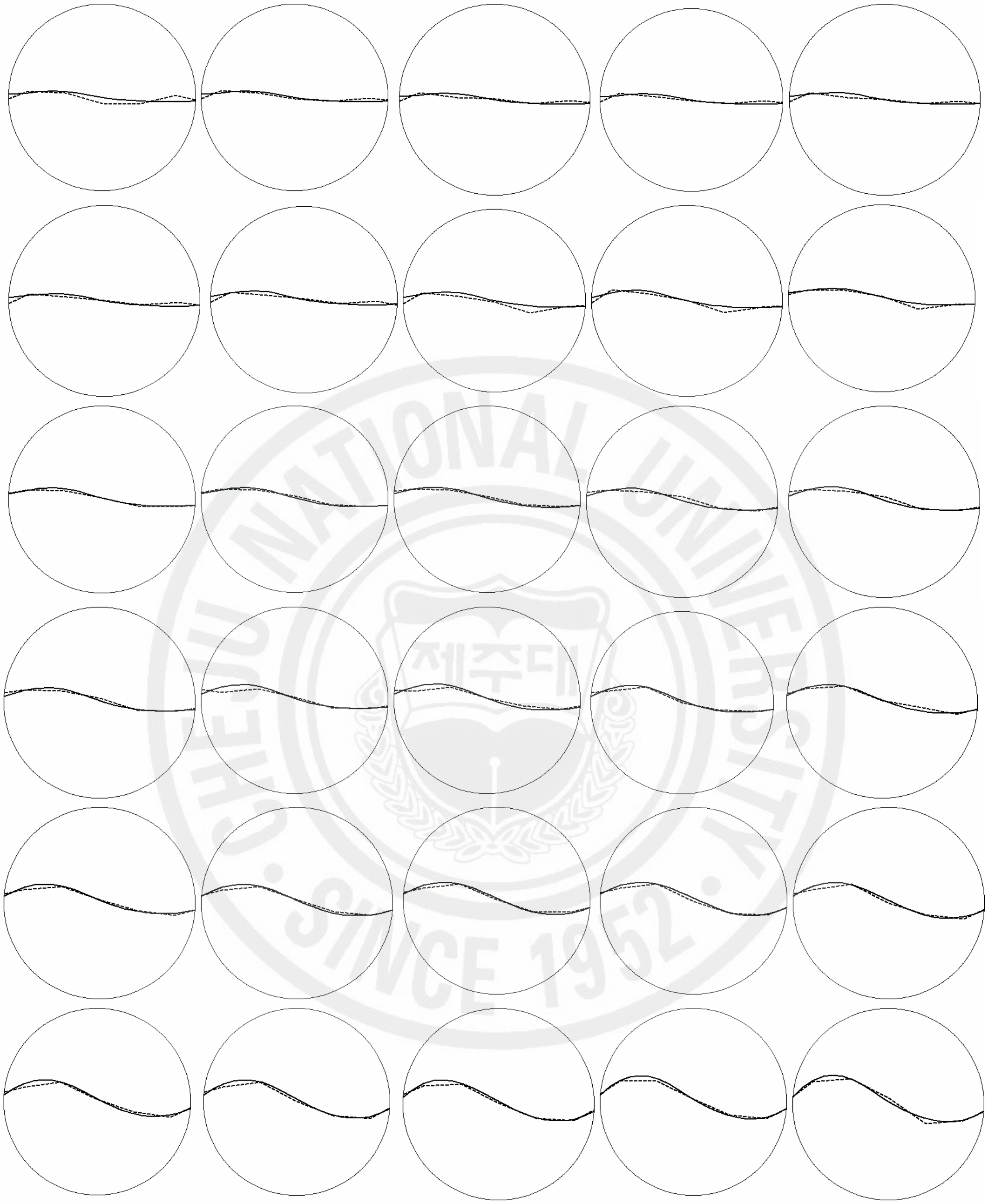

Figure 2.10. Reconstructed images for contrast ratio of 1000:1 with 1% noise. The solid line represents the true interface and the dotted line represents the estimated interface.

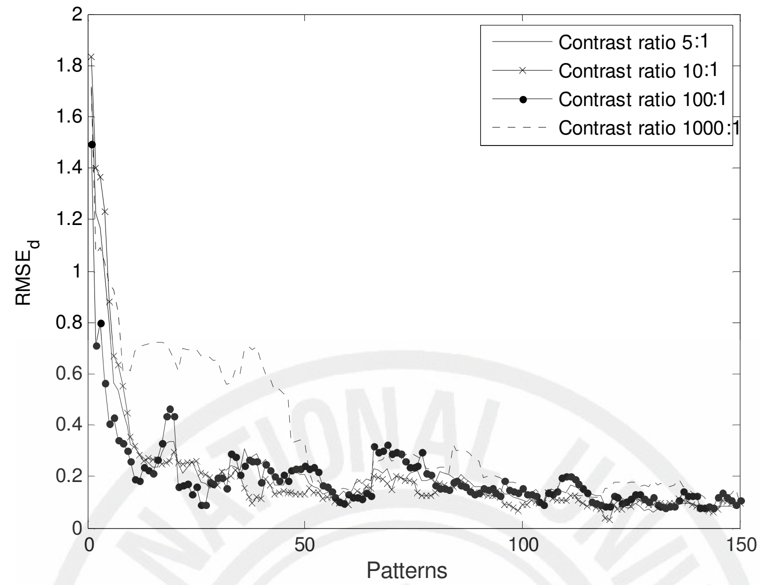

(a)

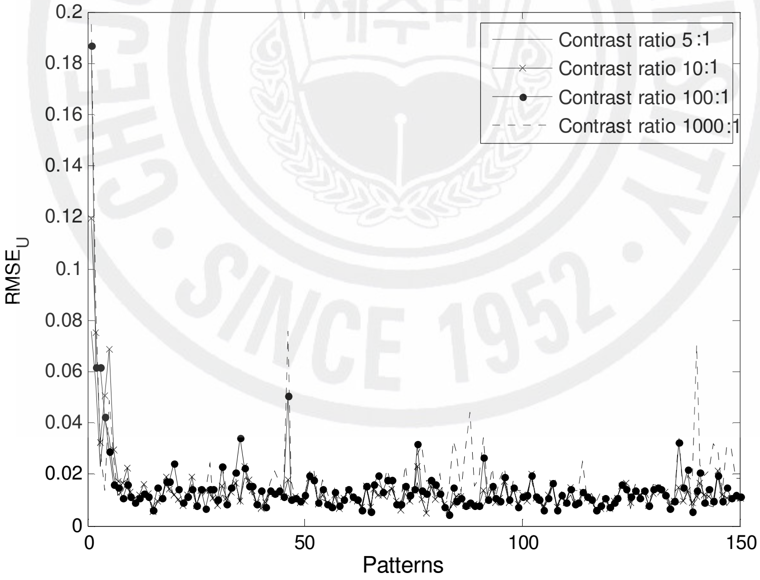

(b)

Figure 2.11. Comparison of (a) $RMSE_d$ and (b) $RMSE_U$ for scenario 1 with contrast ratios of 5:1, 10:1, 100:1, and 1000:1.

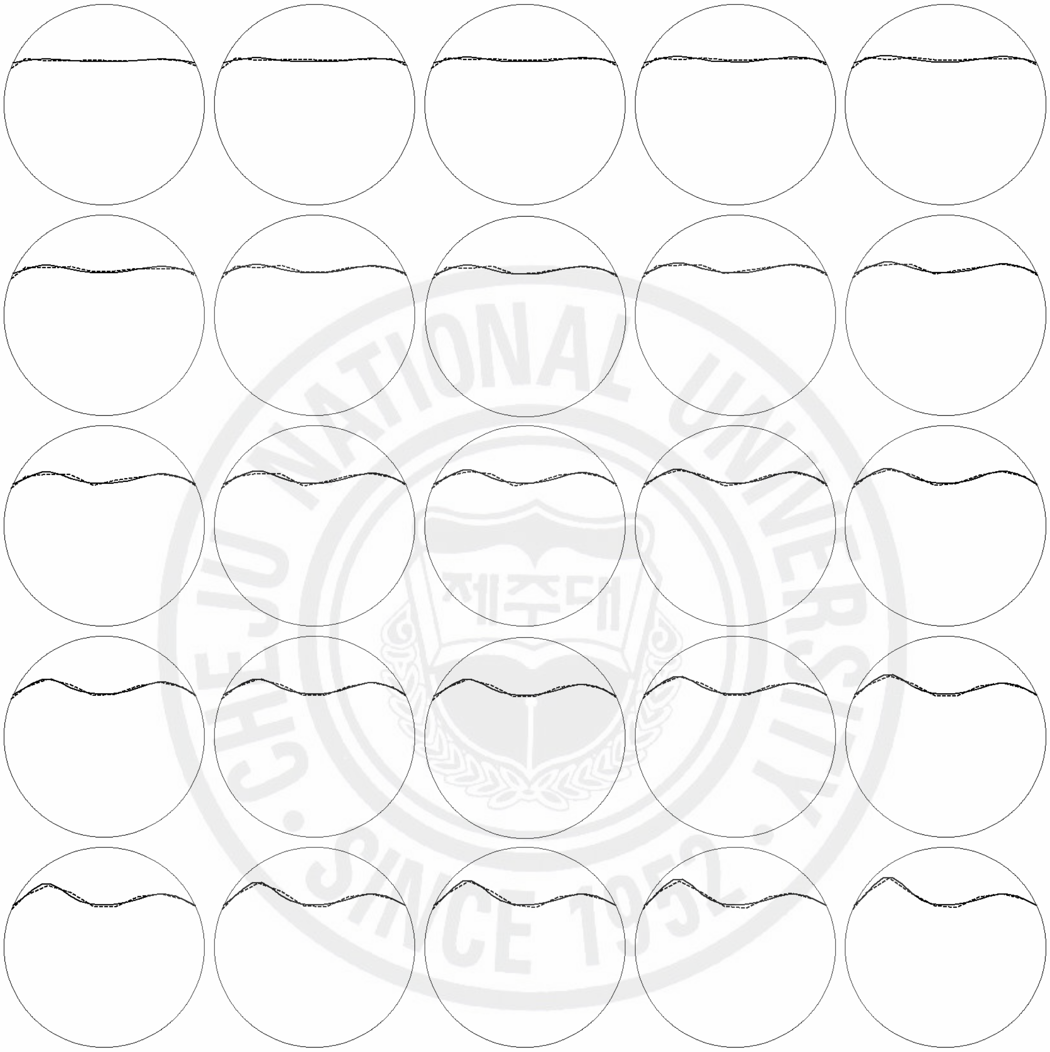

Figure 2.12. Reconstructed images for scenario 2 with 1% noise. The solid line represents the true interface and the dotted line represents the estimated interface.

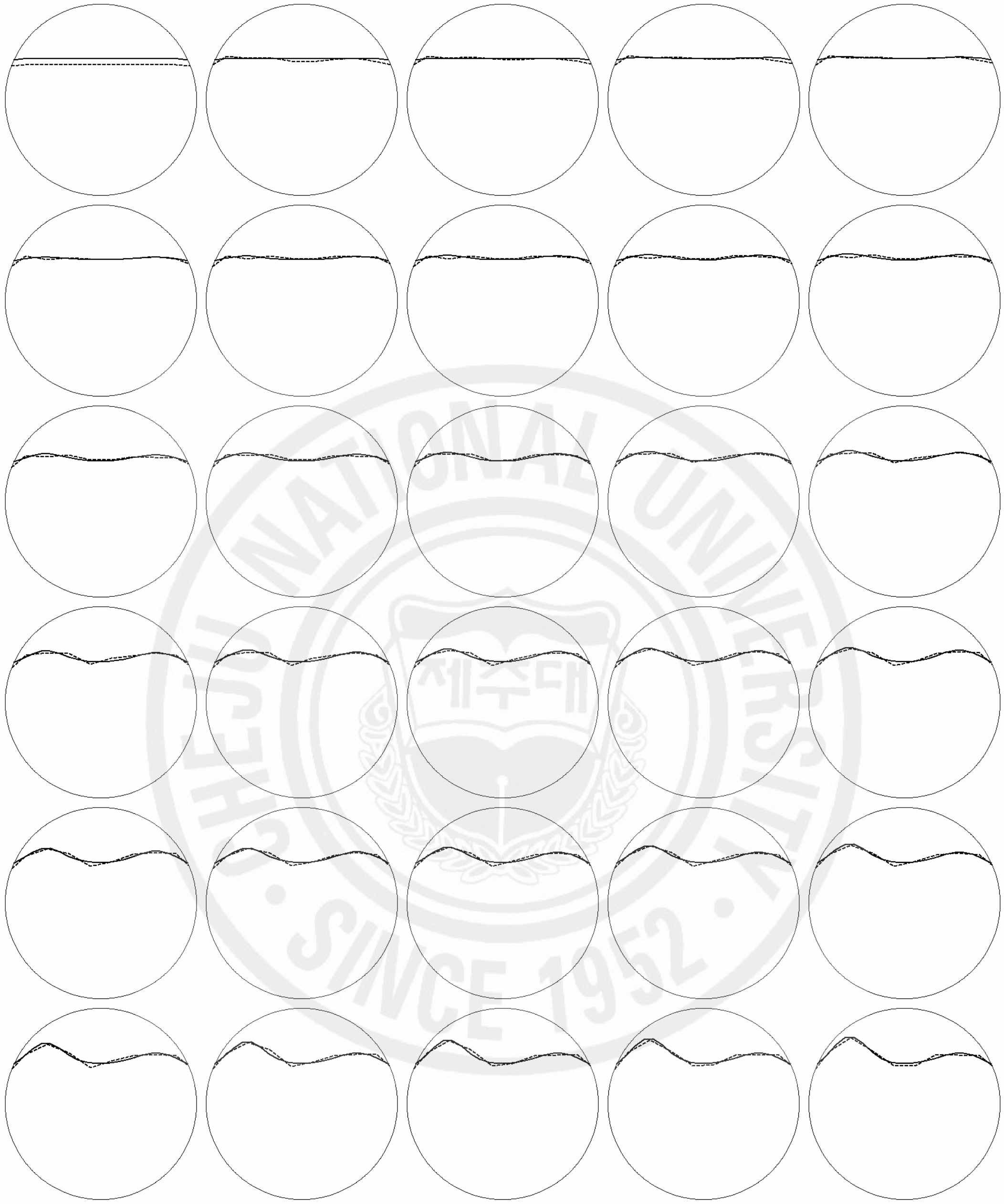

Figure 2.13. Reconstructed images for scenario 2 with 2% noise. The solid line represents the true interface and the dotted line represents the estimated interface.

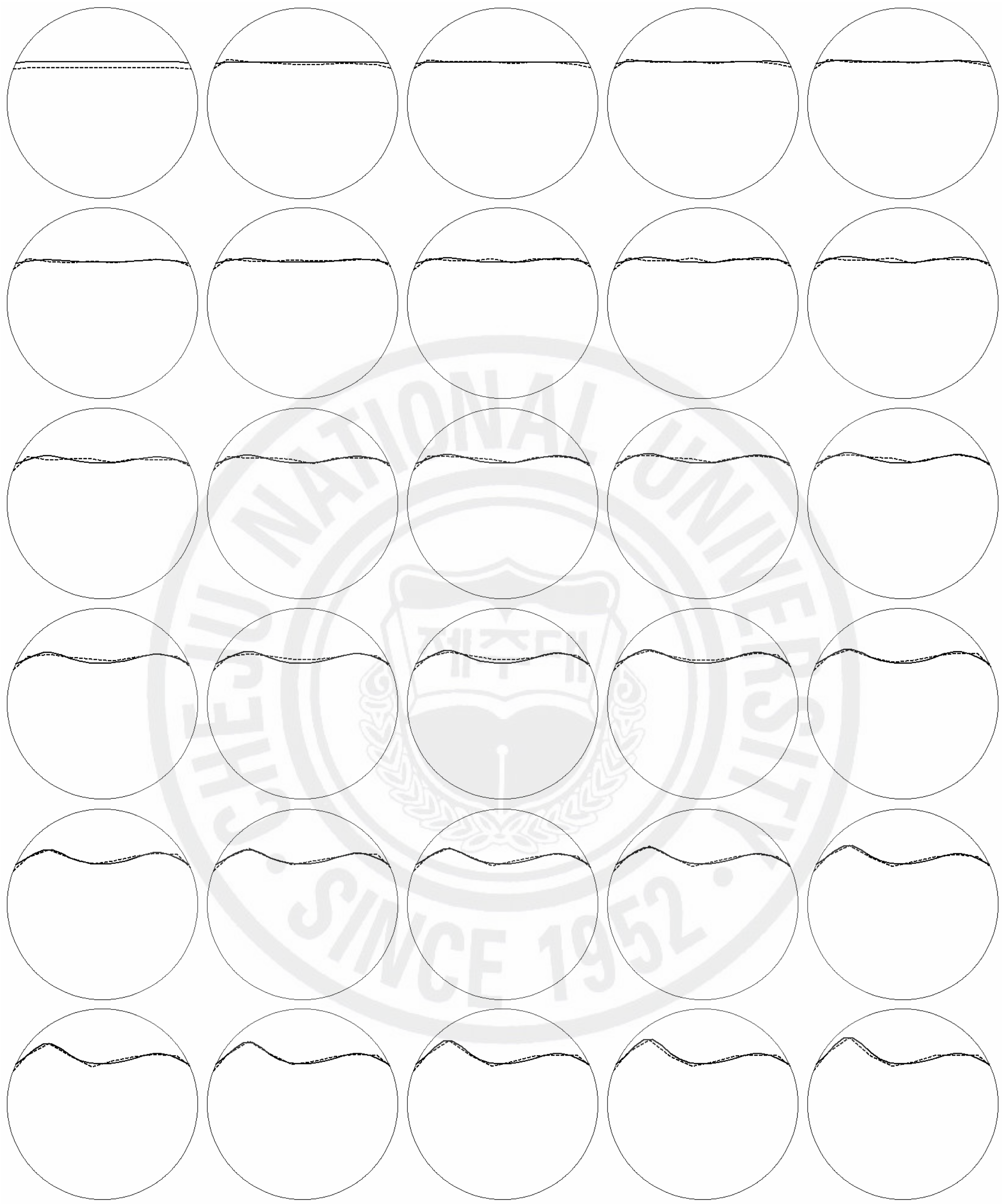

Figure 2.14. Reconstructed images for scenario 2 with 3% noise. The solid line represents the true interface and the dotted line represents the estimated interface.

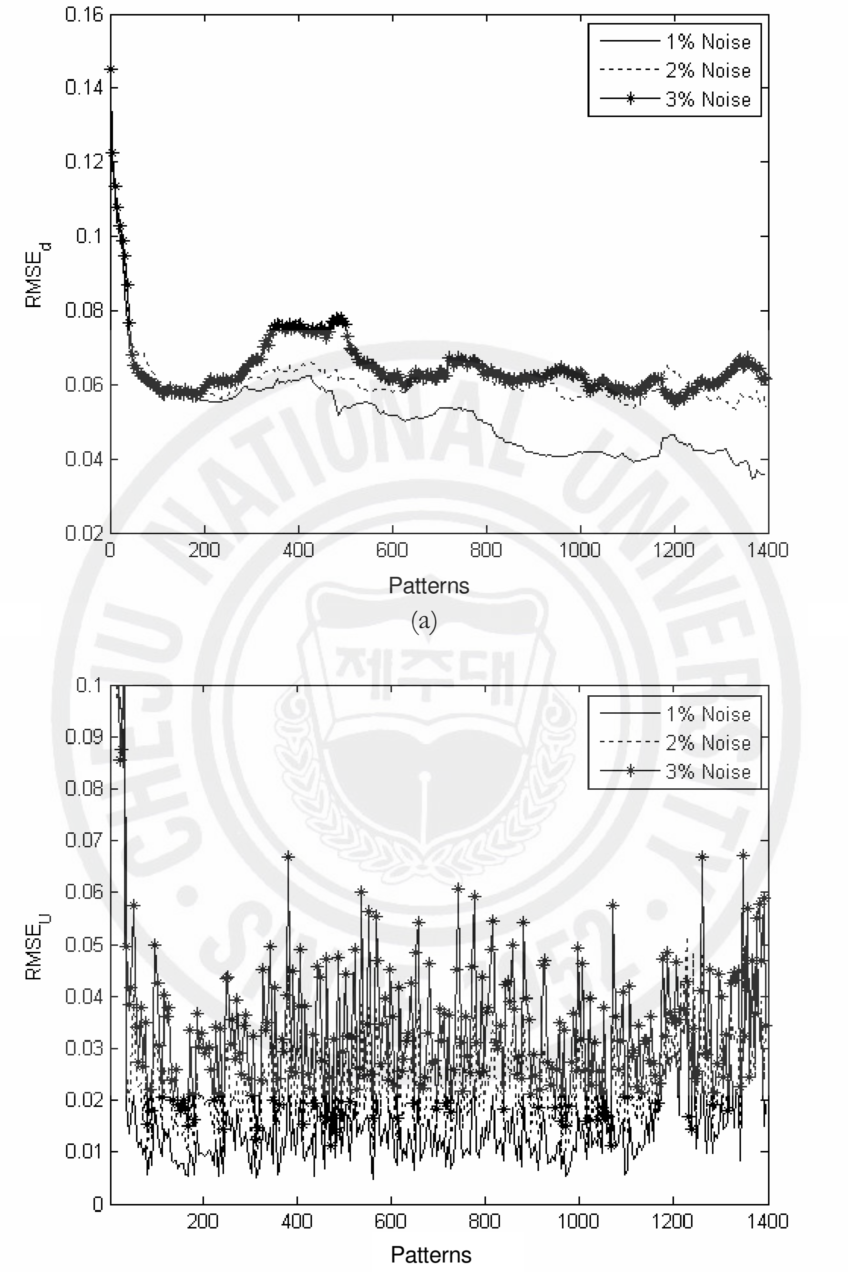

(a)

(b)

Figure 2.15. Comparison of (a) $RMSE_d$ and (b) $RMSE_U$ for scenario 2 with 1%, 2% and 3% noise.

where $U_{meas,l}$, $U_{homo,l}$ and I_l denotes the l'th measured voltage in the inhomogeneous phantom with target, l'th measured voltage when current density j_l is applied in the homogeneous phantom with no target, l'th current applied at the l'th electrode, respectively.

For the assessment of different current patterns, numerical experiments have been conducted. It is assumed that a stratified flow of two conducting immiscible liquids with distinct electrical properties flows through a cylindrical pipe of diameter 28*cm* like in the previous section. The pipe is equipped with *16* electrodes of width 2.5*cm* each around its periphery. The conductivity of each region is assumed to be known and initially set to $1/(10000\Omega cm)$ for the upper region and $1/(100\Omega cm)$ for the lower region. We consider a movement of the interfacial boundary of a stratified two-phase flow shown in Figure 2.16. The interface is approximated with 10 front points. It is assumed that the movement is snapshot with 120 frames of images and a few current injections are available during each frame. The relative noise level is set to 1% in terms of white Gaussian noise. The reconstructed images are shown in Figure 2.17 with various current injection protocols presented in Table 2.4. From the visual evaluation of the reconstructed images given in Figure 2.17, it can be noticed that trigonometric method with first 2 modes of cosine and sine show better reconstruction performance compared with other current patterns. The comparison of RMSE values for voltage and front points *d* are shown in Figure 2.18. Based on the comparison, trigonometric method with first 2 modes of cosine and sine has better performance than the other current patterns. Comparison of norm distinguishability and power distinguishability is given in Figure 2.19. Trigonometric method with first 2 modes has higher distinguishability throughout the domain in comparison to the other current injection protocols. From the Figure 2.19, it can be established that trigonometric method with first 2 modes of cosine and sine current patterns and cross method with electrodes near the interface are the most appropriate current injection protocols for front point approach.

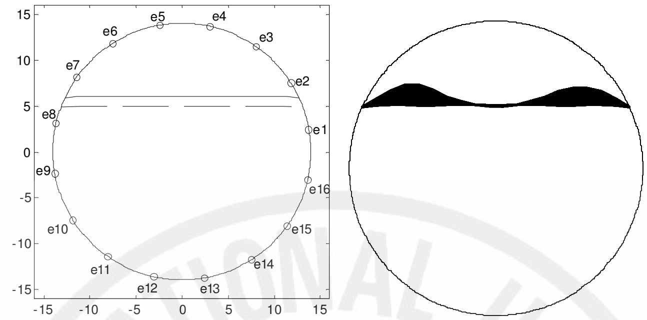

Figure 2.16. Description of the interfacial boundary movement where the interface is initially nearly flat and two ripples grow with time. The left profile describes the true (solid line) and the guessed (dotted line) initial boundary, respectively. Location of electrodes are also shown. The right profile shows the evolution of the interface.

Table 2.4. Current injection protocols used

Current Injection Protocol No.	Description
1	Trigonometric method with first 2 modes of cosine and sine (4 injections; 5 EKF states with repeated use of the first cosine)
2	Opposite method with e1-e9 and e5-e13 pairs (2 injections; 5 states with repeated use of e1-e9, e5-e13, e1-e9)
3	Cross method with e3-e7, e5-e13 pairs (2 injections; 5 states with repeated use of e3-e7, e5-e13, e3-e7)
4	Opposite method with e3-e11, e7-e15 pairs (2 injections; 5 states with repeated use of e3-e11, e7-e15, e3-e11)
5	Opposite method with e3-e11, e7-e15, e5-e13 pairs (3 injections; 5 states with repeated use of e3-e11, e7-e15)

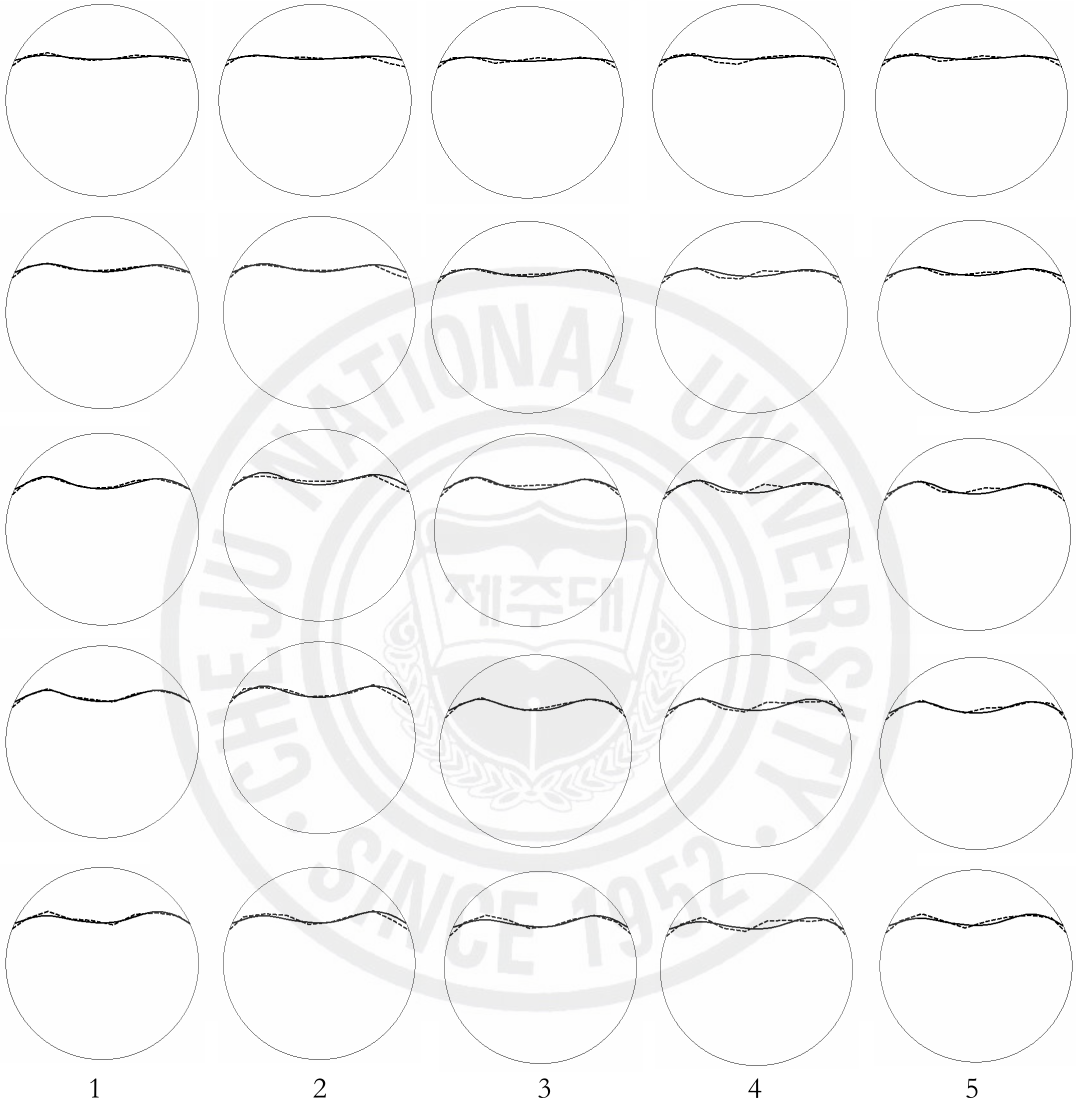

Figure 2.17. Reconstructed images for scenario 3 with 1% noise. The solid line represents the true interface and the dotted line represents the estimated interface.

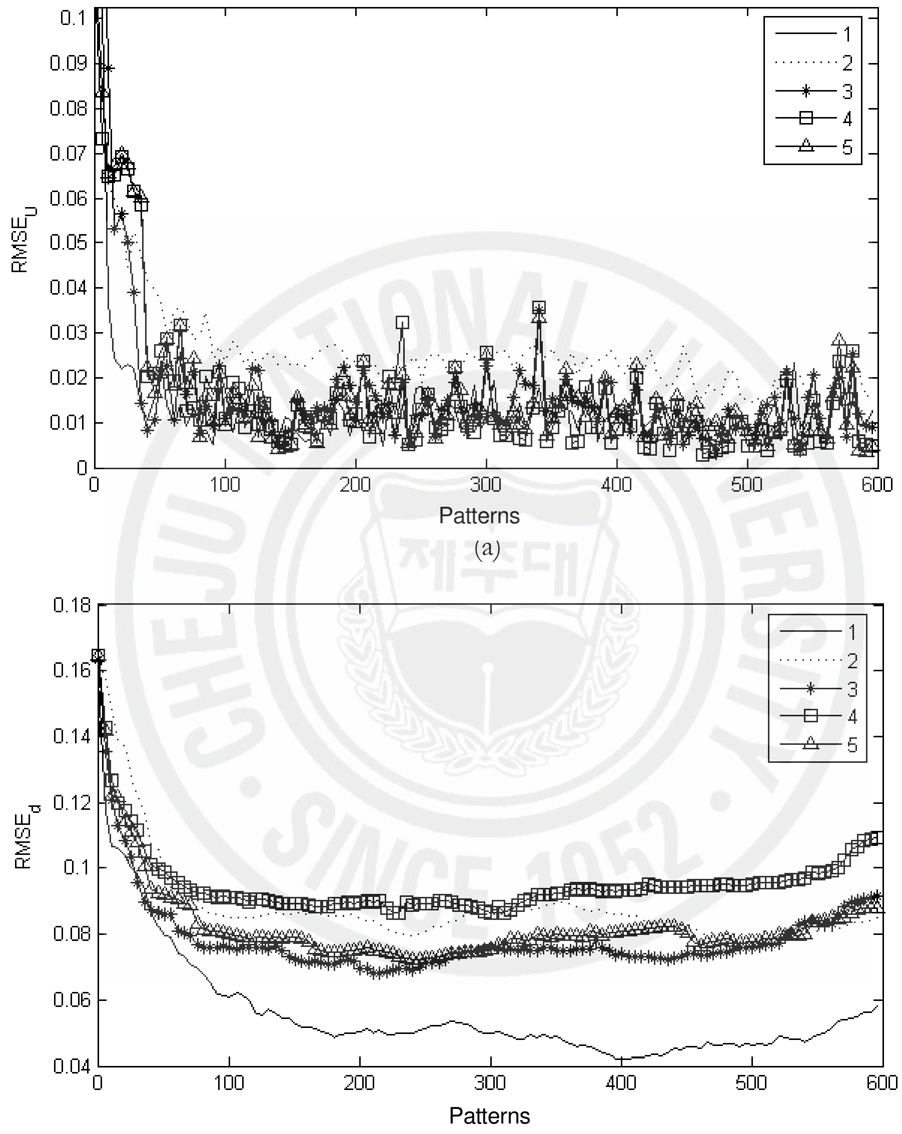

(a)

(b)

Figure 2.18. Comparison of (a) $RMSE_d$ and (b) $RMSE_U$ for scenario 3 with different current patterns.

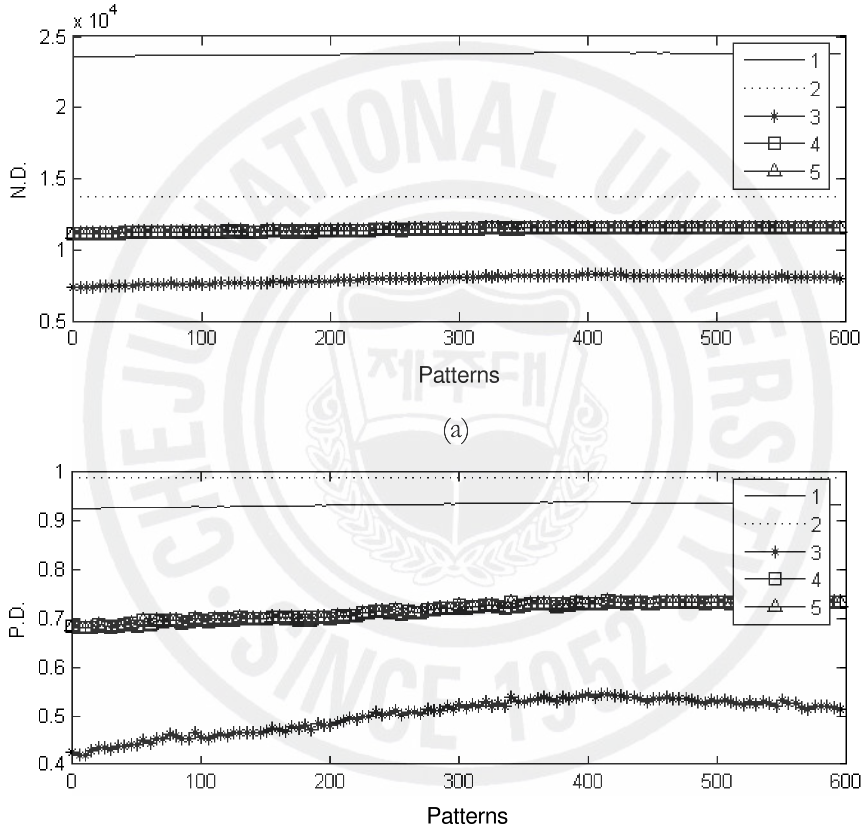

(a)

(b)

Figure 2.19. Comparison of (a) N.D. and (b) P.D. for scenario 3 with different current patterns.

3 NONSTATIONARY PHASE BOUNDARY ESTIMATION USING INTERACTING MULTIPLE MODEL SCHEME

For application of interacting multiple model scheme (IMM), we consider the underlying inverse problem as a state estimation problem to estimate the nonstationary phase boundaries in the domain. It is assumed that the conductivity values of the objects are known constants. It is also assumed that the problem has been discretized with respect to the time variable. In the state estimation problem, we need the so-called dynamic model which constists of the state equation, that is, the evolution of the boundaries, and the observation equation, that is, the relationship between the boundary vector and measured voltages.

Firstly, consider the state evolution model. In general the evolution of the boundary vector for front points d is related by the following nonlinear mapping:

$$d_{k+1} = g_k(d_k) + w_k \tag{3.1}$$

where d_k is the state vector (the boundary representation) at the time kT, g_k is a function ($g_k : \mathbb{R}^{\Lambda} \to \mathbb{R}^{\Lambda}$) defining the state transition from time kT to $(k+1)T$, where T is the sampling period (measurement interval between successive patterns), and w_k is assumed to be white Gaussian noise to compensate for the modelling uncertainties. Here, the state equation is assumed to be of linear form with different process noise:

$$d_k^i = F_{k-1} d_{k-1}^i + w_{k-1}^i \tag{3.2}$$

where $F_k \in \mathbb{R}^{\Lambda \times \Lambda}$ is the state transition matrix at time kT and $i = 1, 2, ..., M$, where M is the number of different models. Here, we take $F_k \equiv I_N$ (the identity matrix). Then equation (3.2) becomes the random-walk model in which the rate of time evolution is governed by the different covariance matrices, defined by

$$Q_k^i = E[w_k^i (w_k^i)^T] \tag{3.3}$$

Next, consider the observation model. Let $V_k \in \mathbb{R}^E$, as defined as

$$V_k = (V_k^1, V_k^2, \ldots, V_k^E)^T \tag{3.4}$$

be the actual surface measurement voltages induced by the *k*'th current pattern. Then the relationship between the boundary vector and measured voltages can be described by the following nonlinear mapping with a measurement error:

$$V_k = U_k(d_k) + v_k \tag{3.5}$$

where U_k is a function ($U_k : \mathbb{R}^\Lambda \to \mathbb{R}^E$) defining the relationship between the boundary vector and measured voltages for the *k*'th current pattern. The measurement error $v_k \in \mathbb{R}^E$ is assumed to be white Gaussian noise with covariance

$$R_k = E[v_k v_k^T] \tag{3.6}$$

Linearizing (3.6) about the predicted (time-updated) states of the *i*'th model $d_{k|k-1}^i$, which will be described later, we obtain

$$V_k = U_k(d_{k|k-1}^i) + J_k^i(d_{k|k-1}^i).(d_k^i - d_{k|k-1}^i) + HOT + v_k \tag{3.7}$$

where 'HOT' represent the higher order terms which are assumed to be additional white Gaussian noise and $J_k^i(d_{k|k-1}^i) \in \mathbb{R}^{E\times\Lambda}$ is the Jacobian matrix defined by

$$J_k^i(d_{k|k-1}^i) \equiv \left.\frac{\partial U_k}{\partial d}\right|_{d=d_{k|k-1}^i} \tag{3.8}$$

Then the following linearized measurement equation is obtained:

$$y_k^i = J_k^i(d_{k|k-1}^i).d_{k|k-1}^i + \overline{v}_k \tag{3.9}$$

where $\overline{v}_k \in \mathbb{R}^E$ is composed of the measurement error and linearization error with known covariances as

$$\overline{R}_k = E[\overline{v}_k \overline{v}_k^T] \tag{3.10}$$

3.1 Extended Kalman filter

In Kalman filtering we estimate the state vector d_k^i for each model based on all the measurements taken up to the time kT. With the Gaussian assumptions, the required estimate is obtained by minimizing the cost functional which is formulated based on the above state and measurement equations (3.2) and (3.9), respectively. The cost functional for the extended Kalman filter (EKF) is of the form

$$\begin{aligned}\Phi^i(d_k^i) = \frac{1}{2}[&\| d_k^i - d_{k|k-1}^i \|_{(C_{k|k-1}^i)^{-1}} + \| y_k^i - J_k^i(d_{k|k-1}^i).d_k^i \|_{\overline{R}_k^{-1}} \\ &+\alpha_R \| L_R(d_k^i - d^*) \|]\end{aligned} \tag{3.11}$$

where $\| x \|_A$ denotes $x^T A x$, α_R and $L_R \in \mathbb{R}^{\Lambda\times\Lambda}$ are the regularization parameter and matrix, respectively, d^* is an *a priori* guess for the boundary representation and $C_{k|k-1}^i \in \mathbb{R}^{\Lambda\times\Lambda}$ is the time-updated error covariance matrix, which is defined by

$$C_{k|k-1}^i \equiv E[(d_k^i - d_{k|k-1}^i)(d_k^i - d_{k|k-1}^i)^T] \tag{3.12}$$

The first two norms in equation (3.11) refer to the weighted norms, having as weighting matrices the inverse of the covariances. The third them on the right-hand side of equation (3.11) is the regularization term which is included to mitigate the ill-posedness of the givern inverse problem. We used the generalized Tikhonov regularization under a smoothness assumption in constructing the regularization matrix (L_R), with the regularization parameter α_R chosen empirically.

If we define the augmented pseudo-measurement $\tilde{y}_k^i \in \mathbb{R}^{(E+\Lambda)}$ and measurement matrix $H_k^i \in \mathbb{R}^{(E+\Lambda)\times\Lambda}$

$$\tilde{y}_k^i \equiv \begin{pmatrix} y_k^i \\ \sqrt{\alpha_R} L_R d^* \end{pmatrix} \tag{3.13}$$

$$H_k^i \equiv \begin{pmatrix} J_k^i(d_{k|k-1}^i) \\ \sqrt{\alpha_R} L_R \end{pmatrix} \tag{3.14}$$

then the cost function (3.11) can be rearranged as

$$\Phi^i(d_k^i)=\frac{1}{2}[\| d_k^i - d_{k|k-1}^i \|_{(C_{k|k-1}^i)^{-1}} + \| \tilde{y}_k^i - H_k^i.d_k^i \|_{\Gamma_k^{-1}}] \tag{3.15}$$

where $\Gamma_k \in \mathbb{R}^{(E+\Lambda)\times(E+\Lambda)}$ is a block diagonal matrix defined by

$$\Gamma_k \equiv Blockdiag[\bar{R}_k, I_\Lambda] \tag{3.16}$$

Minimizing the cost functional equation (3.15) and solving for the updates of the associated covariance matrices, we obtain the recursive extended Kalman filter algorithm for each model, which consists of the following two steps (Gelb 1974):

- time update (prediction)

$$d_{k+1|k}^i = F_k d_{k|k}^i \tag{3.17}$$

$$C_{k+1|k}^i = F_k C_{k|k}^i (F_k)^T + Q_k^i \tag{3.18}$$

- measurement update (filtering)

$$K_{k+1}^i = C_{k+1|k}^i (H_{k+1}^i)^T [H_{k+1}^i C_{k+1}^i (H_{k+1}^i)^T + \Gamma_{k+1}]^{-1} \tag{3.19}$$

$$d_{k+1|k+1}^i = d_{k+1|k}^i + K_{k+1}^i (\tilde{y}_{k+1}^i - H_{k+1}^i d_{k+1|k}^i) \tag{3.20}$$

$$C_{k+1|k+1}^i = (I_\Lambda - G_{k+1}^i H_{k+1}^i) C_{k+1|k}^i \tag{3.21}$$

Hence, we can find the estimated state $d_{k|k}^i$ for model i for $k=0,1,2,...,K$ ($K=rp$), where K is the final step for iteration, p is the number of independent current patterns and r is the number of classical frames. The most striking feature is that the Kalman filtering technique is an online recursive form in place of the offline batch form of the back projection or modified Netwon-Raphson algorithm. Therefore, there is no need to store the past measurements in order to estimate the present state.

3.2 Phase boundary estimation with IMM algorithm

The particular behaviour of the IMM algorithm demonstrated in this application also sets it apart from other applications. Although the general idea underlying the IMM algorithm is to combine multiple models in order to decide which model gives the best fit with the measurements, what is specific to this application is that these models only differ in their rate of evolution (different process noise covariance matrices are considered here).

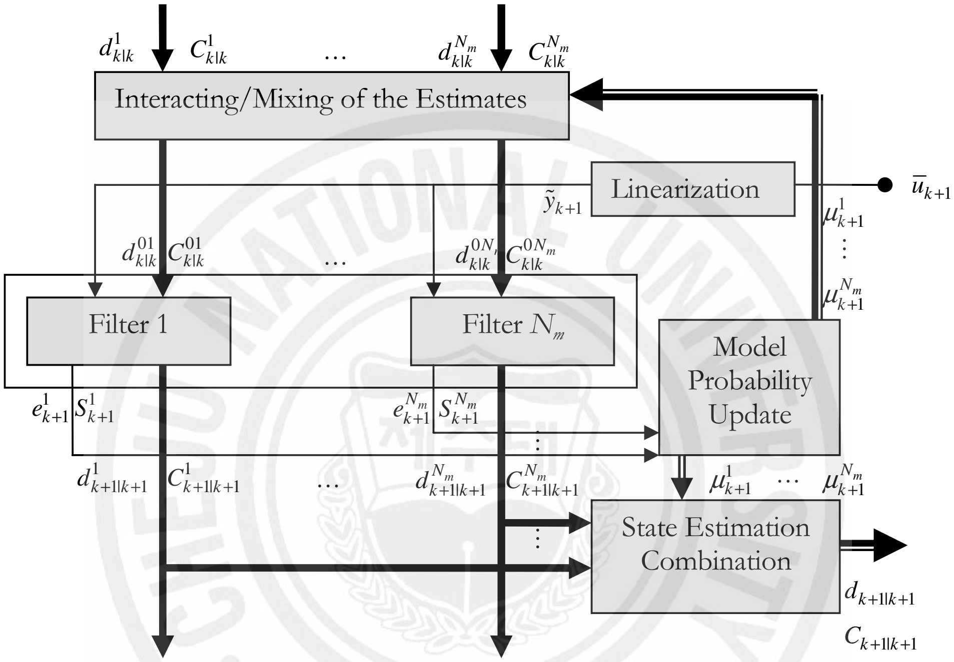

Figure 3.1. One-cycle flow diagram of the inverse solver with the IMM algorithm.

The IMM algorithm is composed of an estimate mixer at the input of each model-conditioned filter, a bank of the EKFs running simultaneously, a model probability evaluator and an estimate combiner at the output of the filters. The flow diagram of the IMM algorithm for 1 cycle is depicted in Figure 3.1. The multiple models interact through the mixing to estimate the time-varying boundary representation. With the assumption that the model transition is governed by an underlying Markov chain, the mixed estimate to each filter is obtained based on the model probabilities and the model transition probabilities. In the filtering stage, each EKF uses a mixed estimate and a voltage measurement to compute a new estimate. The model probabilities are evaluated based on the model transition probabilities. Finally, the overall state estimate is computed in the form of the weighted sum of the new estimates and their model probabilities. The mathematical details of the procedure are as follows (More details are given in Blom and Bar-Schalom (1998), Mazor *et al.* (1998))

Step 1. set the initial condition for $d^i_{0|0}$, $C^i_{0|0}$, μ^i_0, π_{ij}, $Q^i\,(i, j = 1, 2, ..., N_m)$ and $\bar{R}$.

Step 2. mixing (interaction) of the estimates

The mixed initial condition for the *j*'th filter can be computed as

- mixing estimate

$$d^{0j}_{k|k} = \sum_{i=1}^{N_m} d^i_{k|k}\mu^{i|j}_k \tag{3.22}$$

- mixing covariance

$$C^{0j}_{k|k} = \sum_{i=1}^{N_m} [C^i_{k|k} + (d^{0j}_{k|k} - d^i_{k|k})(d^{0j}_{k|k} - d^i_{k|k})^T]\mu^{i|j}_k \tag{3.23}$$

where $d^{0j}_{k|k}$ and $C^{0j}_{k|k}$ represent the mixed state and error covariance, respectively. For the input of the jth model-conditioned EKF. $\mu^{i|j}_k$ in equations (3.22) and (3.23) is the mixing probability (the weight with which the estimates from the previous circle are given to each filter at the beginning of the current cycle), defined by

$$\mu^{i|j}_k \equiv \frac{1}{\bar{c}_j}\pi_{ij}\mu^i_k \tag{3.24}$$

where the normalizing constant $\bar{c}_j$ is calculated by

$$\bar{c}_j = \sum_{i=1}^{N_m} \pi_{ij}\mu^i_k \tag{3.25}$$

where π_{ij} is the assumed Markovian transition probability from model i to model j, which is defined by

$$\pi_{ij} \equiv \Pr\left\{ M_{k+1}^{j} \mid M_{k}^{i} \right\},\ \forall M^{i}, M^{j} \in M^{s} \tag{3.26}$$

where $\Pr\{.\}$ is probability and M_k^i is the event that the i th mode is in effect at sampling time k and M^s is the set of all possible modal states at all times.

Step 3. model-conditioned filtering

Two states of the model-conditioned EKF can be summarized as

- time update (prediction)

$$d_{k+1|k}^{j} = F_k d_{k|k}^{0j} \tag{3.27}$$

$$C_{k+1|k}^{j} = F_k C_{k|k}^{0j} (F_k)^T + Q_k^j \tag{3.28}$$

- measurement update (filtering)

$$K_{k+1}^{j} = C_{k+1|k}^{j} (H_{k+1}^{j})^T (S_{k+1}^{j})^{-1} \tag{3.29}$$

$$d_{k+1|k+1}^{j} = d_{k+1|k}^{j} + K_{k+1}^{j} e_{k+1}^{j} \tag{3.30}$$

$$C_{k+1|k+1}^{j} = (I_{\Lambda}^{j} - G_{k+1}^{j} H_{k+1}^{j}) C_{k+1|k}^{j} \tag{3.31}$$

where $G_{k+1}^j \in \mathbb{R}^{\Lambda \times (E+\Lambda)}$ is the Kalman gain at time $(k+1)T$. The residuals and their covariances are defined as

$$e_{k+1}^{j} \equiv \tilde{y}_{k+1}^{j} - H_{k+1}^{j} d_{k+1|k}^{j} \tag{3.32}$$

$$S_{k+1}^{j} \equiv H_{k+1}^{j} C_{k+1|k}^{j} (H_{k+1}^{j})^T + \Gamma_{k+1} \tag{3.33}$$

where pseudo-measurement $\tilde{y}_{k+1}^j$ and covariance matrix Γ_{k+1} are given by equations (3.13) and (3.16), respectively.

Step 4. model probability evaluation

- likelihood function

$$L_{k+1}^{j} = \frac{1}{\sqrt{2\pi \, | \, S_{k+1}^{j} \, |}} \exp[-\frac{1}{2}(e_{k+1}^{j})^{T} (S_{k+1}^{j}) e_{k+1}^{j}] \tag{3.34}$$

- model probability update

$$\mu_{k+1}^{j} = \frac{1}{c} L_{k+1}^{j} \bar{c}_{j} \tag{3.35}$$

where

$$c = \sum_{i=1}^{N_m} L_{k+1}^{i} \bar{c}_{i} \tag{3.36}$$

Step 5. combination of estimates

- overall state estimates

$$d_{k+1|k+1} = \sum_{j=1}^{N_m} d_{k+1|k+1}^{j} \mu_{k+1}^{j} \tag{3.37}$$

- overall error covariance estimate

$$C_{k+1|k+1} = \sum_{j=1}^{N_m} [C_{k+1|k+1}^{j} + (d_{k+1|k+1} - d_{k+1|k+1}^{j})(d_{k+1|k+1} - d_{k+1|k+1}^{j})^{T}]\mu_{k+1}^{j} \tag{3.38}$$

3.3 Numerical results for front points

In order to evaluate the estimation performance of the IMM scheme, computer simulations were carried out for the front points approach with the evolution model shown in Figure 3.2. Here the circular domain of diameter 28*cm* is considered around which 16 electrodes of width 2.5*cm* are mounted. While generating the data, the conductivity of each region is assumed to be known and is set to $1/(10000\Omega cm)$ for the upper region and $1/(100\Omega cm)$ for the lower region. The standard Tikhonov method is used as regularion method with regularization matrix $L_R = I \in \mathbb{R}^{\Lambda\times\Lambda}$ and $\alpha_R = 0.01$, respectively.

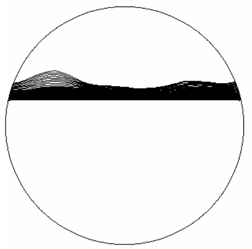

Figure 3.2. Evolution of the boundary interface.

The FEM mesh and current injection patterns are same as considered in the previous chapter. The only difference is a faster evolution model. We have considered a total of 200 patterns whereas in the previous chapter a total of 1400 patterns are considered for 10 front points. A faster evolution model will affect the reconstruction performance and that is where IMM algorithm will become handy.

In the design of the IMM algorithm, three (N_m) extended Kalman filters with different process noise covariances were used. For simplicity, the covariance matrices were assumed to be time invariant and diagonal; the process noise covariance matrices for EKF1, EKF2 and EKF3 were set to $Q_k^1 = 0.05 I_\Lambda$, $Q_k^2 = 0.03 I_\Lambda$, and $Q_k^3 = 0.01 I_\Lambda$, respectively. Two simulations were considered with varying measurement noise. The covariance matrices for the measurement noise $\bar{R}_k$ for all EKFs were set to $8 \times 10^4 I_E$ when there is 1% white Gaussian noise and $9 \times 10^4 I_E$ when there is 2% white Gaussian noise. For comparison purposes, the same measurement data that is used with IMM is then separately used with each EKF. The initial values of the error covariance matrices ($C_{0|0}^i, i = 1,2,3$) were set to be $0.01 I_\Lambda$. In the IMM, the Markov chain transition probabilities π_{ij} are assumed to be 0.8 for $i = j$ and 0.1 for $i \neq j$. In general, the final results were not vey sensitive to these parameters (e.g., π_{ij} can be between 0.8 and 0.99). As can be expected, the lower (higher) values will yield less (more) error during transient intervals but more (less) error during quiescent periods. The initial model probabilities ($\mu_0^i, i = 1,2,3$) were set to $\frac{1}{3}$.

The reconstruction results for 1% noise are shown in Figures 3.3-3.5. From these reconstructed phase boundaries, it should be pointed out that estimation performance of the single EKF depends heavily on the magnitude of the process noise covariance in the random-walk model. It is difficult to choose an appropriate process noise covariance matrix *a priori* in EKF since we have no information on the evolution of the phase boundary. The fourth column in Figure 3.3 shows the reconstructed phase boundaries obtained by the proposed IMM-based scheme. As can be seen, the IMM yields better estimates than the individual EKFs. Although three dynamic models were used in the design of the IMM, one can have flexibility in choosing the number and parameters of the dynamic models. The model probability ($\mu_k^i, i = 1, 2, 3$) of each single EKF employed in the IMM is depicted in Figure 3.4. As can be seen, the model probabilities of the IMM scheme switch rapidly since each EKF has its own dominant interval and the IMM decides which model gives the best fit with the measurements. In this case the EKF2 is dominant throughout, while the EKF1 is significant for some intervals. The reconstruction results for 2% noise are shown in Figures 3.6-3.8. The results are similar to the first simulation and the visual quality of the reconstructed boundaries from the IMM approach (4th column of Figure 3.7) is enhanced as compared to that of the boundaries of each of the EKFs. Also, EKF2 is dominant in all the intervals. Another advantage of IMM approach can be seen by analyzing the $RMSE_d$ comparison in Figures 3.5 and 3.8. It can be seen that $RMSE_d$ is significantly lower for IMM scheme as compared to individual EKFs. An interesting thing to note here is that even though IMM favors EKF1 over EKF3 (Figure 3.7), $RMSE_d$ is lower for EKF3 than EKF1 when run separately (Figure 3.8). This can happen because in IMM the input to each EKF is obtained as a result of mixing of state and covariance estimates, therefore, the performance of EKF1 is different when embedded in IMM and when used separately. However, on the average, IMM performs better than the individual EKFs.

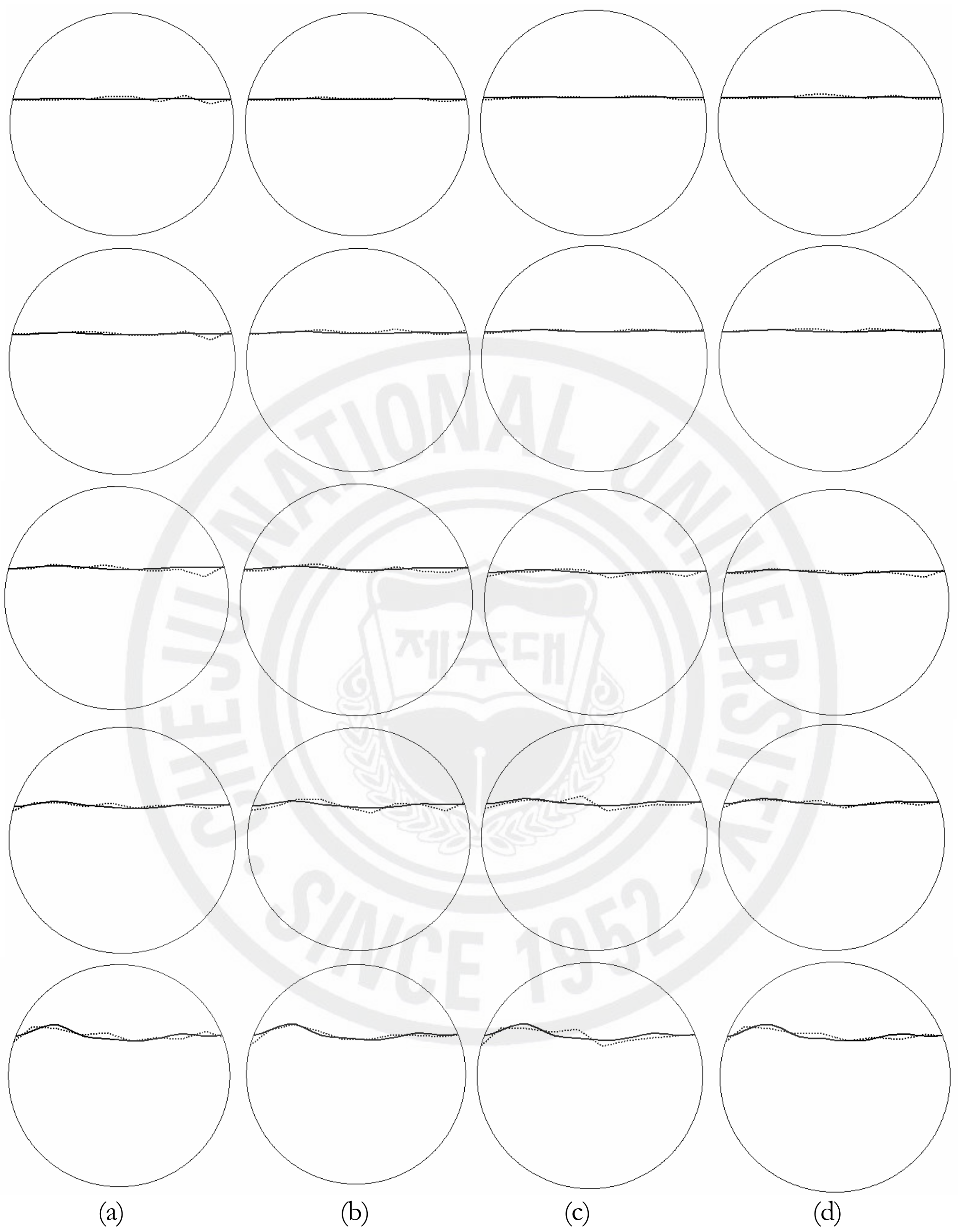

Figure 3.3. The reconstructed phase boundaries for 1% noise. The true boundaries are solid lines and the reconstructed boundaries are dotted lines: (a) boundaries reconstructed by the EKF1; (b) boundaries reconstructed by the EKF2; (c) boundaries reconstructed by the EKF3; and (d) boundariers reconstructed by the IMM.

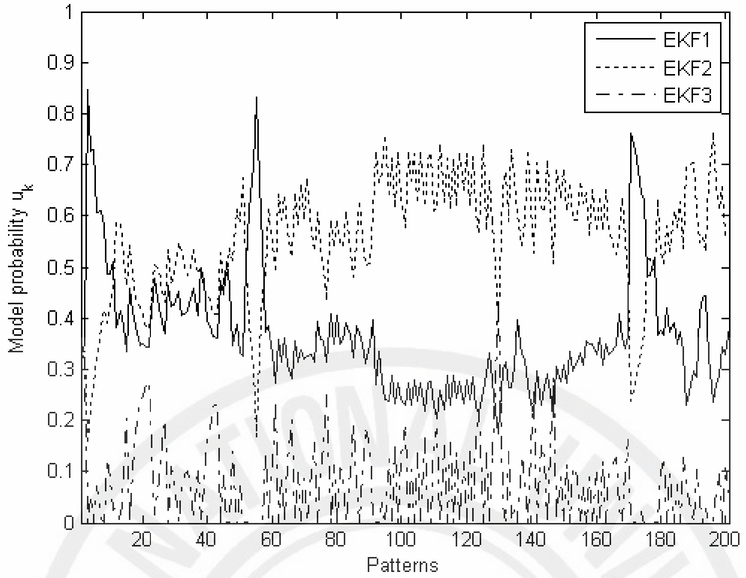

Figure 3.4. Model probabilites of each model for 1% noise.

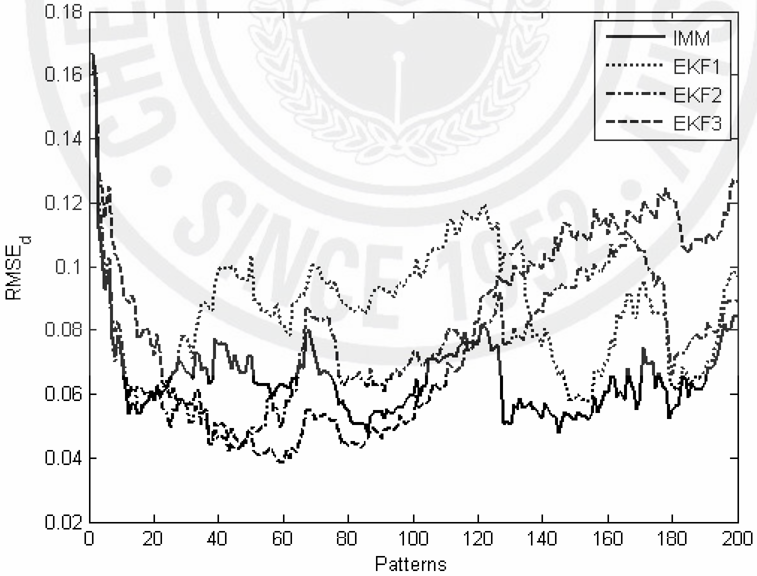

Figure 3.5. $RMSE_d$ comparison between IMM and different EKFs for 1% noise.

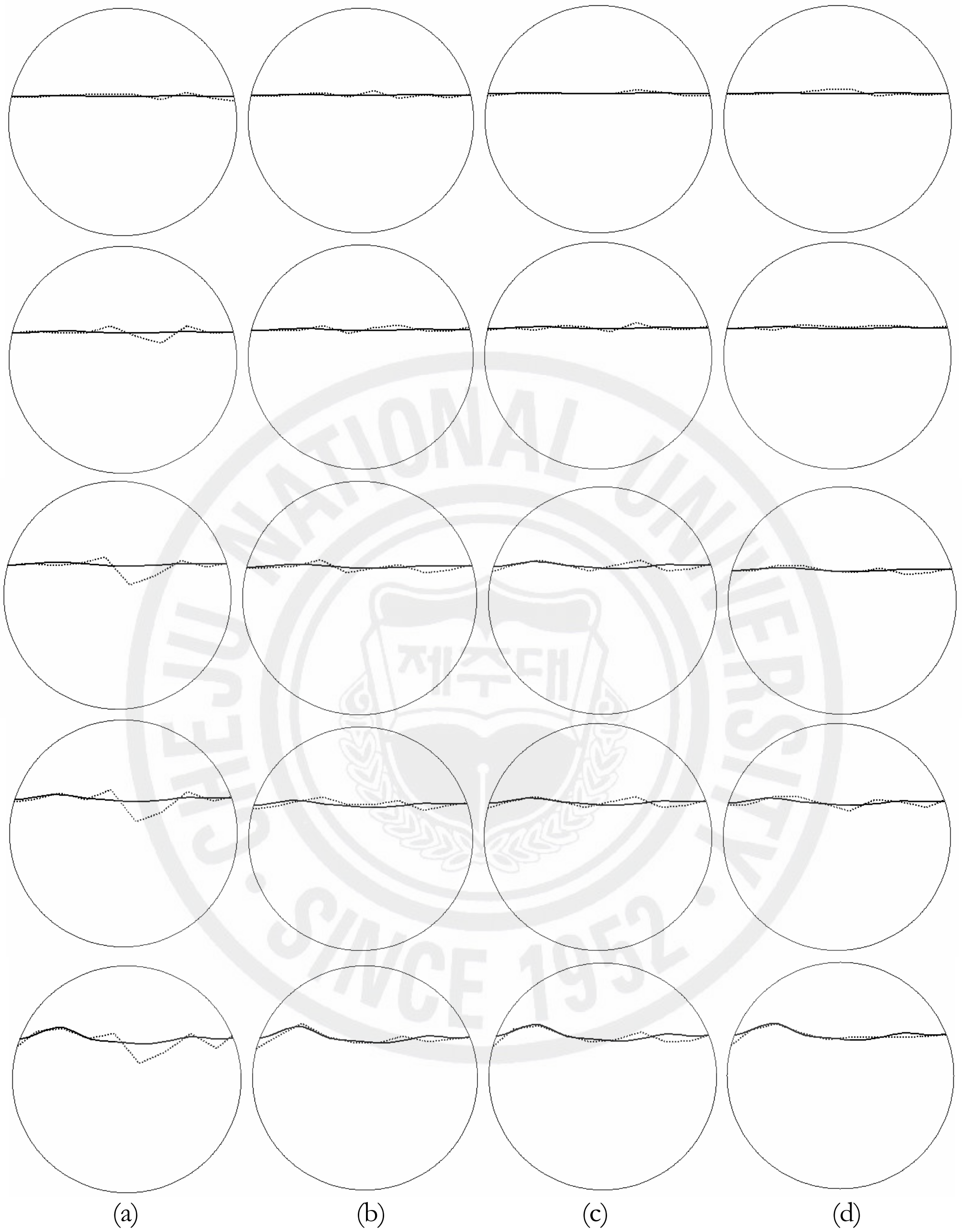

Figure 3.6. The reconstructed phase boundaries for 2% noise. The true boundaries are solid lines and the reconstructed boundaries are dotted lines: (a) boundaries reconstructed by the EKF1; (b) boundaries reconstructed by the EKF2; (c) boundaries reconstructed by the EKF3; and (d) boundariers reconstructed by the IMM.

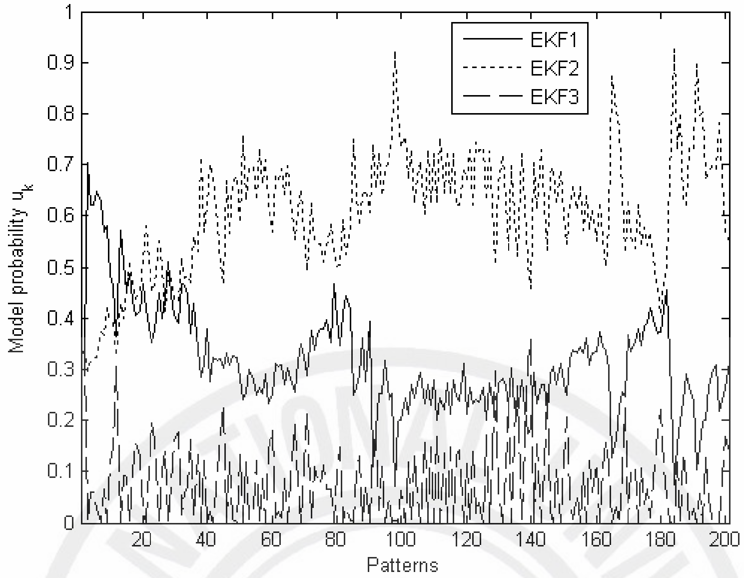

Figure 3.7. Model probabilites of each model for 2% noise.

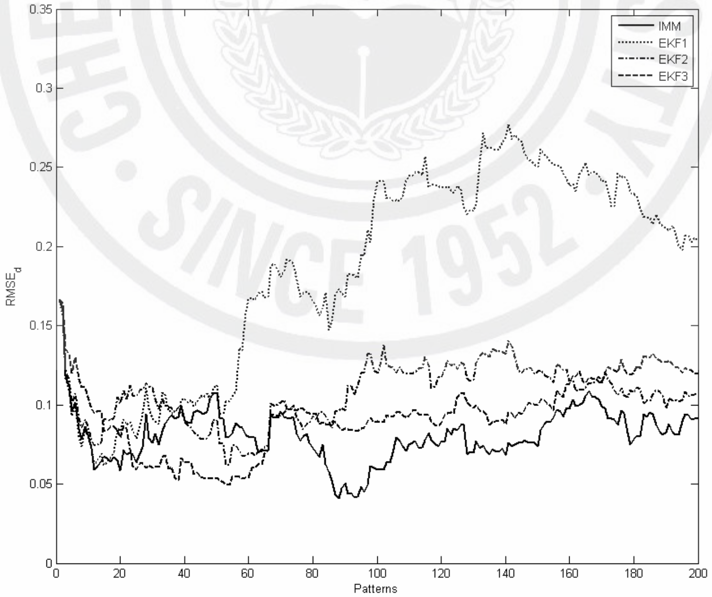

Figure 3.8. $RMSE_d$ comparison between IMM and different EKFs for 2% noise.

4 KINEMATIC MODELS FOR NONSTATIONARY ELLIPTIC REGION BOUNDARIES

In this chapter, kinematic models for dynamic electrical impedance tomography shape estimation of regions of known conductivities based on extended Kalman filter. The interest lies in the estimation of shape of air bubbles and conductive liquid in the industrial pipelines.

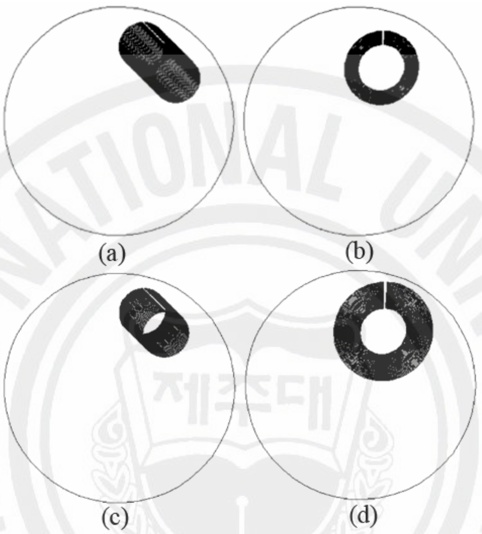

Figure 4.1. Scenarios for kinematic model: (a) bubble is moving with constant velocity; (b) bubble is expanding with constant velocity; (c) bubble is moving with constant acceleration; and (d) bubble is expanding with constant acceleration. Transient boundaries are superimposed onto each other.

At the bare minimum, four different types of scenarios are identified as shown in Figure 4.1. The elliptic object undergoes a transient change in circular domain ($15cm$ in diameter) after each current pattern ($\Delta t = 0.01$). The trigonometric current patterns were injected into the domain. Readings for 3 frames were acquired (93 current injections). In all scenarios, the object and background conductivities were set to $1/(250\times10^6\,\Omega cm)$ and $1/(250\Omega cm)$, respectively. The reason behind taking such a high contrast is to visualize the boundaries of air filled bubbles that have infinite resistivities.

Here, the kinematic model (KM) for the state equation (3.2) , which takes into account the first- and the second-order derivatives of γ of the shape coefficients. Originally the KMs were developed in the target tracking field (Bar-Shalom and Li 1993) to estimate the maneuvering target, in which the acceleration and the jerk are considered as white Gaussian noise for the first- and second- order kinematic models, respectively.

4.1 Kinematic models for movement and expansion

Let us consider the state equation and linearized measurement equation (with Tikhonov regularization included and derived in the same manner as the one for front points, i.e., equation (2.21)) as

$$\gamma_{k+1} = F_k \gamma_k + w_k \tag{4.1}$$

$$\tilde{y}_k = H_k \gamma_k + v_k \tag{4.2}$$

For a bubble moving with constant velocity (Figure 4.1(a)), the required state vector, state matrix and measurement matrix are as follows:

$$\gamma = [\gamma_1^{x_1} \quad \dot{\gamma}_1^{x_1} \quad \gamma_1^{y_1} \quad \dot{\gamma}_1^{y_1} \quad \gamma_1^{x_2} \quad \gamma_1^{y_2} \quad \gamma_1^{x_3} \quad \gamma_1^{y_3}]^T \tag{4.3}$$

$$F_k = \begin{bmatrix} 1 & \Delta t & 0 & 0 & 0 & 0 & 0 & 0 \\ 0 & 1 & 0 & 0 & 0 & 0 & 0 & 0 \\ 0 & 0 & 1 & \Delta t & 0 & 0 & 0 & 0 \\ 0 & 0 & 0 & 1 & 0 & 0 & 0 & 0 \\ 0 & 0 & 0 & 0 & 1 & 0 & 0 & 0 \\ 0 & 0 & 0 & 0 & 0 & 1 & 0 & 0 \\ 0 & 0 & 0 & 0 & 0 & 0 & 1 & 0 \\ 0 & 0 & 0 & 0 & 0 & 0 & 0 & 1 \end{bmatrix} \tag{4.4}$$

$$H_k = \begin{bmatrix} J_k^{(1,1)} & 0 & J_k^{(1,2)} & 0 & J_k^{(1,3)} & J_k^{(1,4)} & J_k^{(1,5)} & J_k^{(1,6)} \\ J_k^{(2,1)} & 0 & J_k^{(2,2)} & 0 & J_k^{(2,3)} & J_k^{(2,4)} & J_k^{(2,5)} & J_k^{(2,6)} \\ \vdots & \vdots & \vdots & \vdots & \vdots & \vdots & \vdots & \vdots \\ J_k^{(32,1)} & 0 & J_k^{(32,2)} & 0 & J_k^{(32,3)} & J_k^{(32,4)} & J_k^{(32,5)} & J_k^{(32,6)} \end{bmatrix} \tag{4.5}$$

For a bubble expanding with constant velocity (Figure 4.1(b)), the required state vector, state matrix and measurement matrix are as follows:

$$\gamma = [\gamma_1^{x_1} \quad \gamma_1^{y_1} \quad \gamma_1^{x_2} \quad \dot{\gamma}_1^{x_2} \quad \gamma_1^{y_2} \quad \gamma_1^{x_3} \quad \gamma_1^{y_3} \quad \dot{\gamma}_1^{y_3}]^T \tag{4.6}$$

$$F_k = \begin{bmatrix} 1 & 0 & 0 & 0 & 0 & 0 & 0 & 0 \\ 0 & 1 & 0 & 0 & 0 & 0 & 0 & 0 \\ 0 & 0 & 1 & \Delta t & 0 & 0 & 0 & 0 \\ 0 & 0 & 0 & 1 & 0 & 0 & 0 & 0 \\ 0 & 0 & 0 & 0 & 1 & 0 & 0 & 0 \\ 0 & 0 & 0 & 0 & 0 & 1 & 0 & 0 \\ 0 & 0 & 0 & 0 & 0 & 0 & 1 & \Delta t \\ 0 & 0 & 0 & 0 & 0 & 0 & 0 & 1 \end{bmatrix} \tag{4.7}$$

$$H_k = \begin{bmatrix} J_k^{(1,1)} & J_k^{(1,2)} & J_k^{(1,3)} & 0 & J_k^{(1,4)} & J_k^{(1,5)} & J_k^{(1,6)} & 0 \\ J_k^{(2,1)} & J_k^{(2,2)} & J_k^{(2,3)} & 0 & J_k^{(2,4)} & J_k^{(2,5)} & J_k^{(2,6)} & 0 \\ \vdots & \vdots & \vdots & \vdots & \vdots & \vdots & \vdots & \vdots \\ J_k^{(32,1)} & J_k^{(32,2)} & J_k^{(32,3)} & 0 & J_k^{(32,4)} & J_k^{(32,5)} & J_k^{(32,6)} & 0 \end{bmatrix} \tag{4.8}$$

For a bubble moving with constant acceleration (Figure 4.1(c)), the required state vector, state matrix and measurement matrix are as follows:

$$\gamma = [\gamma_1^{x_1} \quad \dot{\gamma}_1^{x_1} \quad \ddot{\gamma}_1^{x_1} \quad \gamma_1^{y_1} \quad \dot{\gamma}_1^{y_1} \quad \ddot{\gamma}_1^{y_1} \quad \gamma_1^{x_2} \quad \gamma_1^{y_2} \quad \gamma_1^{x_3} \quad \gamma_1^{y_3}]^T \tag{4.9}$$

$$F_k = \begin{bmatrix} 1 & \Delta t & \frac{1}{2}\Delta t^2 & 0 & 0 & 0 & 0 & 0 & 0 & 0 \\ 0 & 1 & \Delta t & 0 & 0 & 0 & 0 & 0 & 0 & 0 \\ 0 & 0 & 1 & 0 & 0 & 0 & 0 & 0 & 0 & 0 \\ 0 & 0 & 0 & 1 & \Delta t & \frac{1}{2}\Delta t^2 & 0 & 0 & 0 & 0 \\ 0 & 0 & 0 & 0 & 1 & \Delta t & 0 & 0 & 0 & 0 \\ 0 & 0 & 0 & 0 & 0 & 1 & 0 & 0 & 0 & 0 \\ 0 & 0 & 0 & 0 & 0 & 0 & 1 & 0 & 0 & 0 \\ 0 & 0 & 0 & 0 & 0 & 0 & 0 & 1 & 0 & 0 \\ 0 & 0 & 0 & 0 & 0 & 0 & 0 & 0 & 1 & 0 \\ 0 & 0 & 0 & 0 & 0 & 0 & 0 & 0 & 0 & 1 \end{bmatrix} \tag{4.10}$$

$$H_k = \begin{bmatrix} J_k^{(1,1)} & 0 & 0 & J_k^{(1,2)} & 0 & 0 & J_k^{(1,3)} & J_k^{(1,4)} & J_k^{(1,5)} & J_k^{(1,6)} \\ J_k^{(2,1)} & 0 & 0 & J_k^{(2,2)} & 0 & 0 & J_k^{(2,3)} & J_k^{(2,4)} & J_k^{(2,5)} & J_k^{(2,6)} \\ \vdots & \vdots & \vdots & \vdots & \vdots & \vdots & \vdots & \vdots & \vdots & \vdots \\ J_k^{(32,1)} & 0 & 0 & J_k^{(32,2)} & 0 & 0 & J_k^{(32,3)} & J_k^{(32,4)} & J_k^{(32,5)} & J_k^{(32,6)} \end{bmatrix} \tag{4.11}$$

For a bubble expanding with constant acceleration (Figure 4.1(d)), the required state vector, state matrix and measurement matrix are as follows:

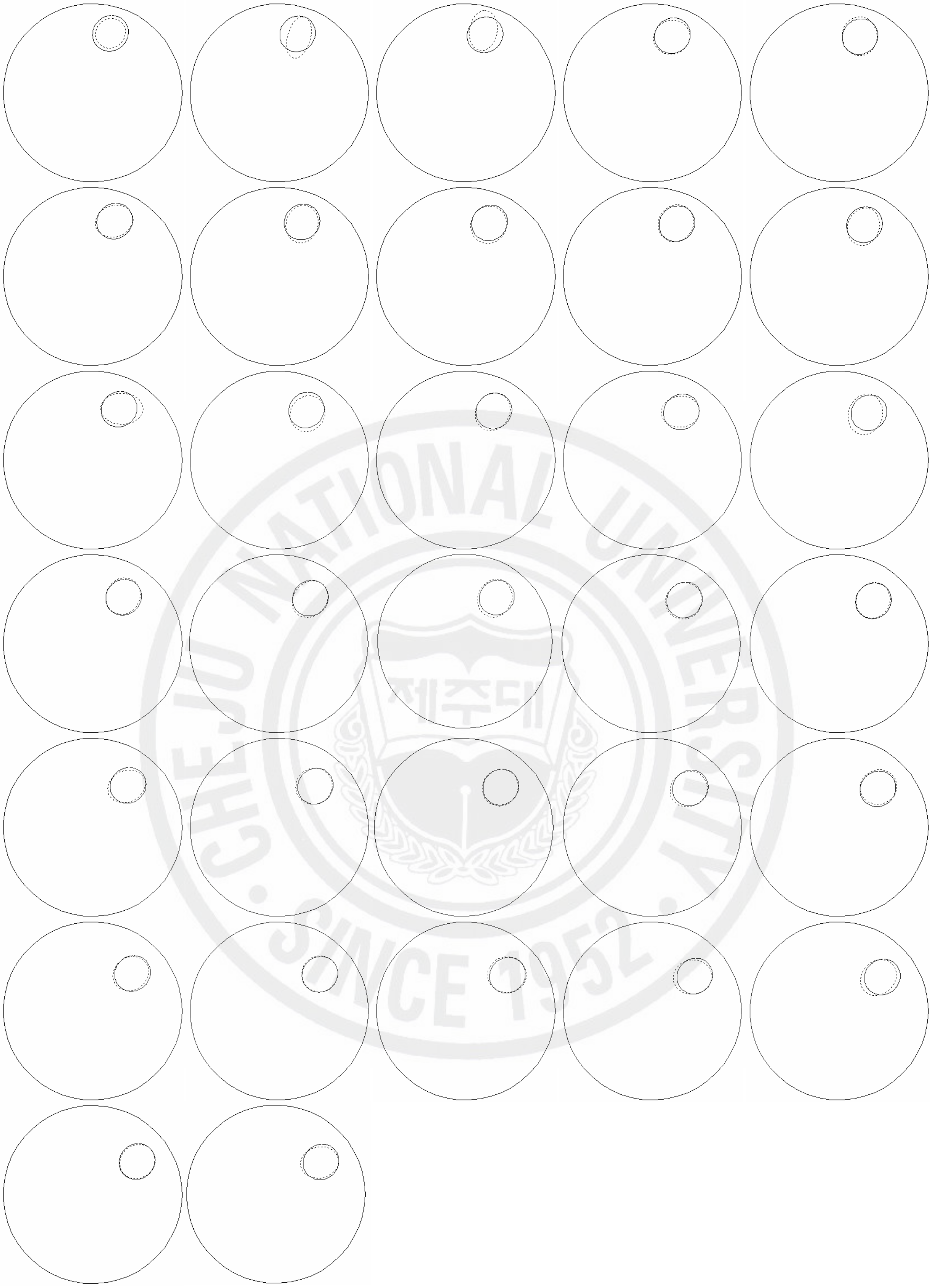

Figure 4.2. Reconstructed boundaries with kinematic model for bubble moving with constant velocity. True boundary is represented by solid line and estimated boundary is represented by dotted line.

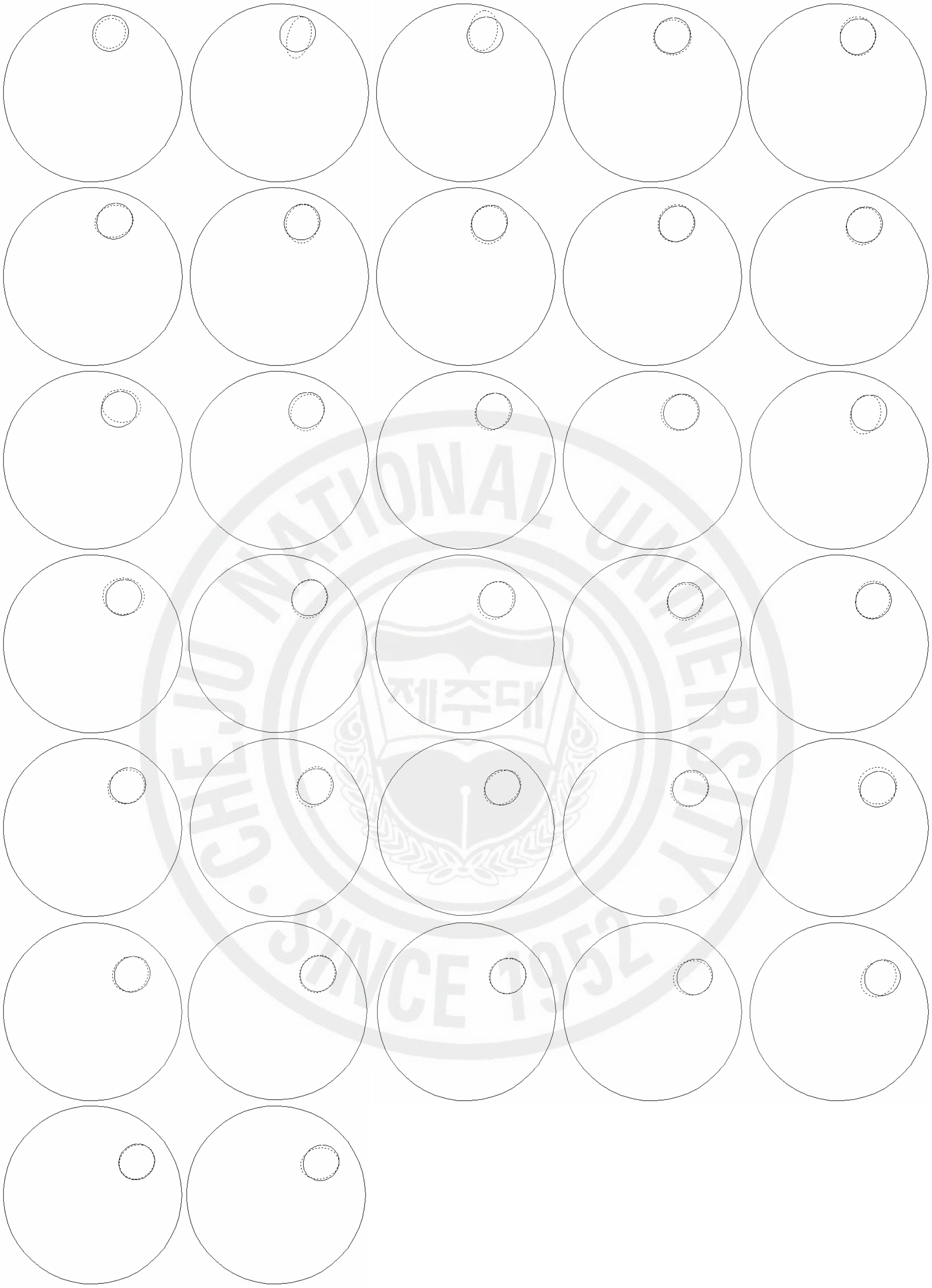

Figure 4.3. Reconstructed boundaries with random-walk model for bubble moving with constant velocity. True boundary is represented by solid line and estimated boundary is represented by dotted line.

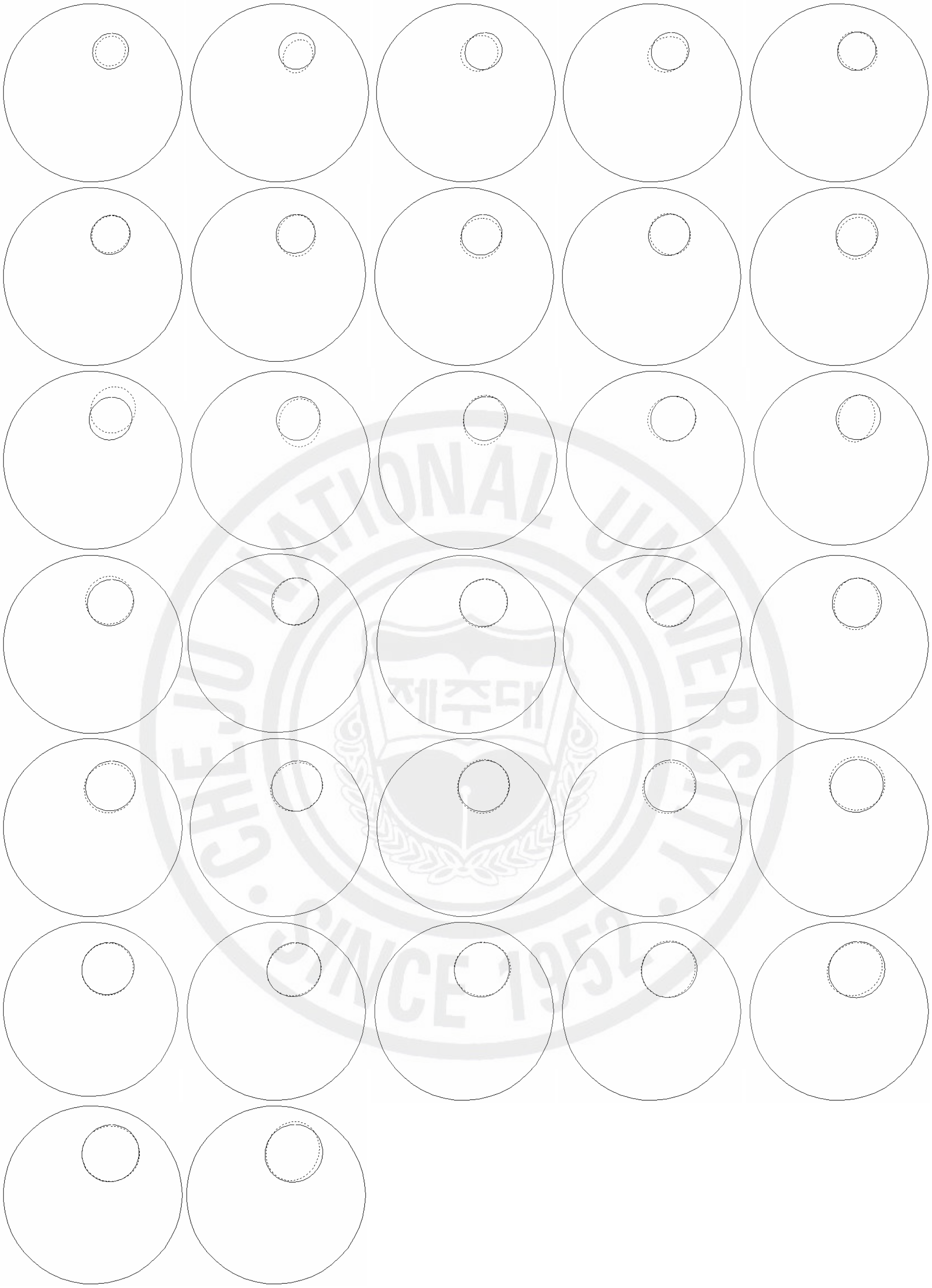

Figure 4.4. Reconstructed boundaries with kinematic model for bubble expanding with constant velocity. True boundary is represented by solid line and estimated boundary is represented by dotted line.

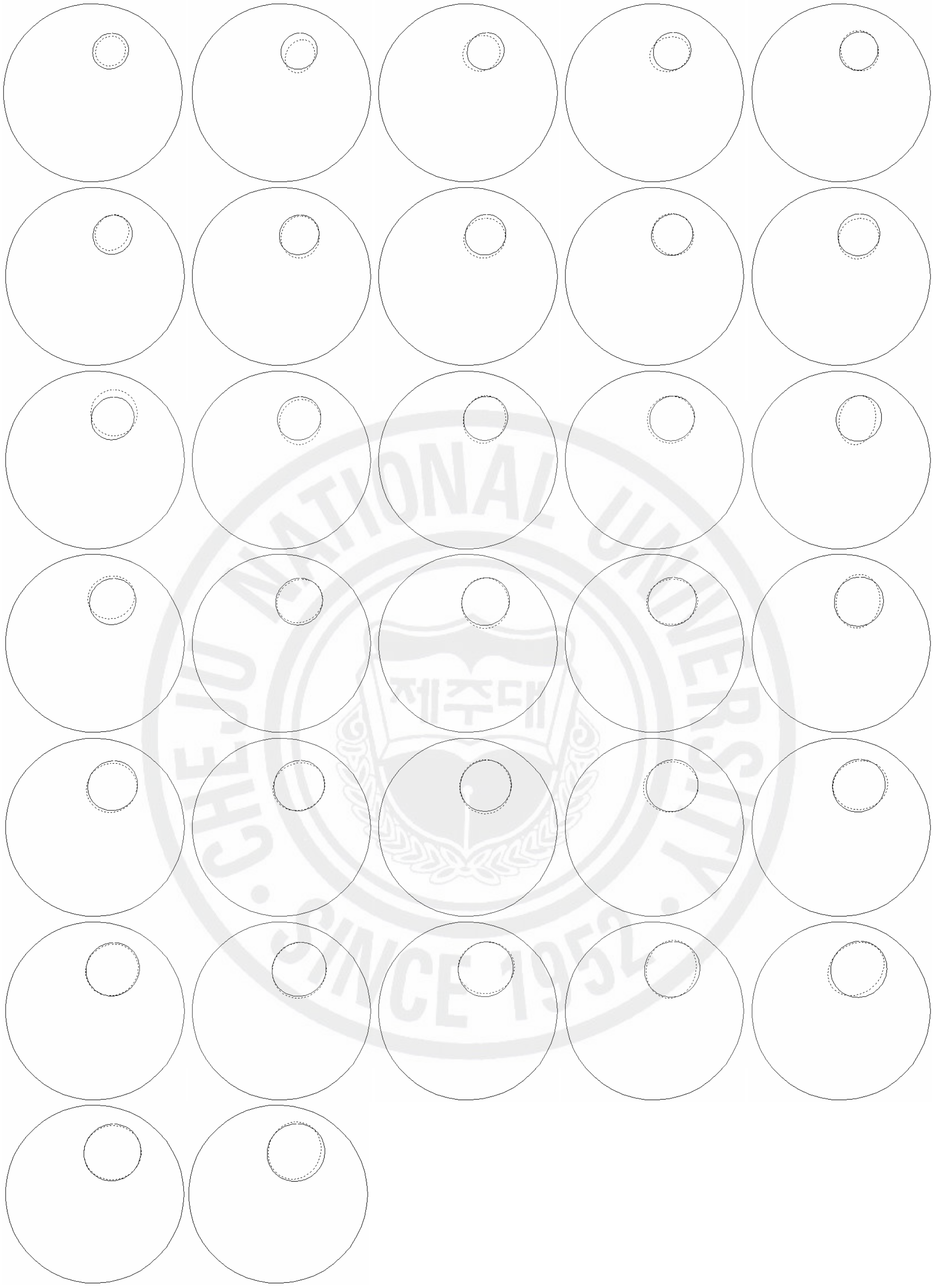

Figure 4.5. Reconstructed boundaries with random-walk model for bubble expanding with constant velocity. True boundary is represented by solid line and estimated boundary is represented by dotted line.

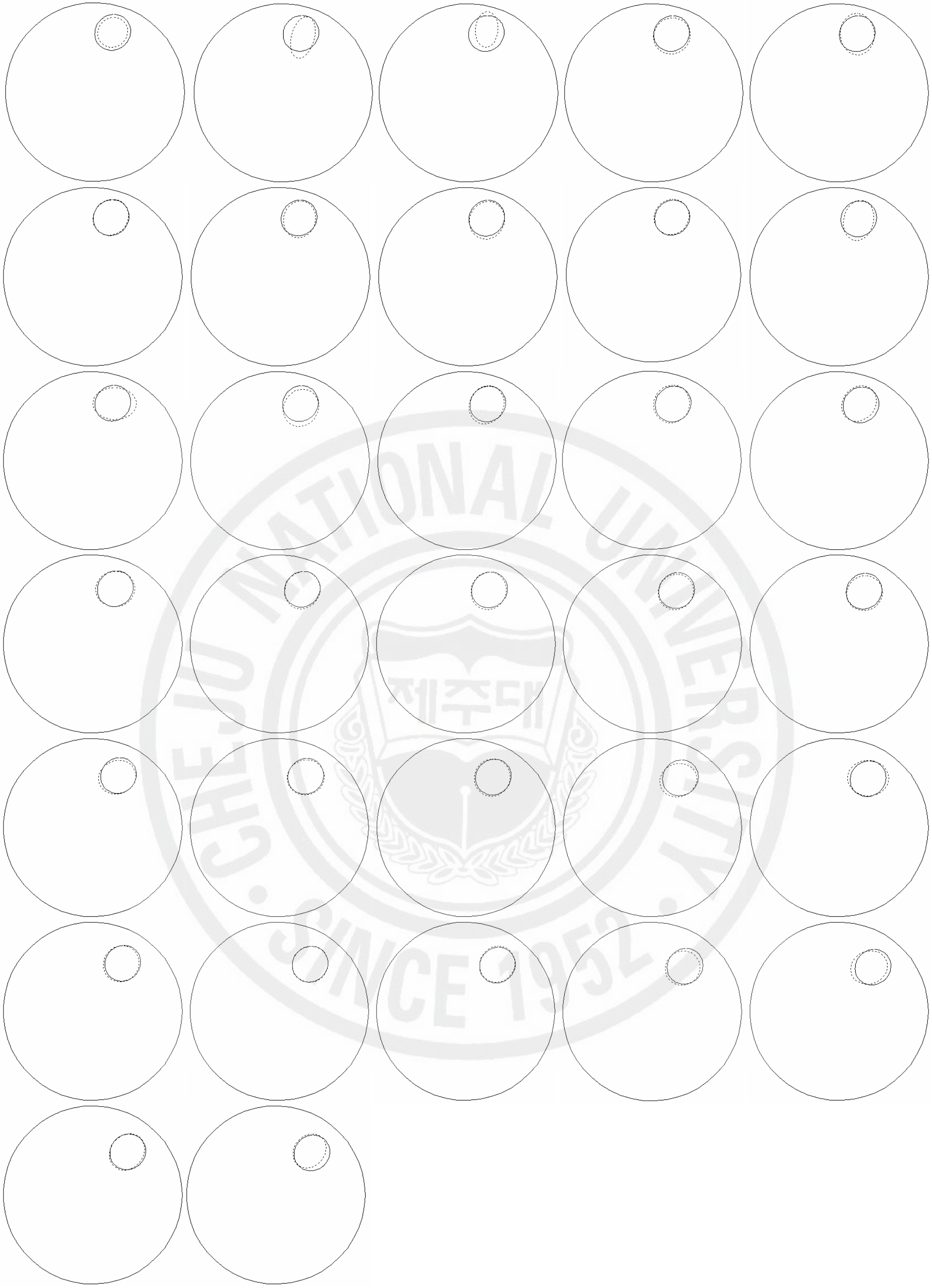

Figure 4.6. Reconstructed boundaries with kinematic model for bubble moving with constant acceleration. True boundary is represented by solid line and estimated boundary is represented by dotted line.

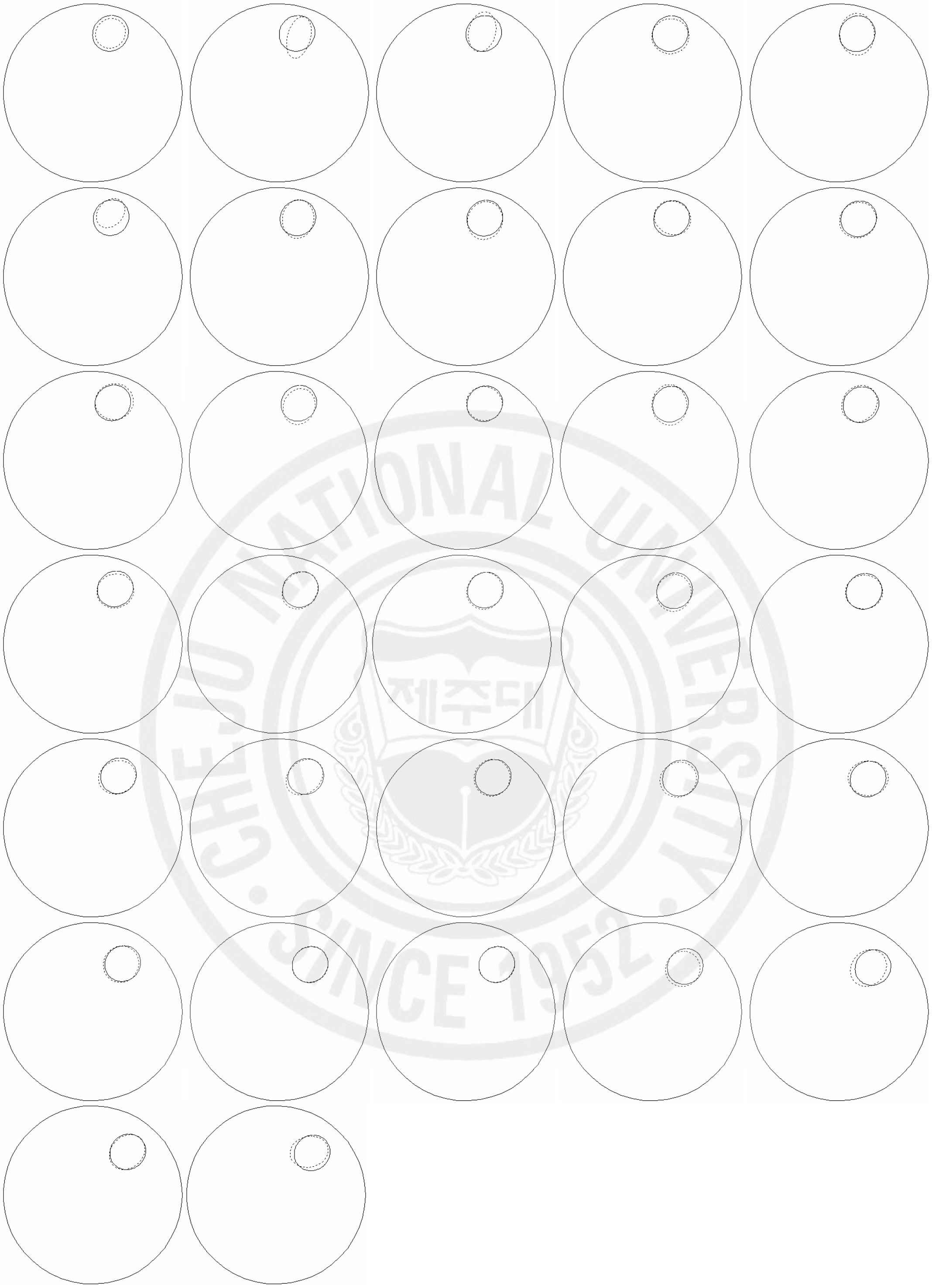

Figure 4.7. Reconstructed boundaries with random-walk model for bubble moving with constant acceleration. True boundary is represented by solid line and estimated boundary is represented by dotted line.

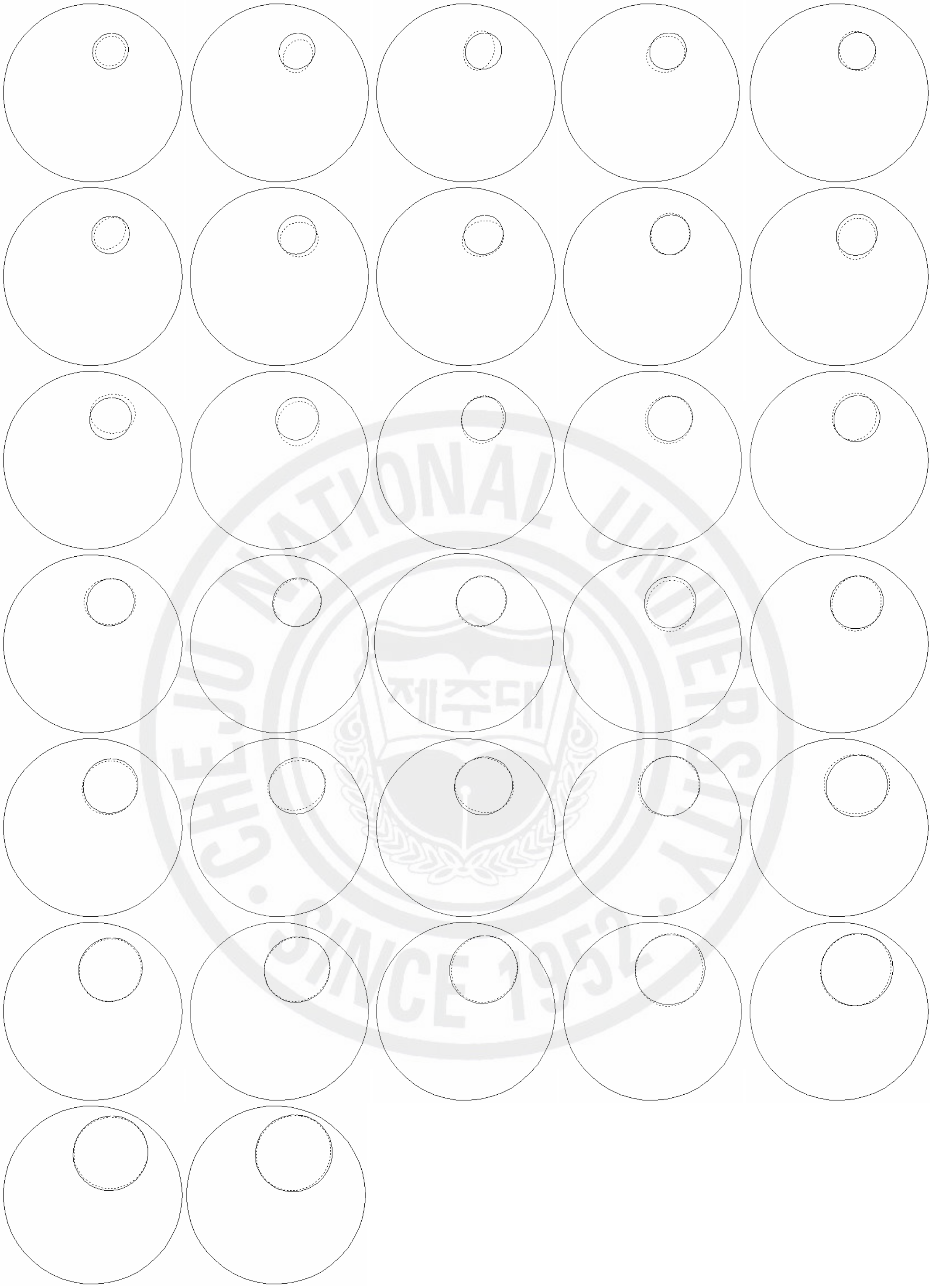

Figure 4.8. Reconstructed boundaries with kinematic model for bubble expanding with constant acceleration. True boundary is represented by solid line and estimated boundary is represented by dotted line.

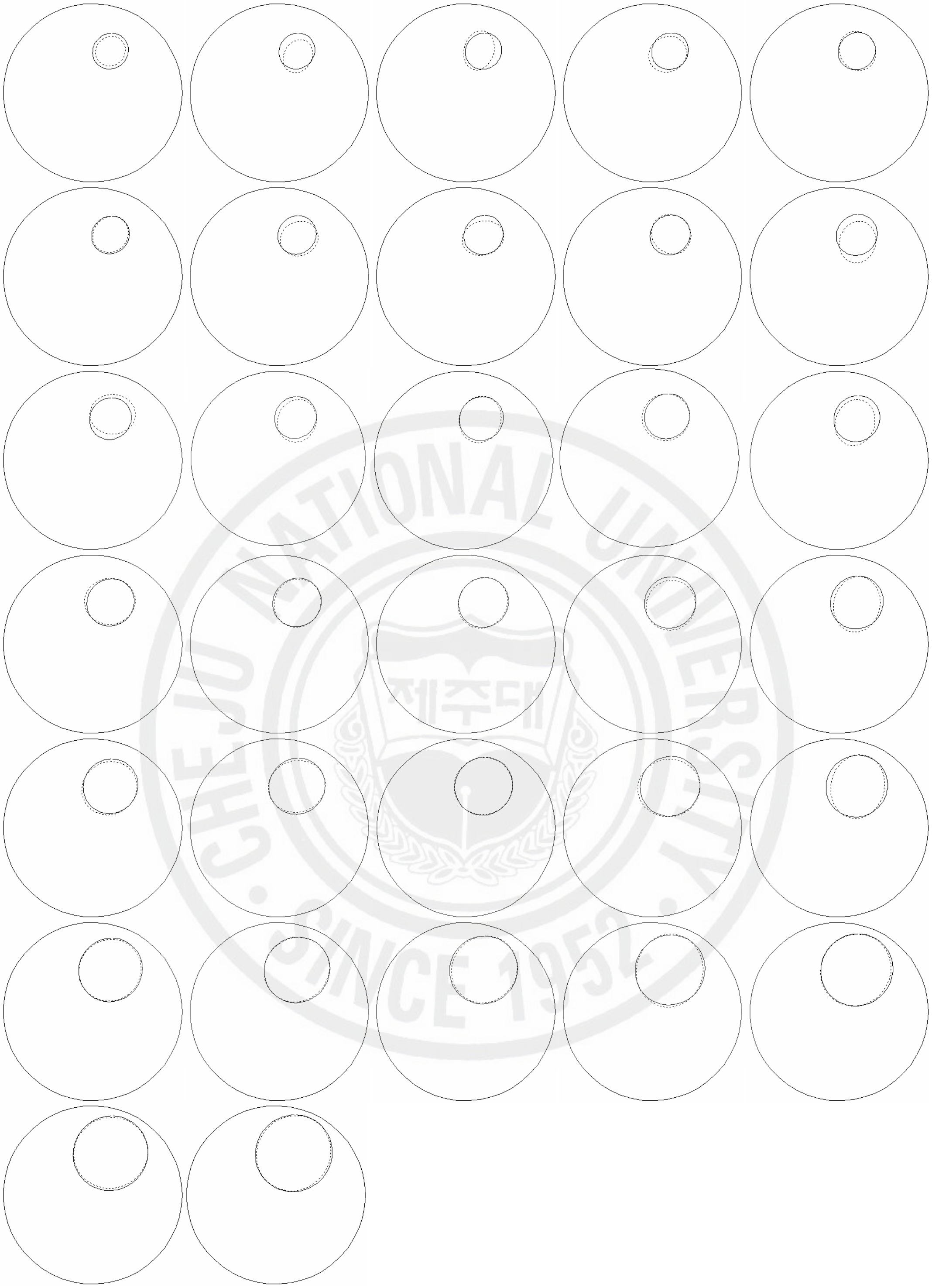

Figure 4.9. Reconstructed boundaries with random-walk model for bubble expanding with constant acceleration. True boundary is represented by solid line and estimated boundary is represented by dotted line.

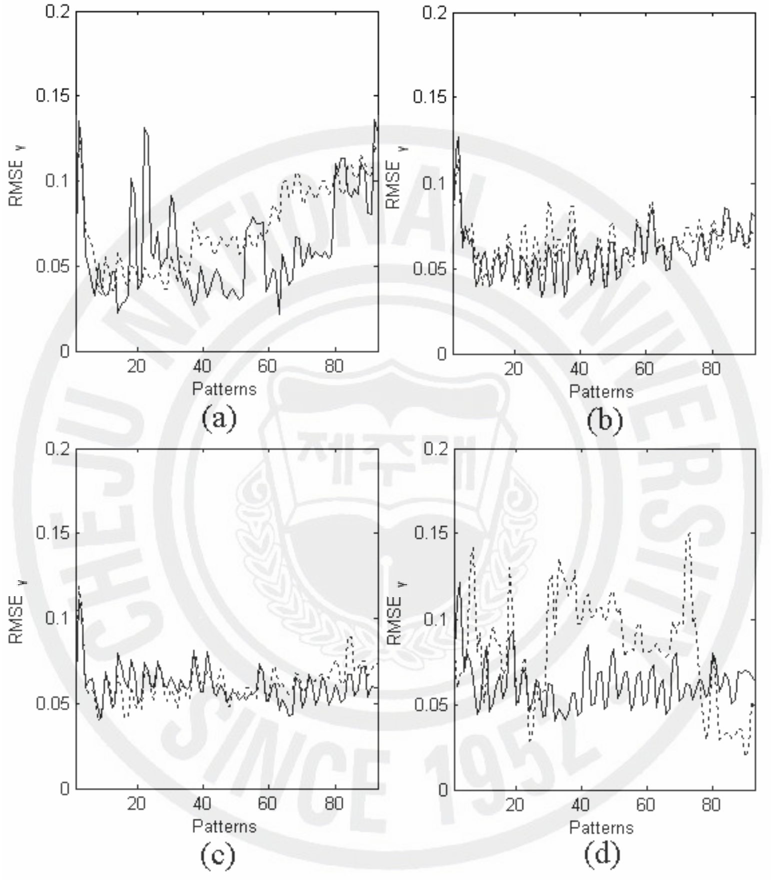

Figure 4.10. RMSE comparison with Monte-Carlo simulation of 10 runs: (a) bubble is moving with constant velocity; (b) bubble is expanding with constant velocity; (c) bubble is moving with constant velocity; and (d) bubble is expanding with constant acceleration. Solid line represents the RMSE with KM whereas dotted line represents the RMSE with random-walk model.

$$\gamma = [\gamma_1^{x_1} \quad \gamma_1^{y_1} \quad \gamma_1^{x_2} \quad \dot{\gamma}_1^{x_2} \quad \ddot{\gamma}_1^{x_2} \quad \gamma_1^{y_2} \quad \gamma_1^{x_3} \quad \gamma_1^{y_3} \quad \dot{\gamma}_1^{y_3} \quad \ddot{\gamma}_1^{y_3}]^T \tag{4.12}$$

$$F_k = \begin{bmatrix} 1 & 0 & 0 & 0 & 0 & 0 & 0 & 0 & 0 & 0 \\ 0 & 1 & 0 & 0 & 0 & 0 & 0 & 0 & 0 & 0 \\ 0 & 0 & 1 & \Delta t & \frac{1}{2}\Delta t^2 & 0 & 0 & 0 & 0 & 0 \\ 0 & 0 & 0 & 1 & \Delta t & 0 & 0 & 0 & 0 & 0 \\ 0 & 0 & 0 & 0 & 1 & 0 & 0 & 0 & 0 & 0 \\ 0 & 0 & 0 & 0 & 0 & 1 & 0 & 0 & 0 & 0 \\ 0 & 0 & 0 & 0 & 0 & 0 & 1 & 0 & 0 & 0 \\ 0 & 0 & 0 & 0 & 0 & 0 & 0 & 1 & \Delta t & \frac{1}{2}\Delta t^2 \\ 0 & 0 & 0 & 0 & 0 & 0 & 0 & 0 & 1 & \Delta t \\ 0 & 0 & 0 & 0 & 0 & 0 & 0 & 0 & 0 & 1 \end{bmatrix} \tag{4.13}$$

$$H_k = \begin{bmatrix} J_k^{(1,1)} & J_k^{(1,2)} & J_k^{(1,3)} & 0 & 0 & J_k^{(1,4)} & J_k^{(1,5)} & J_k^{(1,6)} & 0 & 0 \\ J_k^{(2,1)} & J_k^{(2,2)} & J_k^{(2,3)} & 0 & 0 & J_k^{(2,4)} & J_k^{(2,5)} & J_k^{(2,6)} & 0 & 0 \\ \vdots & \vdots & \vdots & \vdots & \vdots & \vdots & \vdots & \vdots & \vdots & \vdots \\ J_k^{(32,1)} & J_k^{(32,2)} & J_k^{(32,3)} & 0 & 0 & J_k^{(32,4)} & J_k^{(32,5)} & J_k^{(32,6)} & 0 & 0 \end{bmatrix} \tag{4.14}$$

Table 4.1. Extended Kalman filter parameters used in the simulations.

	Simulation 1	Simulation 2	Simulation 3	Simulation 4
Q_k	I_8	I_8	I_{10}	I_{10}
R_k	$200I_E$	$200I_E$	$200I_E$	$200I_E$
$C_{0\|0}$	I_8	I_8	I_{10}	I_{10}

4.2 Numerical Results for Fourier Coefficients

The EKF parameters used in the simulation are shown in Table 4.1. The regularization parameter α_R is set to 0.1 as the contrast ratio between the background and target is very high. Furthermore, in all simulations, zero-mean white Gaussian noise was added to the calculated voltages to generate noisy measurements; the noise level was set to be 1% of the corresponding calculated voltages. The reconstruction results are shown in Figures 4.2-4.9. Here, it should be noted that the profile changes after every current injection, however in the figures, the temporal profile is shown after 3 current patterns with the first image as the initial guess. It can be seen that the estimation quality is quite good especially for the cases when the bubble is moving with constant velocity and when it is expanding with constant acceleration. The RMSE comparison for region boundaries is done between KM and random-walk model for a Monte-Carlo simulations of 10 runs for each scenario (shown in Figure 4.10). From the results, it should be pointed out that the estimation performance of EKF with KM is better than random-walk model in most cases. For the case when the bubble is moving with constant velocity, there is a significant difference in RMSE values of KM and random-walk model between 40th and 80th current patterns and for the bubble expanding with constant acceleration, there is a significant difference between the 35th and 75th current patterns. It is anticipated that the simulation results with KM set the necessary grounds for IMM scheme in which EKFs with different evolution models(kinematic models) can be used to give the best estimates of all models.

5 NONSTATIONARY PHASE BOUNDARY ESTIMATION USING UNSCENTED KALMAN FILTER

The EKF has become a standard technique used in a number of nonlinear estimation and machine learning applications, e.g., estimating the state of nonlinear dynamic system, estimating parameters for nonlinear system identification (learning weights of a neural network) and dual estimation (Expectation Maximization (EM) algorithm) where both states and parameters are estimated simultaneously. However, in EKF, the state distribution is approximated by a Gaussian random variable (GRV), which is then propagated analytically through the first-order linearization of the nonlinear system. This can introduce large errors in the true posterior mean and covariance of the transformed GRV, which may lead to suboptimal performance and sometimes divergence of the filter. To overcome these difficulties, the unscented transform (UT) was developed by Julier and Uhlmann (1997) and subsequently in Julier and Uhlmann (2004) as a method to propagate mean and covariance information through a nonlinear transformation. It is more accurate, easier to implement, and uses the same order of calculations as linearization. The unscented Kalman filter (UKF) addresses this problem by carefully choosing sample points instead of GRV, and which when propagated through the true nonlinear system, captures the posterior mean and covariance accurately to the 3rd order (Taylor series expansion) for any nonlinearity. The EKF, in contrast, only achieves first-order accuracy. Also, the linearization in EKF is possible only if the Jacobian matrix exists. However, this is not always the case. Some systems contain discontinuities in process model, and in another case, the Jacobian matrices can be very difficult and error-prone process and in most cases introduce human coding errors that undermine the performance. Remarkably, the computational complexity of the UKF is the same order as that of EKF as mentioned in Julier and Uhlmann (2004).

5.1 Unscented Kalman filter

In order to derive UKF, the linear state and nonlinear measurement equations are as follows:

$$x_k = F_{k-1}x_{k-1} + w_{k-1} \tag{5.1}$$

$$V_k = U_k(x_k) + v_k \tag{5.2}$$

where $w_k \in \mathbb{R}^{N\times 1}$ and $V_k \in \mathbb{R}^{E\times 1}$ are assumed to be white Gaussian noise with covariance $Q_k = E[w_k w_k^T]$ and $R_k = E[v_k v_k^T]$ respectively. Here x_k is a generalized representation employing either of the front points d_k and the Fourier coefficients γ_k. Also, $U_k(x_k)$ is the forward solver to obtain boundary voltages. Given the stochastic nonlinear state-space model, the unscented Kalman filter algorithm (Julier and Uhlmann 2004) is as follows:

Initialize with:

$$\hat{x}_0 = E[x_0] \tag{5.3}$$

$$C_0 = E[(x_0 - \hat{x}_0)(x_0 - \hat{x}_0)^T] \tag{5.4}$$

$$\hat{x}_0^a = E[x^a] = [\hat{x}_0^T \quad 0 \quad 0]^T \tag{5.5}$$

$$C_0^a = E[(x_0^a - \hat{x}_0^a)(x_0^a - \hat{x}_0^a)^T] = \begin{bmatrix} C_0 & 0 & 0 \\ 0 & Q_0 & 0 \\ 0 & 0 & R_0 \end{bmatrix} \tag{5.6}$$

for $k \in \{1, \ldots, \infty\}$

Calculate sigma points:

$$\chi_{k-1}^a = \left[\hat{x}_{k-1}^a \quad \hat{x}_{k-1}^a + \sqrt{(N_s + \lambda_s) C_{k-1}^a} \quad \hat{x}_{k-1}^a - \sqrt{(N_s + \lambda_s) C_{k-1}^a} \right] \tag{5.7}$$

Time Update:

$$\chi_{k|k-1}^x = F_{k-1} \cdot \chi_{k-1}^x + \chi_{k-1}^w \tag{5.8}$$

$$\hat{x}_k^- = \sum_{i=0}^{2N_s} W_i^{(m)} \chi_{i,k|k-1}^x \tag{5.9}$$

$$C_k^- = \sum_{i=0}^{2N_s} W_i^{(c)} [\chi_{i,k|k-1}^x - \hat{x}_k^-][\chi_{i,k|k-1}^x - \hat{x}_k^-]^T \tag{5.10}$$

$$\psi_{k|k-1} = U_k(\chi_{k|k-1}^x) + \chi_{k-1}^v \tag{5.11}$$

$$\hat{U}_k^- = \sum_{i=0}^{2N_s} W_i^{(m)} \psi_{i,k|k-1} \tag{5.12}$$

Measurement Update:

$$C_{\tilde{U}_k \tilde{U}_k} = \sum_{i=0}^{2N_s} W_i^{(c)} [\psi_{i,k|k-1} - \hat{U}_k^-][\psi_{i,k|k-1} - \hat{U}_k^-]^T \tag{5.13}$$

$$C_{x_k U_k} = \sum_{i=0}^{2N_s} W_i^{(c)} [\chi_{i,k|k-1}^x - \hat{x}_k^-][\psi_{i,k|k-1} - \hat{U}_k^-]^T \tag{5.14}$$

$$\mathrm{K}_k = C_{x_k U_k} C_{\tilde{U}_k \tilde{U}_k}^{-1} \tag{5.15}$$

$$\hat{x}_k = \hat{x}_k^- + \mathrm{K}_k (V_k - \hat{U}_k^-) \tag{5.16}$$

$$C_k = C_k^- - \mathrm{K}_k C_{\tilde{U}_k \tilde{U}_k} \mathrm{K}_k^T \tag{5.17}$$

where

$x^a = [x^T \quad w^T \quad v^T]^T$, $\chi^a = [(\chi^x)^T \quad (\chi^w)^T \quad (\chi^v)^T]^T$, $\lambda_s = \alpha_s{}^2 (N_s + \kappa_s) - N_s$ is composite scaling parameter, α_s determines the spread of sigma points (is usually set to a small positive value e.g., $10^{-4} \le \alpha_s \le 1$). The κ_s is secondary scaling parameter (is usually set to 0 or $3 - N_s$) and β_s is used to incorporate prior knowledge of the distribution of x (for Gaussian distribution, β_s =2 is optimal). Weights W_i are given by

$$W_0^{(m)} = \lambda_s / (N_s + \lambda_s) \tag{5.18}$$

$$W_0^{(c)} = \lambda_s / (N_s + \lambda_s) + (1 - \alpha_s{}^2 + \beta_s) \tag{5.19}$$

$$W_i^{(m)} = W_i^{(c)} = 1/\{2(N_s + \lambda_s)\}, \; i = 1, \ldots, 2N_s \tag{5.20}$$

where $N_s = 2N + E$, N is the dimension of Fourier coefficients or Front Points and E is the total number of electrodes. The above mentioned computational procedure to compute the Fourier coefficients is also explained in block diagram in Figure 5.2. Here, the augmented state vector $\hat{\boldsymbol{x}}^{\boldsymbol{a}}$ and the augmented covariance matrix C^a is updated when the voltage measurement V_k becomes available at *k*th iteration. Two significant covariance matrices shown in Figure 5.2 are $C_{\tilde{U}\tilde{U}}$ and C_{xU}. During the iterative process $C_{\tilde{U}\tilde{U}}$ will be reduced so that the transformed sigma points (also putting Figure 5.1 in perspective) move towards the cluster mean. With the introduction of the measurement data V_k, the cluster mean will then move further towards the true mean and as a consequence C_{xU} will be reduced. Here, it should be noted that if the target is static during the application of some current patterns then the transformed sigma points will move towards the true mean and then spread again whenever the target changes its position. Therefore, the trade-off from performance standpoint is how many current patterns should be used and how fast should be the dynamic changes for UKF to capture them.

This method significantly differs from general Monte-Carlo sampling methods which require more sample points in an attempt to propagate an accurate (possibly non-Gaussian) distribution of state. The UKF results in approximations that are accurate to the 3rd order for Gaussian inputs for all nonlinearities. For non-Gaussian inputs, approximations are accurate to at least the 2nd order, with the accuracy of third and higher order moments determined by the choice of α_s and β_s in equation (5.19). The proof of this is provided in Julier and Uhlmann (2004). The UKF used in this study consists of an augmented state vector that contains both the process noise vector and the measurement noise vector. The reason behind taking the augmented state is to consider process and measurement noises with non-zero means. However, if the noise is additive and white Gaussian with zero-mean, one can choose a much simpler form without taking the augmented state.

The complexity of UKF algorithm is $(N_s)^3$, where N_s is the dimension of augmented state. This has the same complexity as EKF. A number of other variations are also possible. For example, the matrix square root, which is implemented directly using a Cholesky factorization, is in general order $(N_s)^3/6$. However, the covariance matrices are expressed recursively, and thus the square-root can be computed in the order $E\times(N_s)^2$ (E is the dimension of the voltage vector V_k) by performing a recursive update on the Cholesky factorization. Such kind of UKF is called square-root UKF and its implementation is covered in Van der Merwe and Wan (2001). For practical purposes, the alternatives are then to use the parallel implementation for sigma points calculation, to use limited measurement data, or to use the square-root UKF with lower complexity.

5.2 Numerical and experimental results for Fourier coefficients

In order to evaluate the performance of UKF, numerical and experimental studies were performed and the performance was assessed in comparison to extended Kalman filter (EKF) which is most often used as a dynamic inverse solver. The EKF uses Tikhonov regularization with regularization parameter α_R and regularization matrix L_R as identity matrix. The experimental setup shown in Figure 5.3 consists of a circular phantom with a radius of $40mm$ and a height of $80mm$ was considered around which L=32 electrodes (each of length 6 mm) were mounted. Two different meshes (Figure 5.4) were used for forward (2121 nodes and 3984 elements) and inverse solver (563 nodes and 993 elements) so that inverse crime is avoided in numerical simulations. As for the current injection protocol, opposite current patterns are used. Traditionally, for 32 electrodes' configuration, there are 16 opposite current patterns. However, since the goal of the current research is to use UKF in dynamic settings, a subset of opposite current patterns is considered in each image frame.

For numerical simulations, two scenarios are considered and their evolution models are shown in Figure 5.5. In both scenarios, a very high contrast ratio between the background ($1/(300\times10^9\,\Omega cm)$) and target ($1/(330\Omega cm)$) is maintained. Also, a total of N=6 Fourier coefficients are reconstructed in the inverse solver that can represent an elliptic object and also meet the requirements of this study. In Figure 5.5(a), in scenario 1, a circular target located in the south moves east at first and then towards north along the boundary until it stops just above the center. It then starts to expand and takes an elliptic shape. Here, a total of 64 image frames (a hypothetical number representing a frame in which the target remains static) are considered where each frame consists of one current pattern. i.e., target changes its position after every current pattern. Furthermore, the measurement data obtained is perturbed with 1%, 2% and 3% relative white Gaussian noise so as to emulate the real situations. The scenarios are then reconstructed with both EKF and UKF.

The parameters used in scenario 1 for both UKF and EKF are shown in Table 5.1. The reconstructed results and RMSE comparison are shown in Figures 5.6-5.11. The reconstructed profiles in Figures 5.6, 5.8, and 5.10 are shown after every 4 current patterns. For the case where measurement data is perturbed with 1% white Gaussian noise, it is noted that UKF is performing remarkably well in estimating the phase boundary. EKF, on the other hand, is trailing behind after application of each current pattern. However, it is noted that in the later part of the simulation, when the target is static and only expanding, the difference between UKF and EKF is a bit less. From the RMSE comparison for 1% white Gaussian noise case, it can be noted that on the average, the RMSE values for UKF are around 0.1 whereas for EKF, they are around 0.3. It can be established that a performance gain of 3 times is a marked improvement. Another key point is that UKF has a smaller transition period in the start as compared to EKF, and the difference in the transition periods between the two filters grows exponentially with the increase in measurement noise. Therefore, for 2% white Gaussian noise case, it can be seen in Figure 5.9 that the first stable estimate for UKF is obtained around the 5th current pattern and for EKF, it is obtained around the 20th current pattern. As for the 3% white Gaussian noise case, the first stable estimate for UKF is obtained around the 15th current pattern, whereas for EKF, it is around the 35th current pattern. From the reconstructed images of Figure 5.8 for 2% white Gaussian noise case, it can be observed that the performance of UKF is better than EKF. The reconstruction results for 3% white Gaussian noise show that EKF has nearly failed whereas UKF is still giving a satisfactory performance. Furthermore, UKF is estimating the position well and the only problem is the shape of the target. However, that is expected in noisy scenarios.

In scenario 1, the emphasis was more on the movement of the target and less on the expansion of the target. Therefore, scenario 2 is considered, whose evolution model is given in Figure 5.5(b), in which a target initially circular located in south-west, moves north and changes its shape after the application of every current pattern. Here, a total of 48 image frames are considered and in each image frame, one opposite current pattern is used. The parameters used in both UKF and EKF are shown in Table 5.2. The reconstructed results and RMSE comparison are shown in Figures 5.12-5.17. The reconstructed profiles in Figures 5.12, 5.14, and 5.16 are shown after every 4 current patterns. Here, the changes in the position are not abrupt, therefore, it is anticipated from the first scenario's expansion that the difference between UKF and EKF will be small, however, UKF will still be better in terms of reconstructed image and RMSE. And so, for the 1% white Gaussian noise case, the reconstructed image quality is almost similar for both filters but UKF is slightly better than EKF. In terms of RMSE (Figure 5.13), UKF (average RMSE is around 0.05) is performing 2 times better than EKF (average RMSE is around 0.1). Similarly, for 2% and 3% white Gaussian noise cases, in terms of RMSE (Figures 5.15 and 5.17), the difference between UKF and EKF is small as compared to scenario 1, however, UKF is still performing better than EKF after the application of every current pattern. A similar thing that is already observed in scenario 1 can also be seen in scenario 2 and that is the difference in transition period for higher noise levels.

From the simulation results, it can be established that UKF has performance gains over EKF for processes in which the dynamic changes are abrupt and that it is also possible to model boundaries of air bubbles. Therefore, both UKF and EKF are put to use in experimental studies by considering plastic targets in saline water (with a resistivity of $330\Omega cm$). In Figure 5.3(c), the possible positions of the plastic targets are shown in the phantom. Since experimental results are a bit difficult to reconstruct and also in the current configuration, the position changes are abrupt, therefore, multiple current injections per image frame are considered during which the target remains stationary. Two different experiments are considered in which UKF and EKF use the parameters shown in Table 5.3. In both experiments, 8 image frames are considered and each image frame comprises of 6 current patterns. The reconstruction results for both experiments are shown in Figures 5.18 and 5.20 after 6 current patterns and the RMSE comparisons are done in Figures 5.19 and 5.21. In both experiments, it can be seen that UKF is performing far better than EKF in terms of reconstructed boundary. In the RMSE comparisons, it can be seen that mostly the RMSE for UKF is much less than EKF, however, there are certain points where the RMSE curve of both the filters almost come closer. The reason behind this phenomenon is the repetition of the current patterns. Since from the simulations, it was observed that UKF estimates the position very fast as compared to EKF, therefore, in the first few current patterns in the static case, the decrease in UKF is substantial as compared to EKF. However, after sometimes, when it finally reaches the estimated position, it generally wobbles on the same spot. In the meanwhile, the EKF also converges and hence the difference between UKF and EKF is reduced. In all the simulations and experimental results, it can be noticed that RMSE for UKF is always lower than EKF. This is because UKF basically uses nonlinear unscented transform, and EKF uses the linearized version of the measurement equation. However, there can also be some exception to this rule, i.e., certain scenarios might favor EKF better than UKF which can be best explained from Figure 5.22 in which there are three positions of the target. Since UKF estimates fast so it moves very fast to the second position and the slow EKF is still in the middle. However, from the second position to the third position there is more distance for UKF to cover as compared to EKF, thus proving that in certain cases one can also observe EKF's RMSE to be slightly less than that of UKF. The same phenomenon can also be observed in a situation in which a target at position A goes to position B and then comes back to position A. However, through extensive simulations and experimental results, it was found out that such cases are rare and UKF on the average performs better.

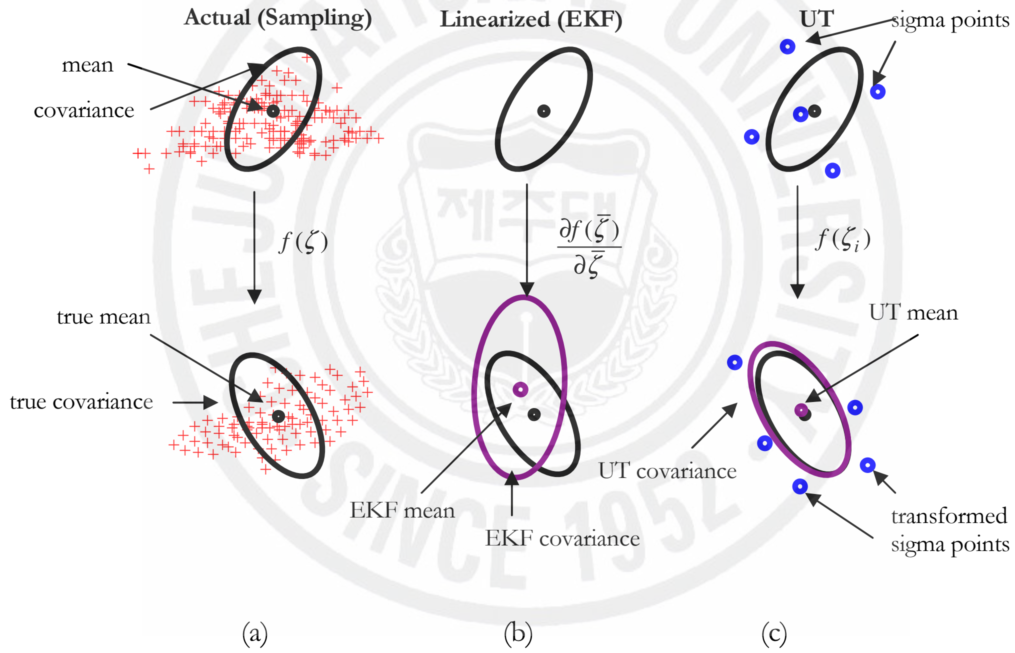

Figure 5.1. An example of unscented transform for mean and covariance propagation: (a) actual; (b) first-order linearization (EKF); and (c) unscented transform.

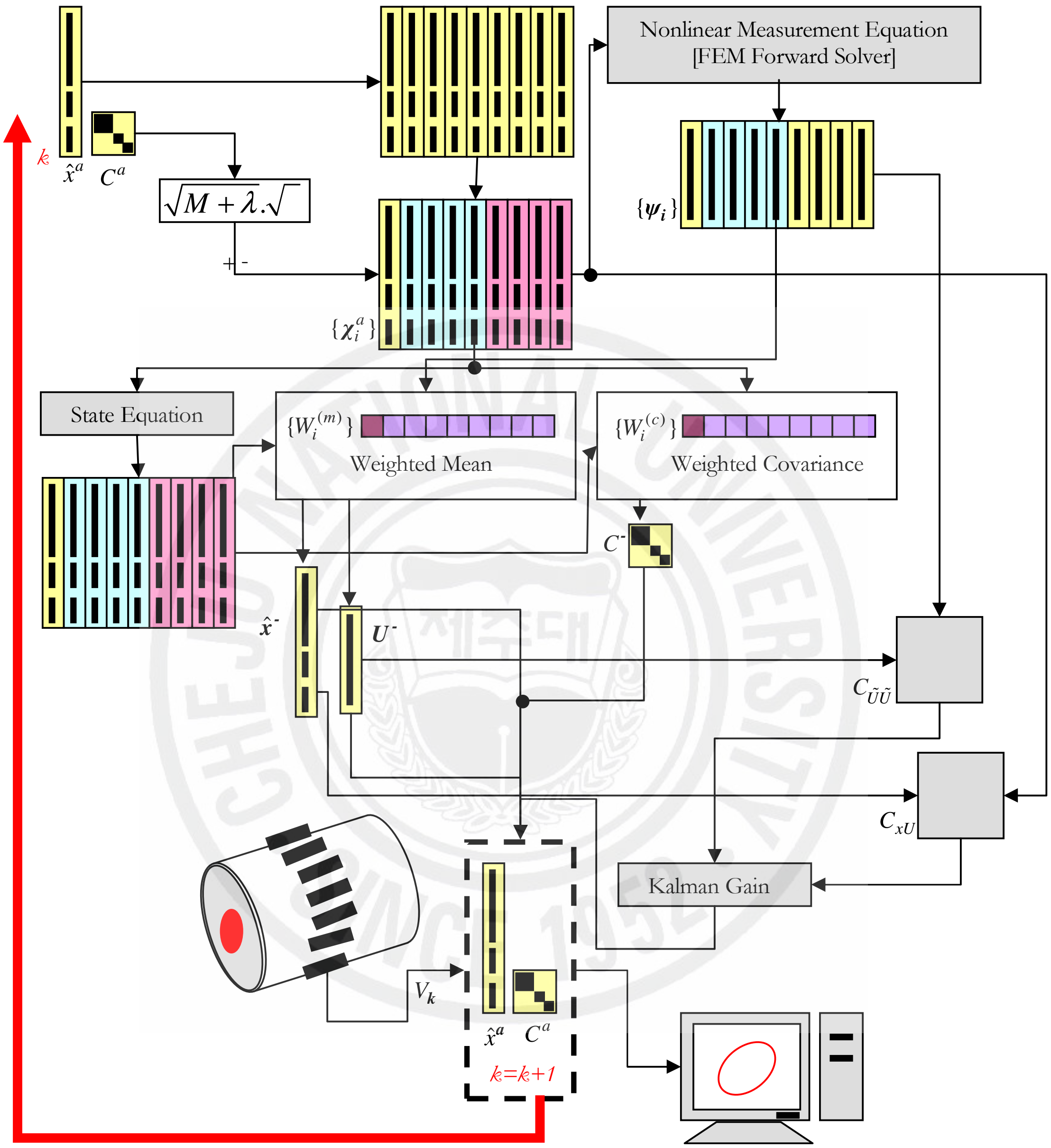

Figure 5.2. Block diagram of the UKF for phase boundary estimation in EIT.

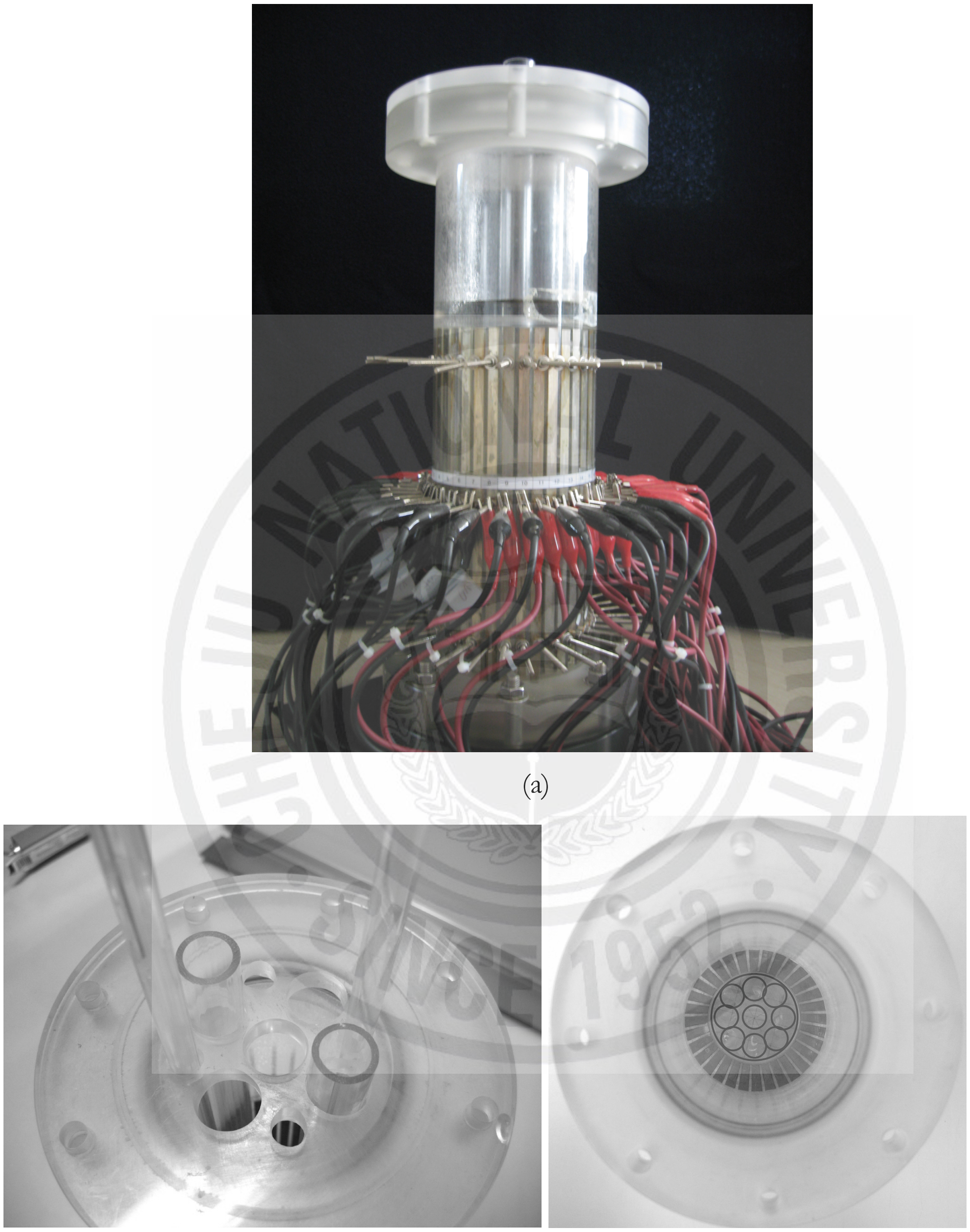

(a)

(b)

(c)

Figure 5.3. Experimental setup: (a) phantom; (b) plastic rods used as targets; and (c) positions where the plastic targets could be placed.

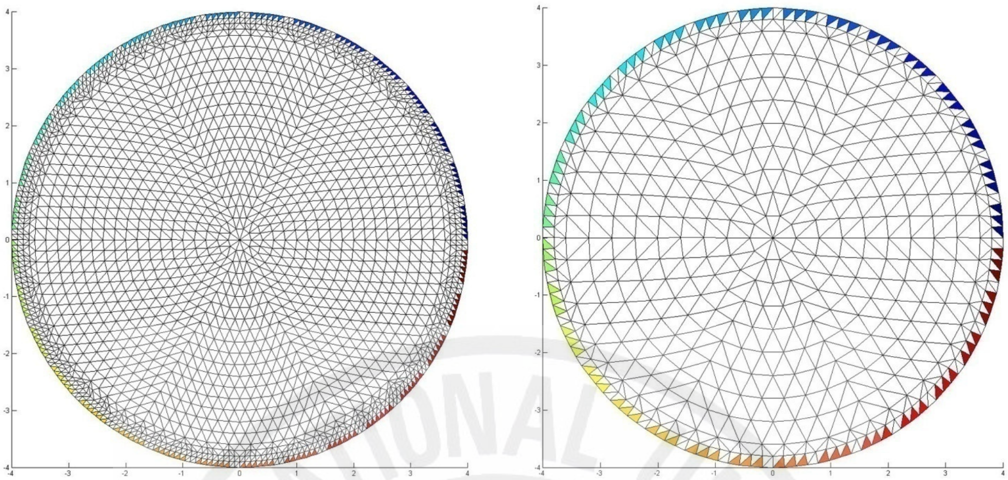

(a) (b)

Figure 5.4. Meshes used in: (a) forward solver; and (b) inverse solver.

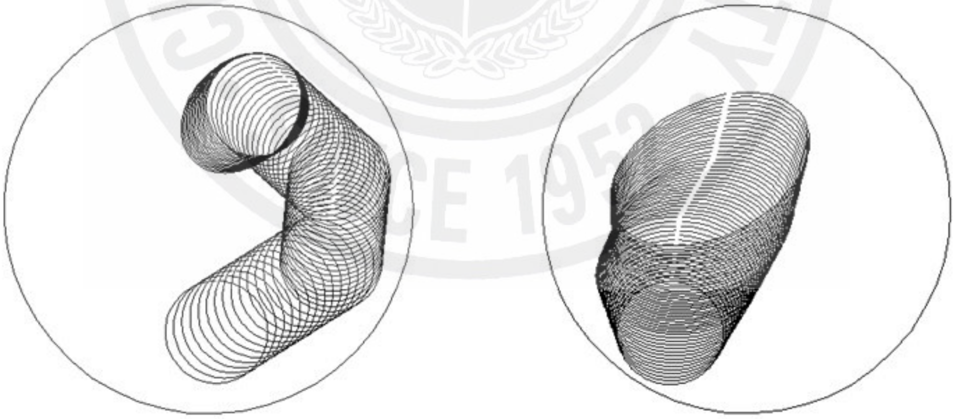

(a) (b)

Figure 5.5. Evolution model for numerical simulations: (a) scenario 1; and (b) scenario 2.

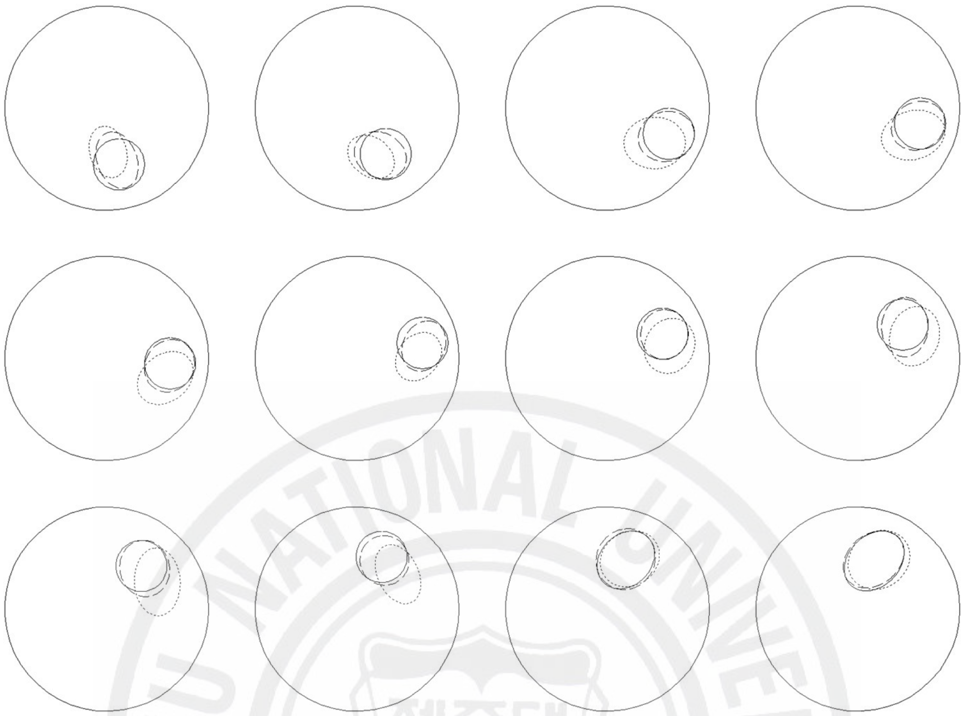

Figure 5.6. Reconstructed boundaries for scenario 1 with 1% noise. Solid line, dotted line and dashed line represent the true boundary, boundary estimated by EKF, and boundary estimated by UKF, respectively.

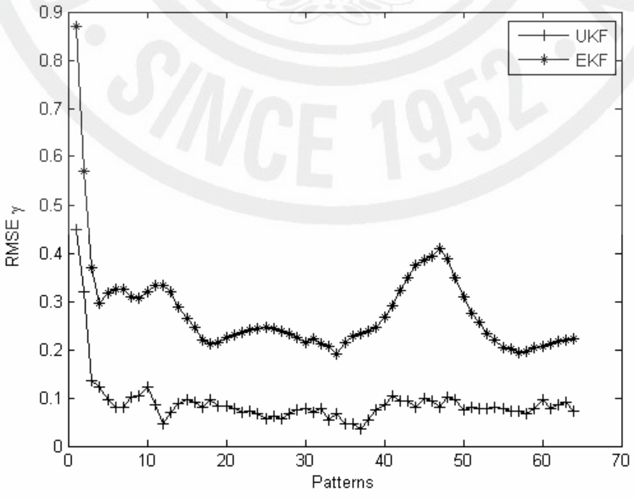

Figure 5.7. RMSE comparison for scenario 1 with measurements perturbed by 1% white Gaussian noise.

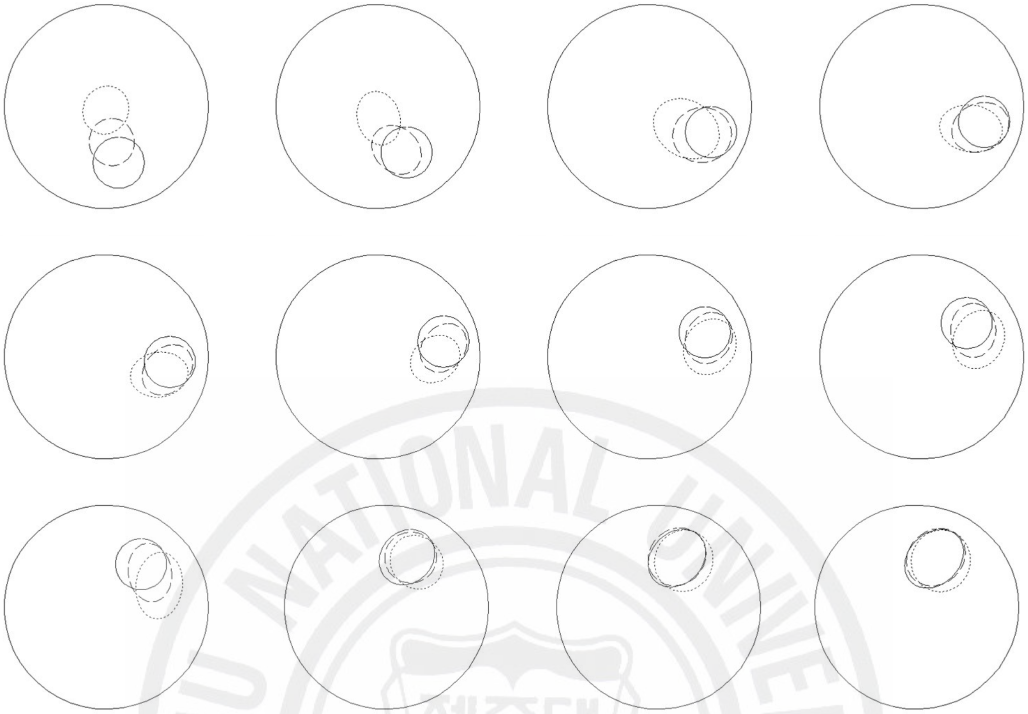

Figure 5.8. Reconstructed boundaries for scenario 1 with 2% noise. Solid line, dotted line and dashed line represent the true boundary, boundary estimated by EKF, and boundary estimated by UKF, respectively.

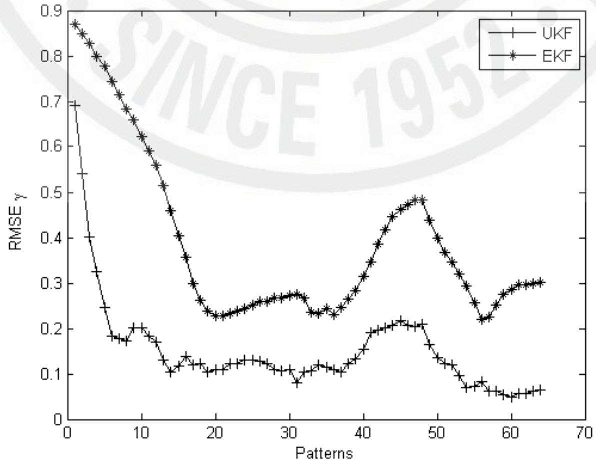

Figure 5.9. RMSE comparison for scenario 1 with 2% noise.

Figure 5.10. Reconstructed boundaries for scenario 1 with 3% noise. Solid line, dotted line and dashed line represent the true boundary, boundary estimated by EKF, and boundary estimated by UKF, respectively.

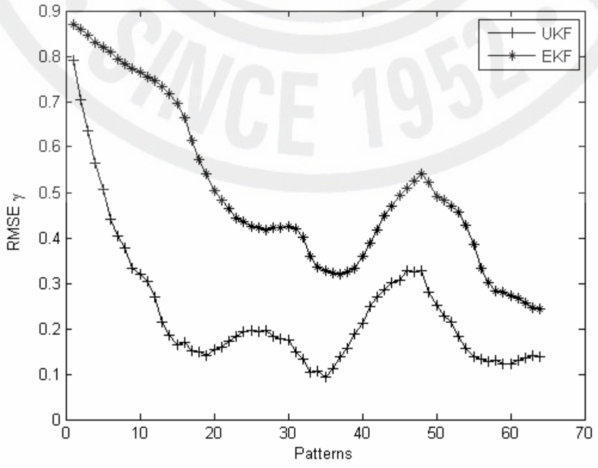

Figure 5.11. RMSE comparison for scenario 1 with 3% noise.

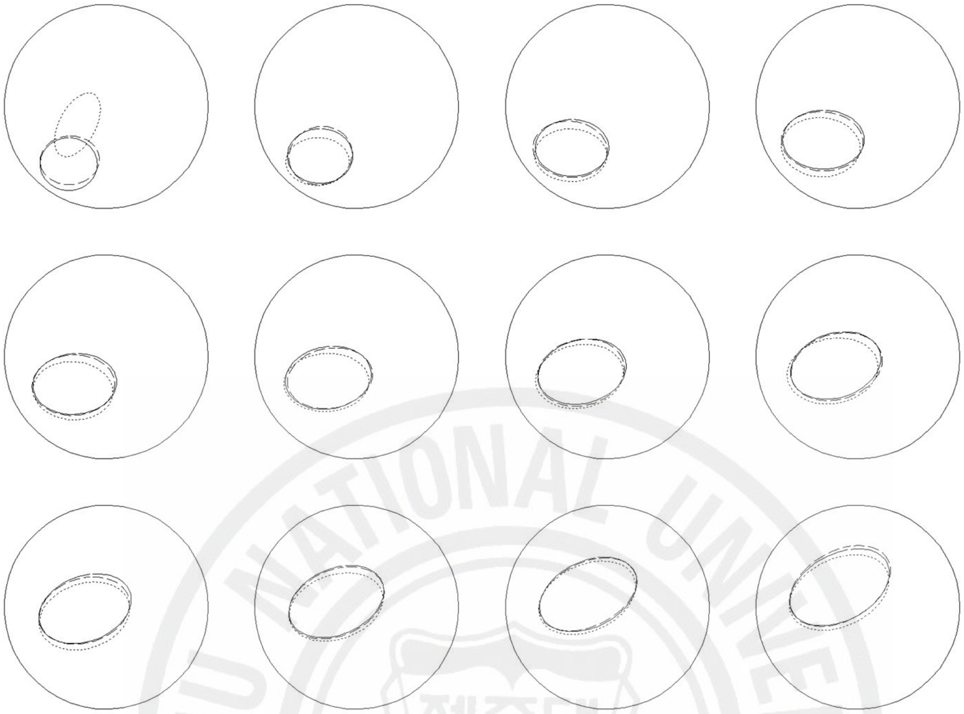

Figure 5.12. Reconstructed boundaries for scenario 2 with 1% noise. Solid line, dotted line and dashed line represent the true boundary, boundary estimated by EKF, and boundary estimated by UKF, respectively.

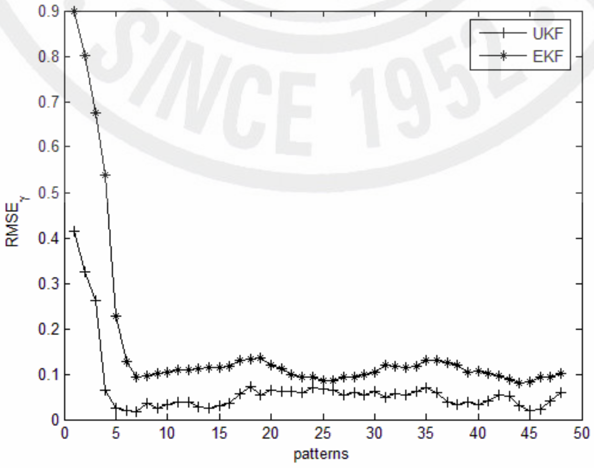

Figure 5.13. RMSE comparison for scenario 2 with 1% noise.

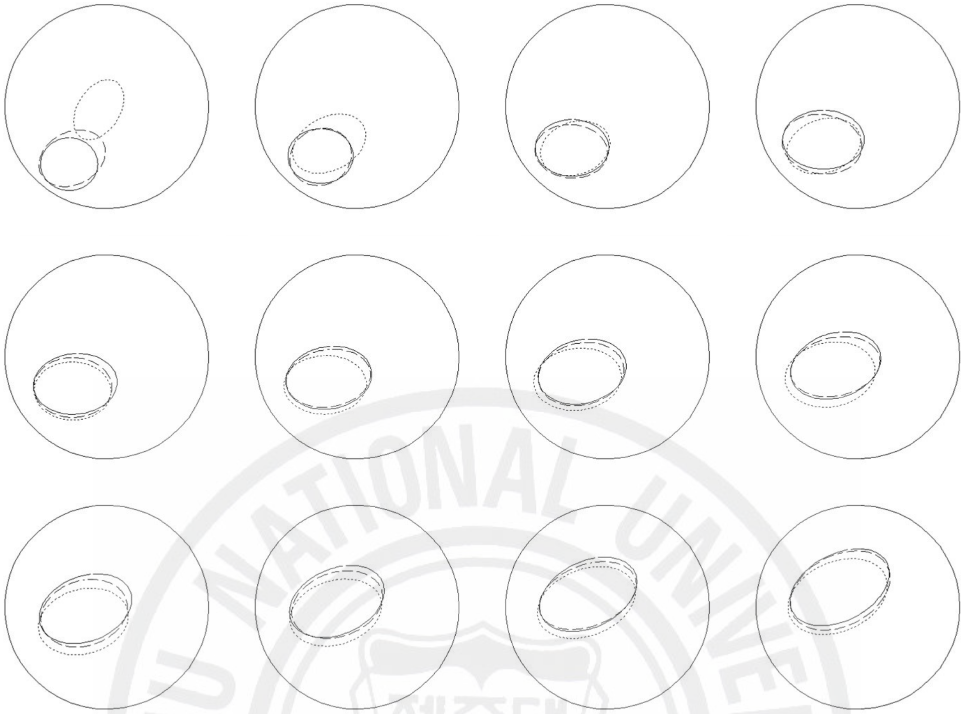

Figure 5.14. Reconstructed boundaries for scenario 2 with 2% noise. Solid line, dotted line and dashed line represent the true boundary, boundary estimated by EKF, and boundary estimated by UKF, respectively.

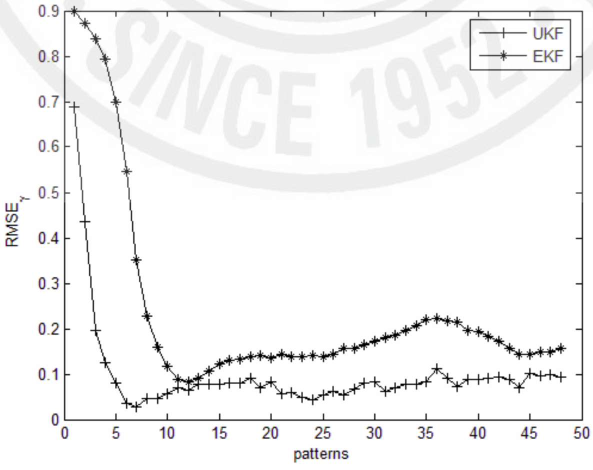

Figure 5.15. RMSE comparison for scenario 2 with 2% noise.

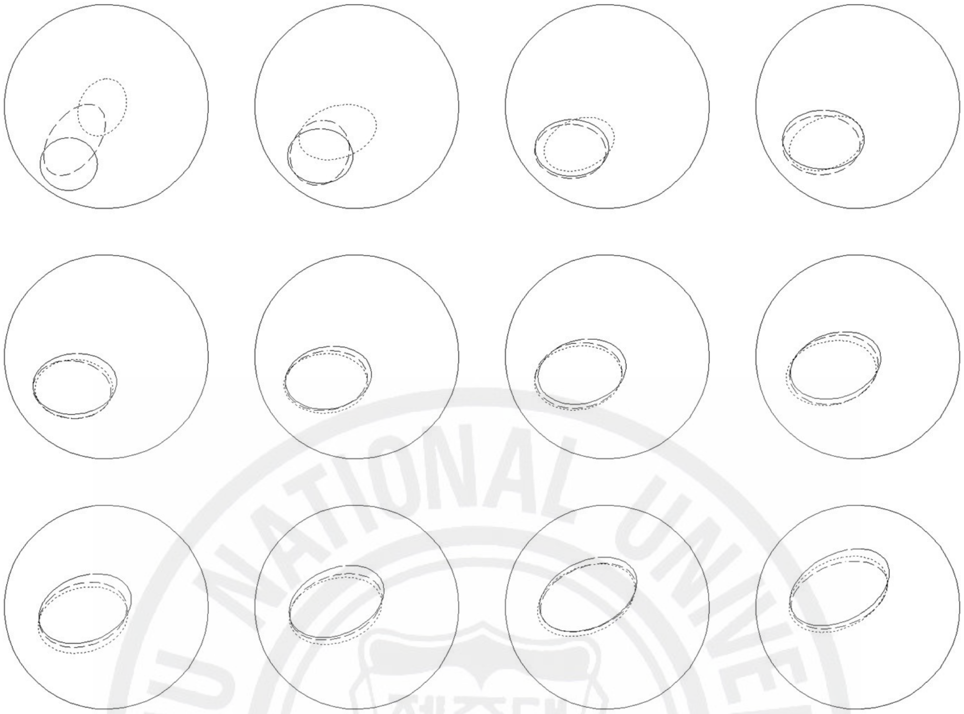

Figure 5.16. Reconstructed boundaries for scenario 2 with 3% noise. Solid line, dotted line and dashed line represent the true boundary, boundary estimated by EKF, and boundary estimated by UKF, respectively.

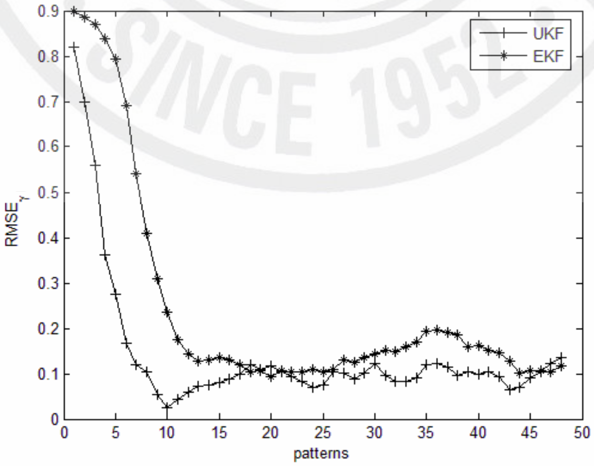

Figure 5.17. RMSE comparison for scenario 2 with 3% noise.

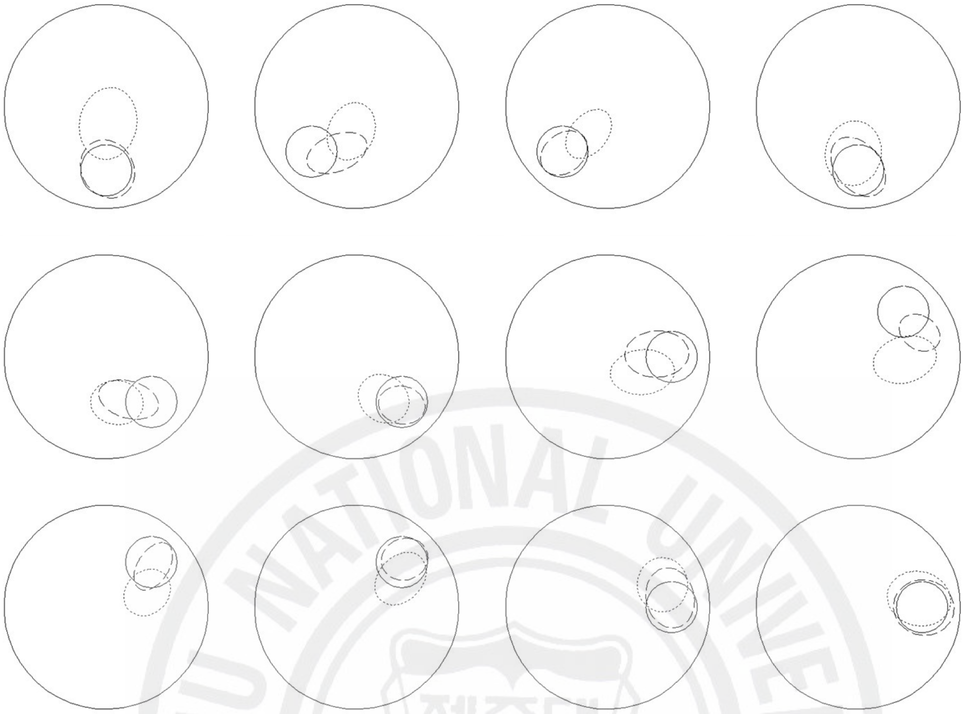

Figure 5.18. Reconstructed boundaries for first experiment. Solid line, dotted line and dashed line represent the true boundary, boundary estimated by EKF, and boundary estimated by UKF, respectively.

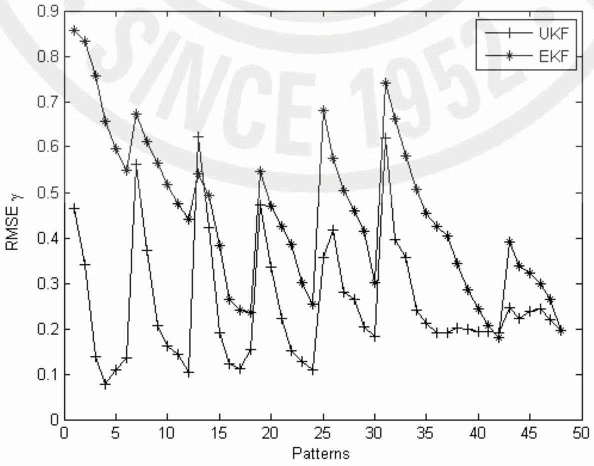

Figure 5.19. RMSE comparison for first experiment.

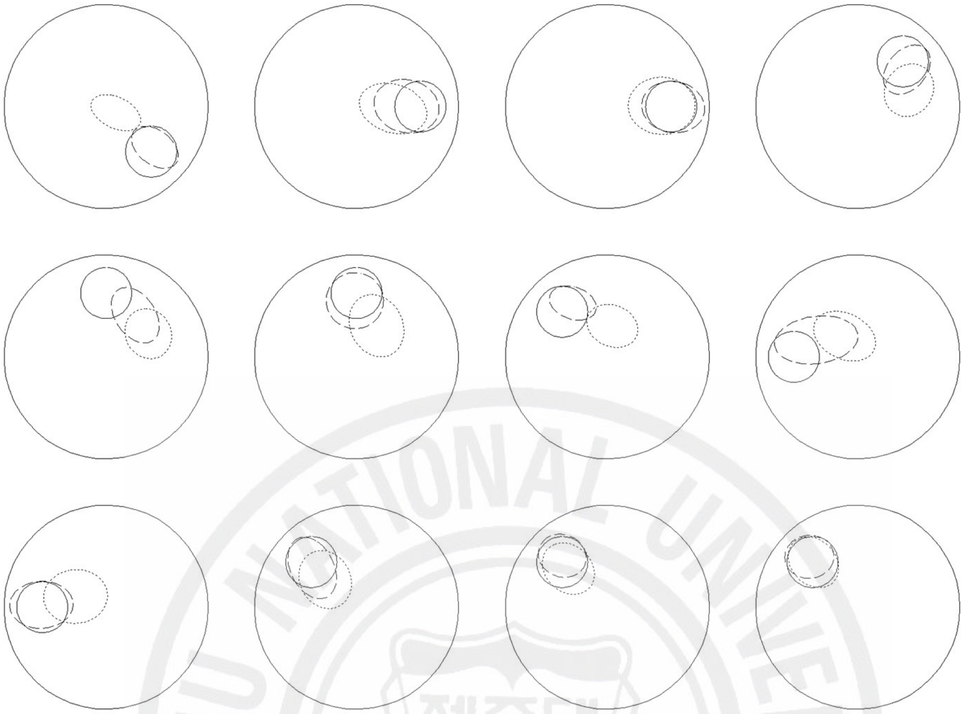

Figure 5.20. Reconstructed boundaries for the second experiment. Solid line, dotted line and dashed line represent the true boundary, boundary estimated by EKF, and boundary estimated by UKF, respectively.

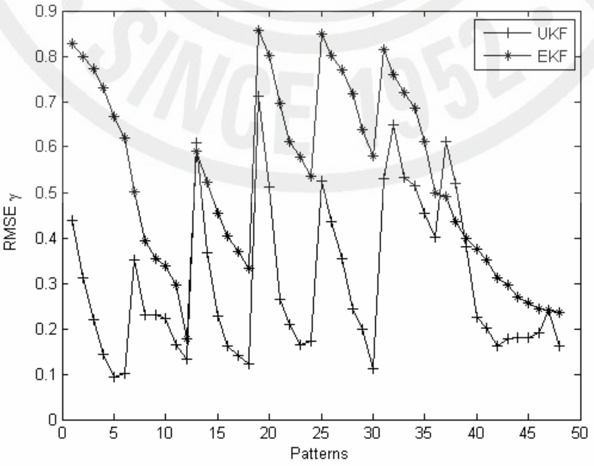

Figure 5.21. .RMSE comparison for the second experiment.

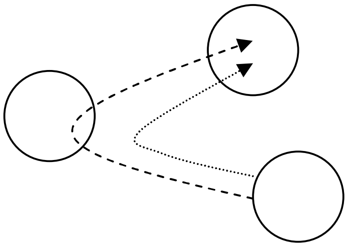

Figure 5.22. A scenario favoring EKF. UKF path is represented by dashed line and EKF path is represented by dotted line.

Table 5.1. Parameters used in simulations for scenario 1.

Parameters	EKF			UKF		
	1% white Gaussian Noise	2% white Gaussian Noise	3% white Gaussian Noise	1% white Gaussian Noise	2% white Gaussian Noise	3% white Gaussian Noise
Q_k	$0.01\,I_N$	$0.01\,I_N$	$0.01\,I_N$	$0.01\,I_N$	$0.01\,I_N$	$0.01\,I_N$
R_k	$200\,I_E$	$900\,I_E$	$3000\,I_E$	$10\,I_E$	$90\,I_E$	$300\,I_E$
C_0	$0.1\,I_N$	$0.1\,I_N$	$0.1\,I_N$	$0.1\,I_N$	$0.1\,I_N$	$0.1\,I_N$
α_R	0.001	0.01	0.1	-	-	-
α_s	-	-	-	0.1	0.08	0.2
β_s	-	-	-	2	2	2
κ_s	-	-	-	0	0	0

Table 5.2. Parameters used in simulations for scenario 2.

Parameters	EKF			UKF		
	1% white Gaussian Noise	2% white Gaussian Noise	3% white Gaussian Noise	1% white Gaussian Noise	2% white Gaussian Noise	3% white Gaussian Noise
Q_k	$0.01\,I_N$	$0.01\,I_N$	$0.01\,I_N$	$0.01\,I_N$	$0.01\,I_N$	$0.01\,I_N$
R_k	$200\,I_E$	$1000\,I_E$	$6000\,I_E$	$10\,I_E$	$90\,I_E$	$300\,I_E$
C_0	$0.1\,I_N$	$0.1\,I_N$	$0.1\,I_N$	$0.1\,I_N$	$0.1\,I_N$	$0.1\,I_N$
α_R	0.001	0.01	0.1	-	-	-
α_s	-	-	-	0.05	0.08	0.2
β_s	-	-	-	2	2	2
κ_s	-	-	-	0	0	0

Table 5.3. Parameter used in obtaining experimental results.

Parameters	EKF	UKF
Q_k	$0.01\, I_N$	$0.01\, I_N$
R_k	$200\, I_E$	$10\, I_E$
C_0	$0.1\, I_N$	$0.1\, I_N$
α_R	0.2	-
α_s	-	0.2
β_s	-	2
κ_s	-	0

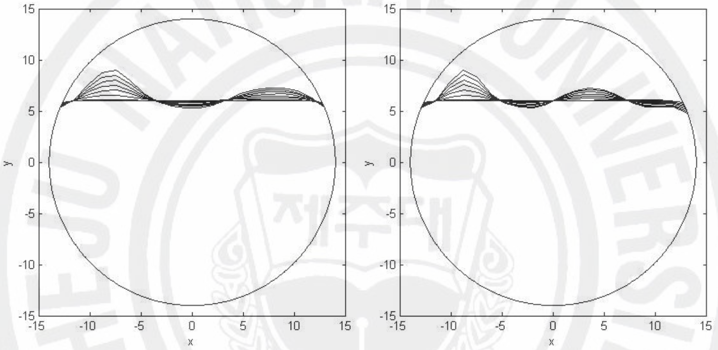

(a) scenario 1 (b) scenario 2

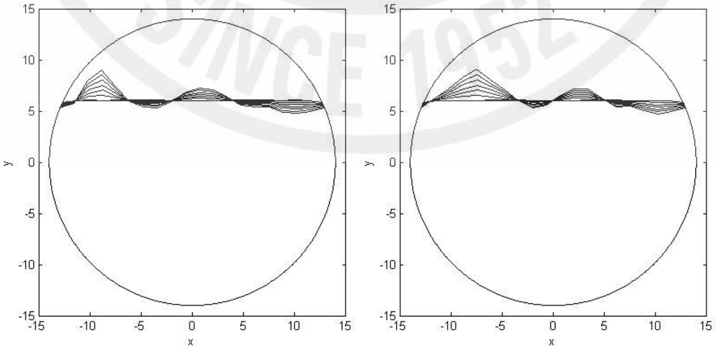

(c) scenario 3 (d) scenario 4

Figure 5.23. Scenario considered: (a) for reconstruction with 10 front points; (b) for reconstruction with 12 front points; (c) for reconstruction with 14 front points; and (d) for reconstruction with 16 front points

5.3 Numerical results for front points

In this section, the numerical results for UKF are reported with the same settings as considered in the first chapter for EKF i.e., stratified flow of two conducting immiscible liquids through a cylindrical pipe of diameter $28cm$ with 16 electrodes of width $2.5cm$ each around its periphery. For comparison purposes, EKF is used along with Tikhonov regularization with regularization parameter as α_R and regularization matrix as identity matrix. Starting with 10 front points, the UKF simulations are performed using contrast ratio of 100:1 and are tested with 1%, 2% and 3% white Gaussian noise. Furthermore, higher contrast ratios are tested with 10 front points and results for contrast ratio as high as 10000:1 is reported with 1% white Gaussian noise. The scenario considered for 10 front points is shown in Figure 5.23(a). Also, the results are provided for the increase in the number of front points. The scenarios for 12 front points, 14 front points and 16 front points are shown in Figures 5.23(b), 5.23(c), and 5.23(d), respectively. It was found that the front points greater than 16 tend to deteriorate the image reconstruction performance incase of UKF whereas it was 10 front points in case of EKF in Kim *et al.* (2007). In all the simulations, a very small measurement data is used, i.e., 8 image frames. Therefore, total number of current patterns are 32. Furthermore, in the reconstruction process, only first two modes of cosine and sine patterns are used as: $\cos(\zeta_l)$, $\cos(2\zeta_l)$, $\sin(\zeta_l)$ and $\sin(2\zeta_l)$. The repeated use of the first cosine pattern is dropped in this study.

Figures 5.24-5.26 show the reconstructed interfacial boundaries for scenario 1 in which white Gaussian noises of 1%, 2%, and 3% are added to the simulated voltage measurement so as to emulate the real situations. The parameters used in EKF and UKF are shown in Table 5.4. In Figures 5.24-5.26, the reconstructed boundaries are shown after every 4 current patterns. As seen from the results, UKF performs significantly better than EKF. For 1% white Gaussian noise case (Figure 5.24), on the average a performance gain of 2 is observed in UKF over EKF in terms of RMSE. The average value of RMSE for UKF are around 0.05 and for EKF they are around 0.1. Similarly, a performance gain of 1.25 (0.08 for UKF and 0.1 for EKF on the average) can be observed for 2% white Gaussian noise (Figure 5.25). For 3% white Gaussian noise (Figure 5.26), EKF has completely failed in estimating the interfacial boundaries. The observed average RMSE values are 0.09 and 0.11 for UKF and EKF, respectively. Several other conclusions can also be drawn from analyzing the same results. UKF has a small transition period, therefore, the initial guess moves very fast to the true boundary. EKF on the other hand has a slow convergence. For relative smooth boundaries, UKF and EKF will have similar performance, but UKF will still be slightly better. With many ripples in the boundaries, the performance of UKF will be significantly better than EKF in crests and troughs on the interface where the differences in adjacent front points is high. That is exactly the same reason why 280 frames were used and a slow moving interface was considered for 10 front points in Kim *et al.* (2007).

Table 5.4. Parameters used in simulations for assessing the impact of measurement noise in 10 front points case with contrast ratio of 100:1.

	EKF			UKF		
Parameters	1% white Gaussian Noise	2% white Gaussian Noise	3% white Gaussian Noise	1% white Gaussian Noise	2% white Gaussian Noise	3% white Gaussian Noise
Q_k	$0.01\,I_N$	$0.01\,I_N$	$0.01\,I_N$	$0.01\,I_N$	$0.002\,I_N$	$0.01\,I_N$
R_k	$9\times10^4\,I_E$	$10\times10^4\,I_E$	$13\times10^4\,I_E$	$2\times10^3\,I_E$	$3\times10^3\,I_E$	$3\times10^4\,I_E$
C_0	$0.01\,I_N$	$0.1\,I_N$	$0.01\,I_N$	$0.01\,I_N$	$0.01\,I_N$	$0.01\,I_N$
α_R	0.00001	0.0001	0.0001	-	-	-
α_s	-	-	-	0.5	1	0.2
β_s	-	-	-	2	2	2
κ_s	-	-	-	0	0	0

Table 5.5. Parameters used in simulations for assessing the impact of contrast ratio in 10 front points case with 1% noise.

	Contrast Ratio			
	EKF		UKF	
Parameters	1000:1	10000:1	1000:1	10000:1
Q_k	$0.01\,I_N$	$0.01\,I_N$	$0.01\,I_N$	$0.01\,I_N$
R_k	$5\times10^6\,I_E$	$5\times10^7\,I_E$	$3\times10^4\,I_E$	$5\times10^6\,I_E$
C_0	$0.01\,I_N$	$0.1\,I_N$	$0.01\,I_N$	$0.01\,I_N$
α_R	0.0001	0.0001	-	-
α_s	-	-	1	1
β_s	-	-	2	2
κ_s	-	-	0	0

It is worth mentioning here that the measurement error covariance matrix *R* of EKF will always be bigger than UKF as for EKF it will also include the linearization errors caused by ignoring higher-order terms in Taylor series expansion. Therefore, this point should be kept in mind in replacing EKF with UKF as an inverse solver. With 10 front points and 1% white Gaussian noise, the results with different contrast ratios are shown in Figures 5.27 and 5.28 in which the reconstructed boundaries are shown after every 4 current patterns. The parameters used in the simulation are listed in Table 5.5. Notice that UKF is error-prone to increase in contrast ratio. In the contrast ratios of 100:1, 1000:1, and 10000:1, it can be observed that on the average, the RMSE of UKF is somewhere between 0.05 and 0.09 and a very little increase in RMSE can be observed with the increase of contrast ratio. On the other hand, the recontruction results for EKF show a different story. There is an exponential increase in RMSE with the increase in contrast ratio and also it can be observed in Figure 5.28 that EKF becomes unstable and fails in the contrast ratio of 10000:1. As mentioned before, with the increase in the ripples in the interface, UKF will tend to show better performance than EKF, so for this purpose, increase in front points are considered for the scenarios shown in the Figures 5.23(b), 5.23(c), and 5.23(d), respectively. The reconstruction results are shown in Figures 5.29-5.31 whereas the parameters used in the simulations are listed in Table 5.6. Again the reconstructed boundaries are shown after every 4 current patterns. With the increase in the number of front points, there is a decrease in the performance for both UKF and EKF, however, the deterioration in estimation quality of UKF is small as compared to EKF.

Table 5.6. Parameters used in simulations for assessing the impact of front points with contrast ratio of 100:1.

Parameters	EKF			UKF		
	12 Front Points	14 Front Points	16 Front Points	12 Front Points	14 Front Points	16 Front Points
Q_k	$0.01\,I_N$	$0.1\,I_N$	$0.01\,I_N$	$0.01\,I_N$	$0.01\,I_N$	$0.01\,I_N$
R_k	$4\times10^5\,I_E$	$6\times10^6\,I_E$	$3\times10^6\,I_E$	$3\times10^4\,I_E$	$3\times10^5\,I_E$	$3\times10^5\,I_E$
C_0	$0.01\,I_N$	$0.1\,I_N$	$0.01\,I_N$	$0.01\,I_N$	$0.01\,I_N$	$0.01\,I_N$
α_R	0.0001	0.001	0.0001	-	-	-
α_s	-	-	-	1.5	1	1.5
β_s	-	-	-	2	2	2
κ_s	-	-	-	0	0	0

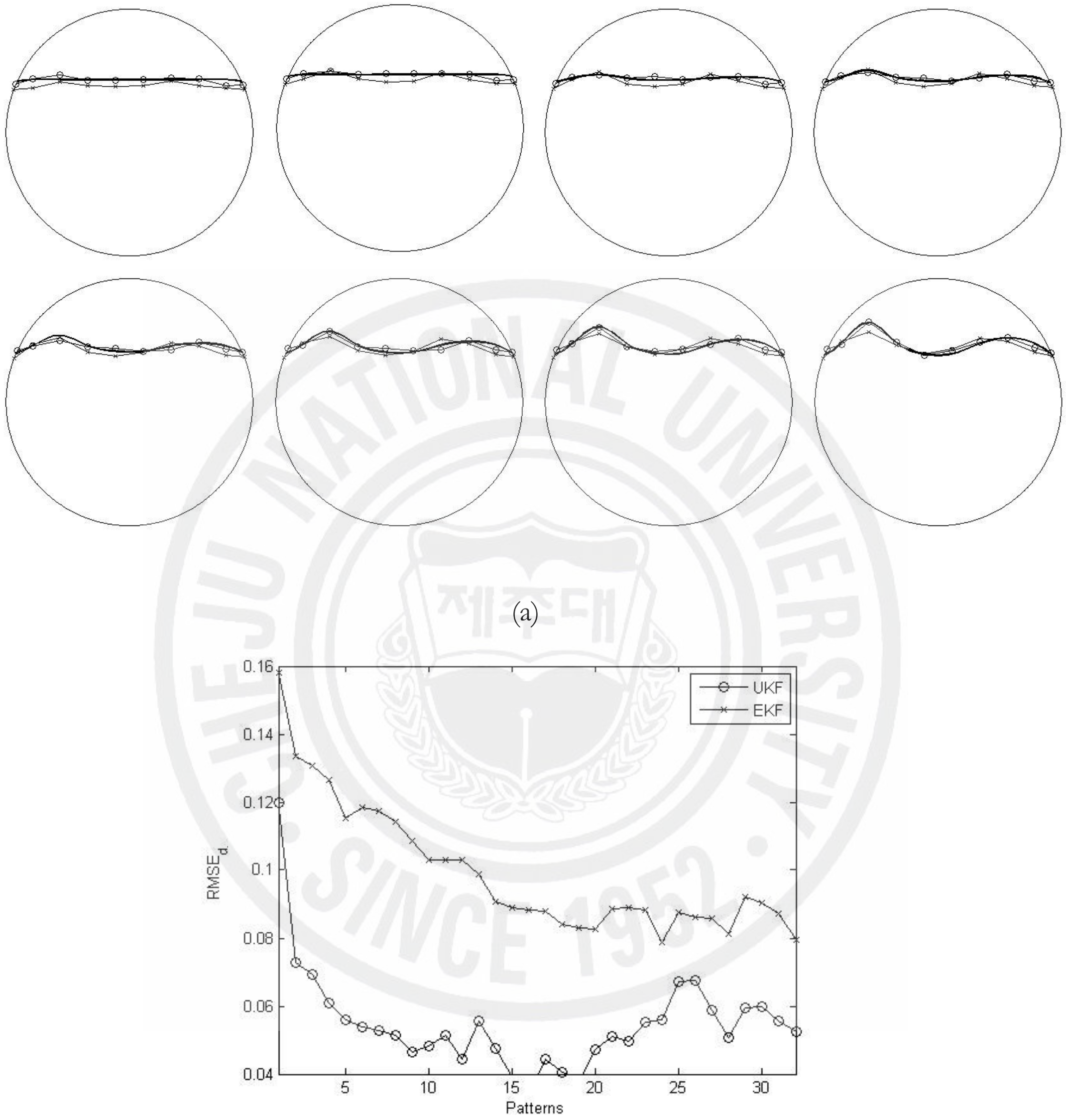

(a)

(b)

Figure 5.24. Results with 10 front points for scenario1 with 1% noise and contrast ratio of 100:1: (a) reconstructed boundaries after every 4 current patterns. True profile (-), EKF (-x-), and UKF (-o-); (b) RMSE comparison between EKF and UKF.

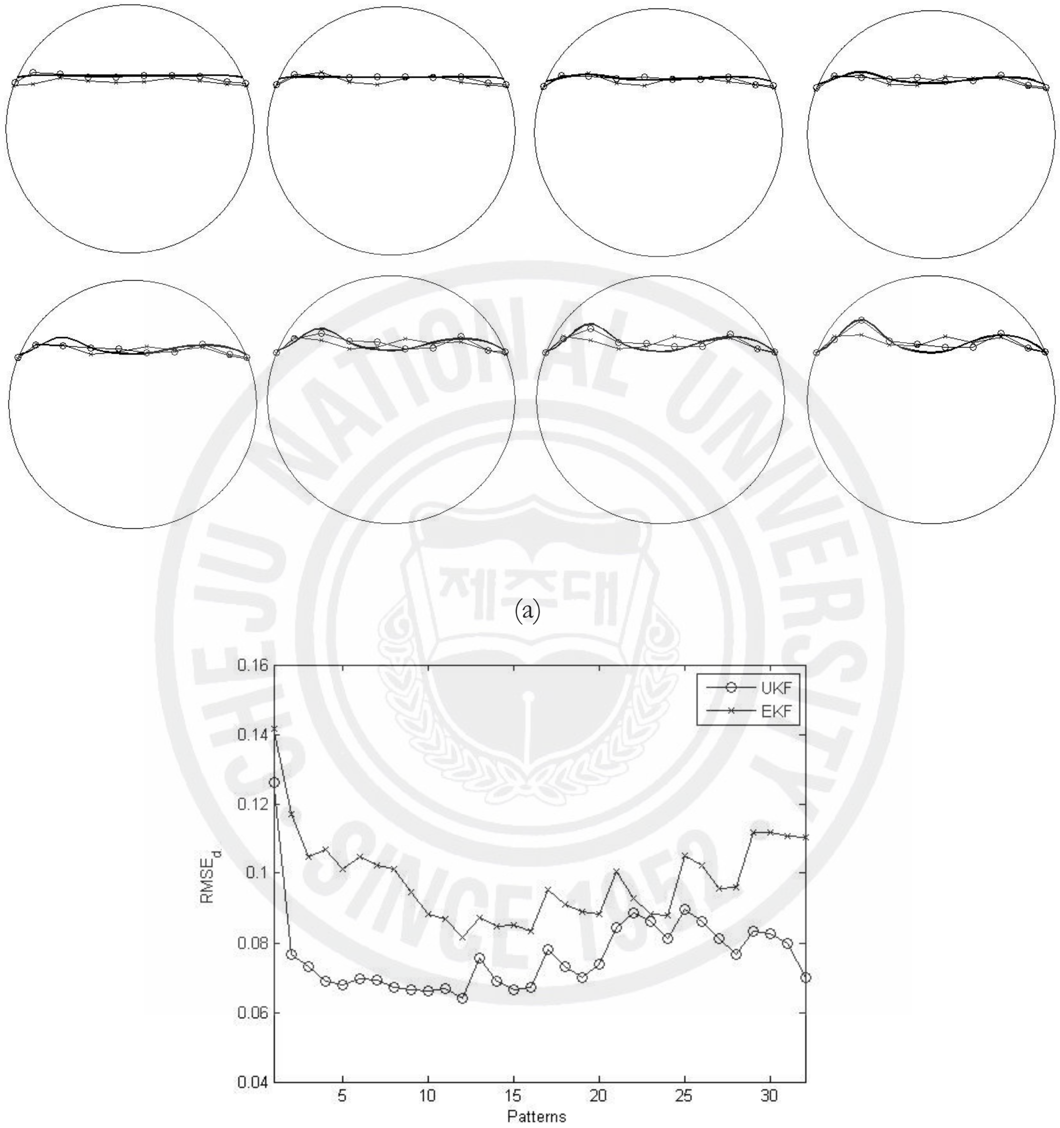

(b)

Figure 5.25. Results with 10 front points for scenario1 with 2% noise and contrast ratio of 100:1: (a) reconstructed boundaries after every 4 current patterns. True profile (-), EKF (-x-), and UKF (-o-); (b) RMSE comparison between EKF and UKF.

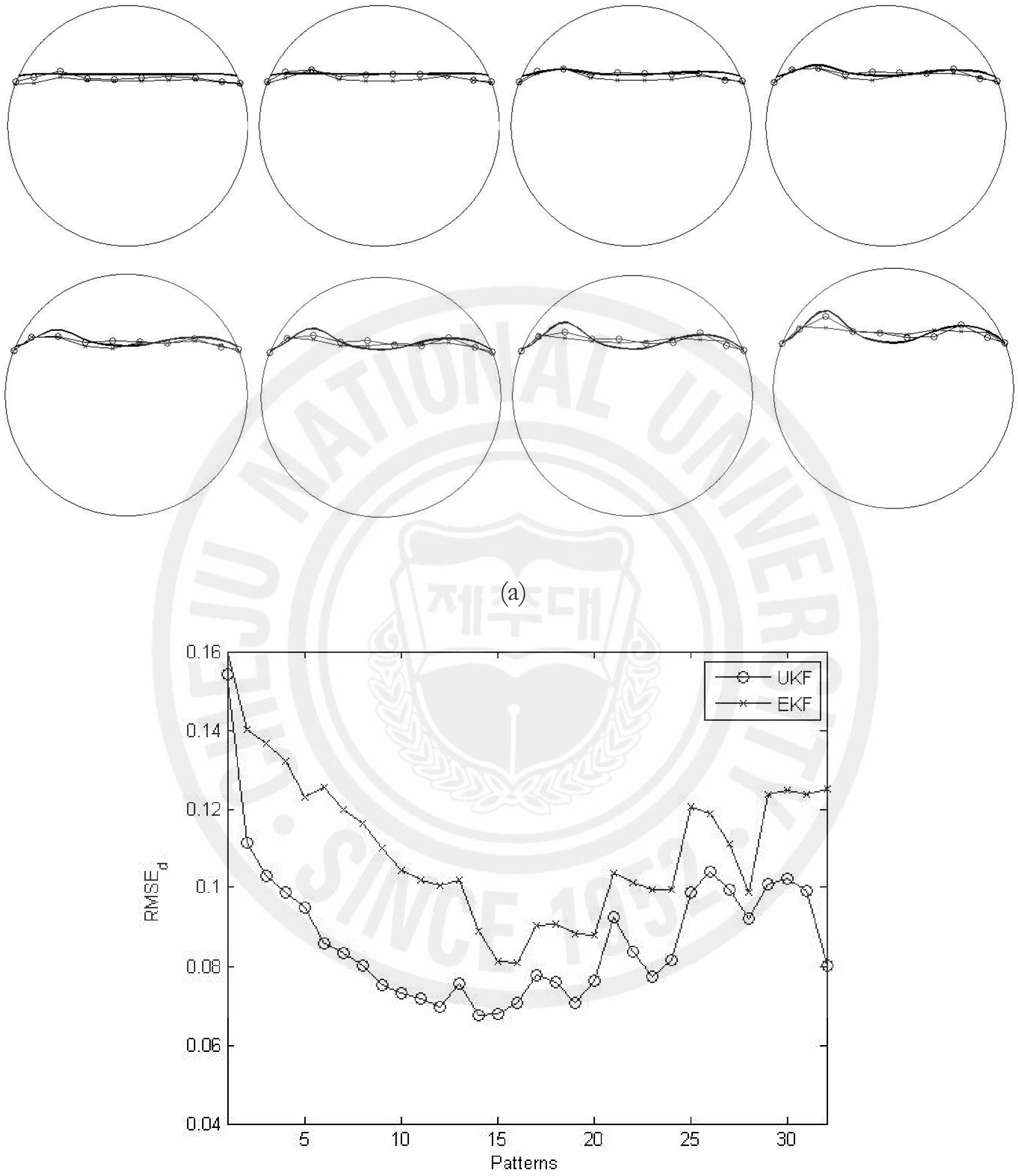

(a)

(b)

Figure 5.26. Results with 10 front points for scenario 1 with 3% noise and contrast ratio of 100:1: (a) reconstructed boundaries after every 4 current patterns. True profile (-), EKF (-x-), and UKF (-o-); (b) RMSE comparison between EKF and UKF.

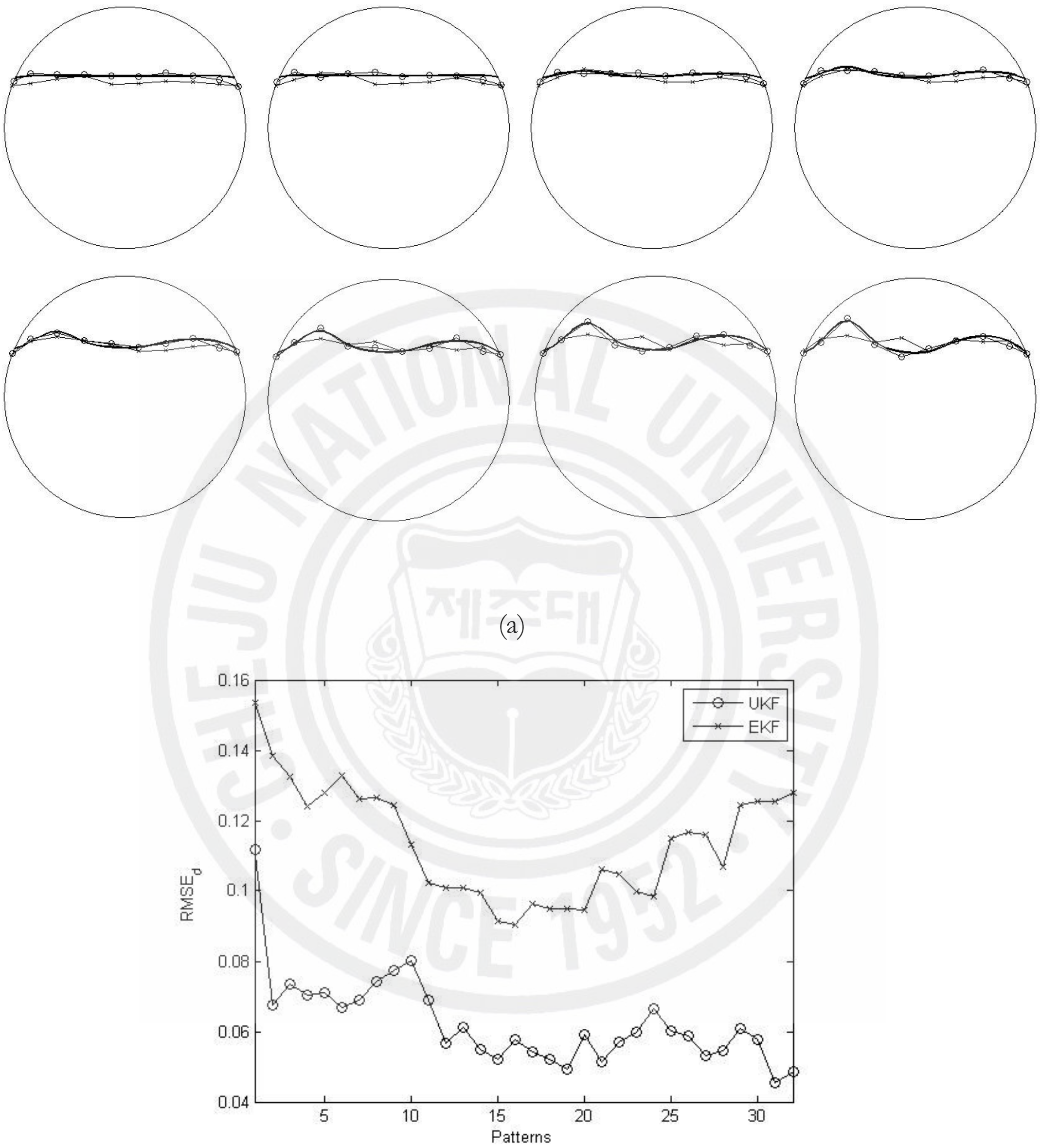

(b)

Figure 5.27. Results with 10 front points for scenario1 with 1% noise and contrast ratio of 1000:1: (a) reconstructed boundaries after every 4 current patterns. True profile (-), EKF (-x-), and UKF (-o-); (b) RMSE comparison between EKF and UKF.

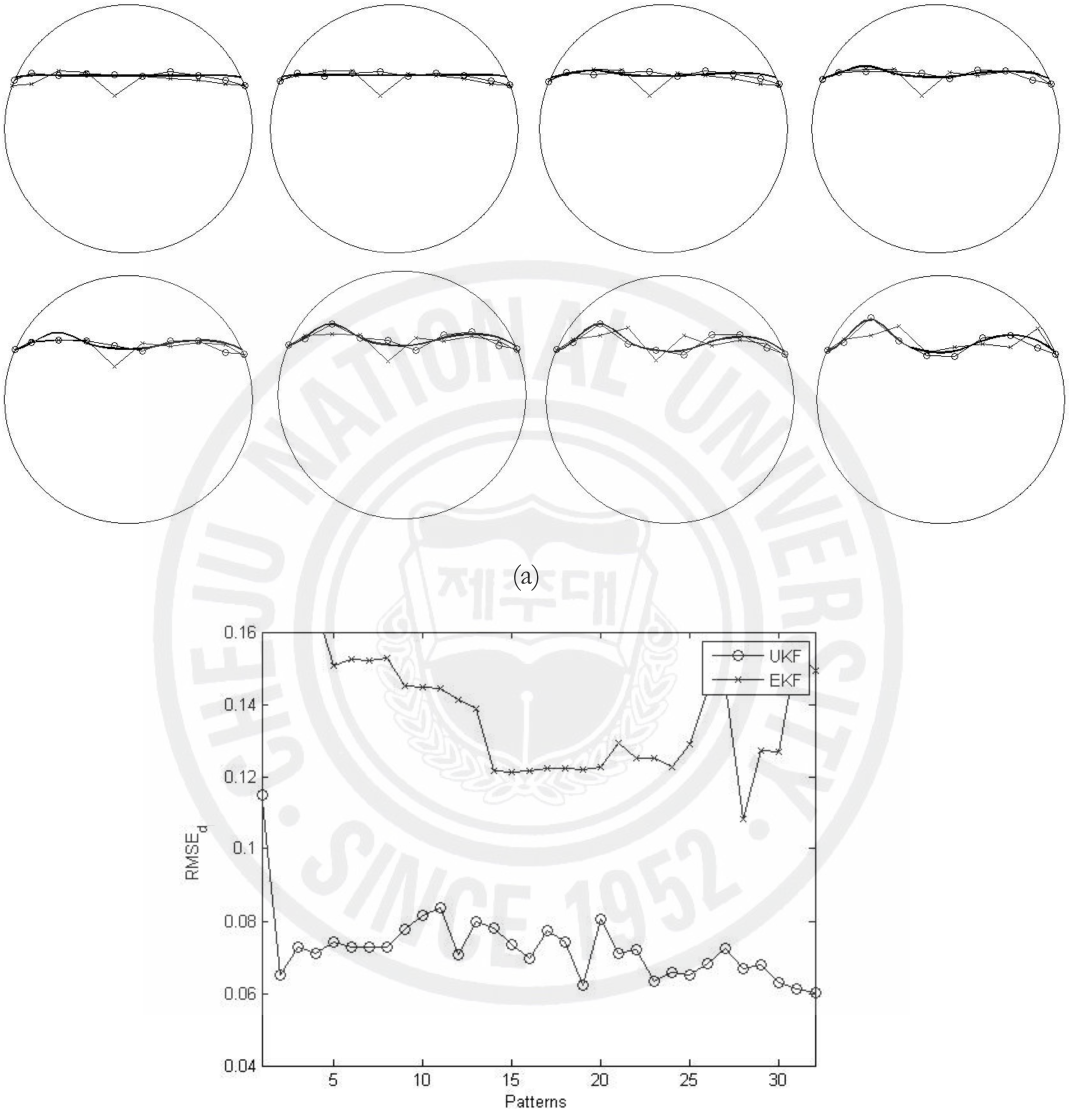

(a)

(b)

Figure 5.28. Results with 10 front points for scenario1 with 1% noise and contrast ratio of 10000:1: (a) reconstructed boundaries after every 4 current patterns. True profile (-), EKF (-x-), and UKF (-o-); (b) RMSE comparison between EKF and UKF.

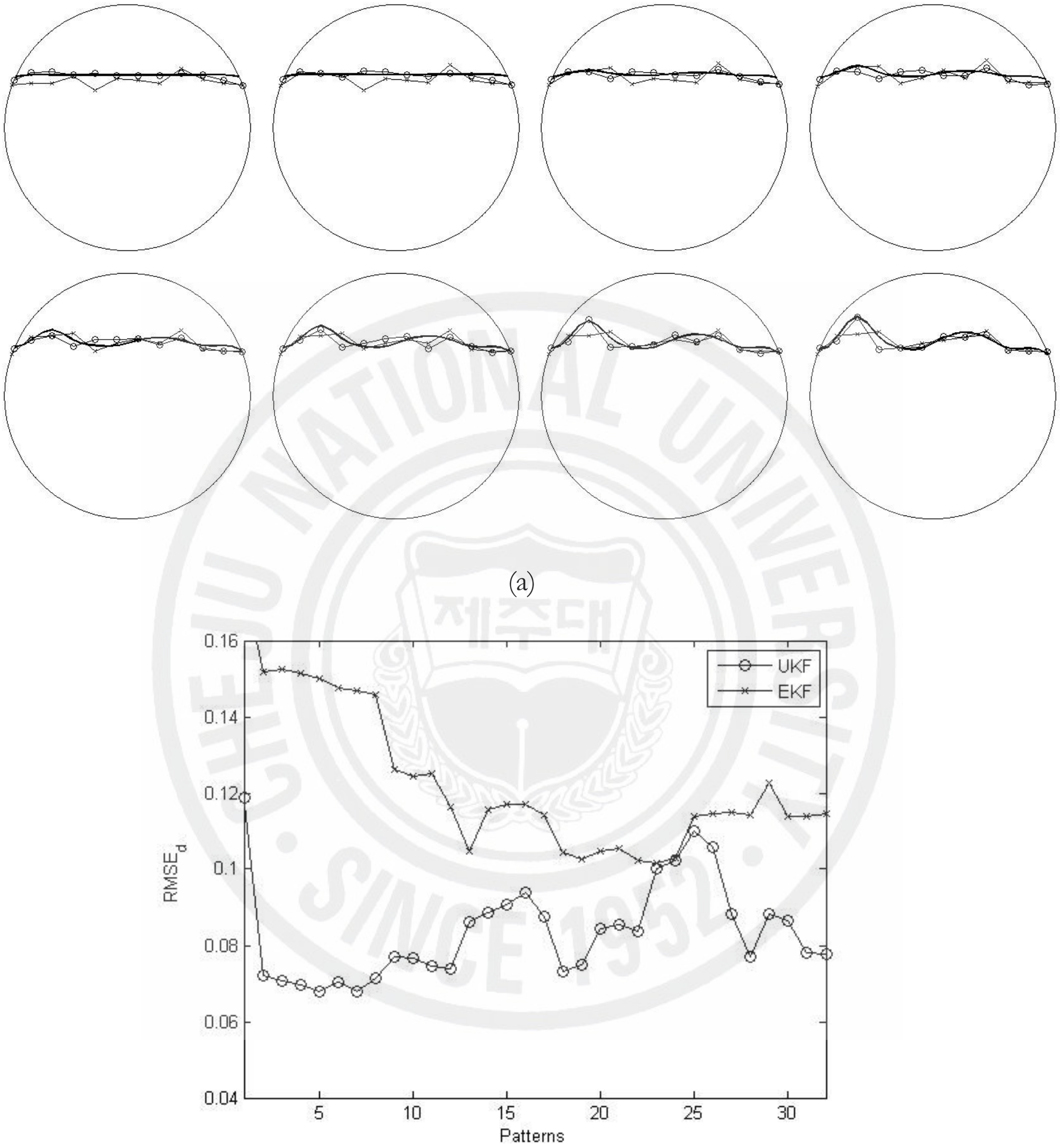
(a)

(b)

Figure 5.29. Results with 12 front points for scenario 2 with 1% noise and contrast ratio of 100:1: (a) reconstructed boundaries after every 4 current patterns. True profile (-), EKF (-x-), and UKF(-o-); (b) RMSE comparison between EKF and UKF.

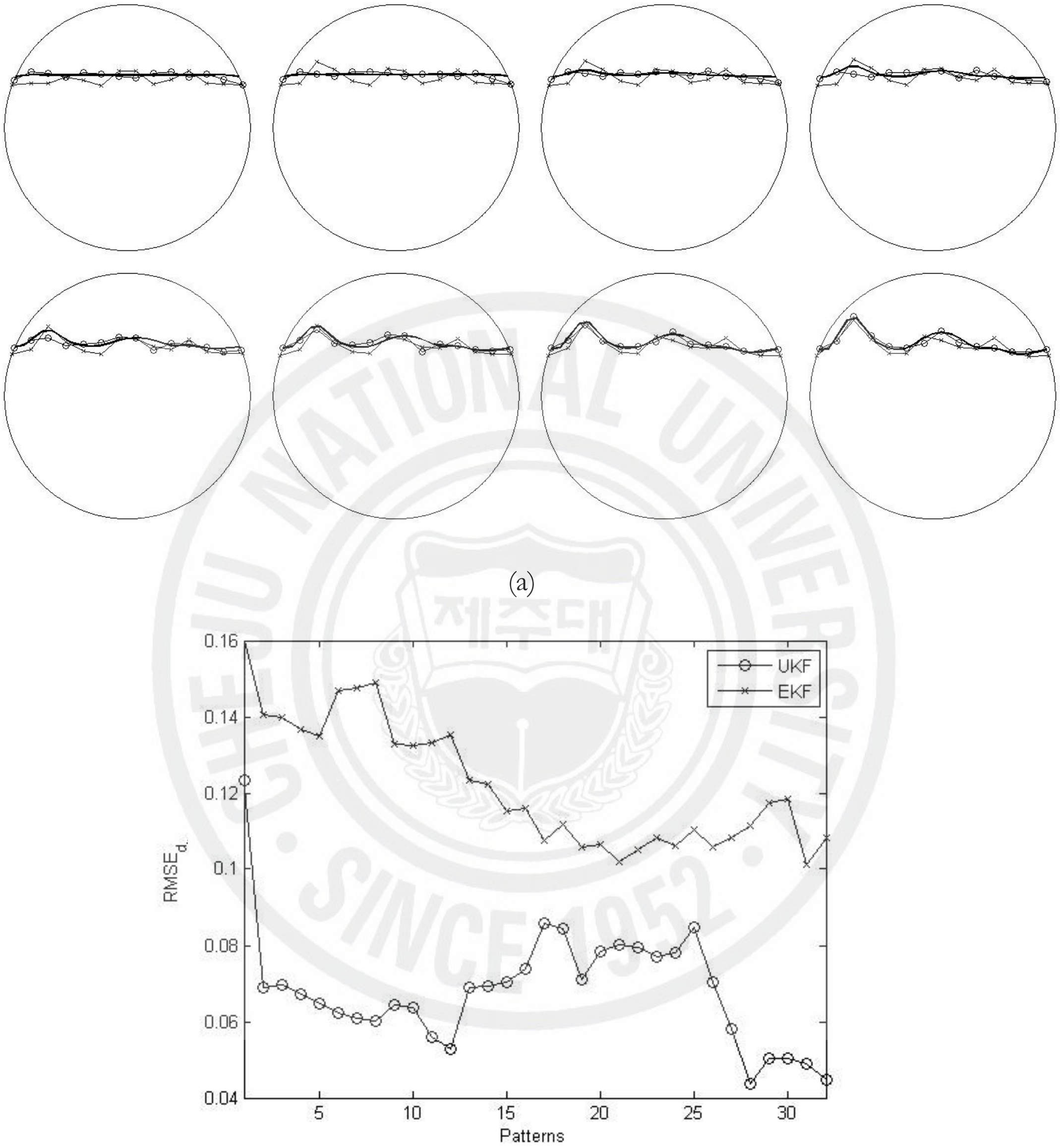

(a)

(b)

Figure 5.30. Results with 14 front points for scenario 3 with 1% noise and contrast ratio of 100:1: (a) reconstructed boundaries after every 4 current patterns. True profile (-), EKF (-x-), and UKF (-o-); (b) RMSE comparison between EKF and UKF.

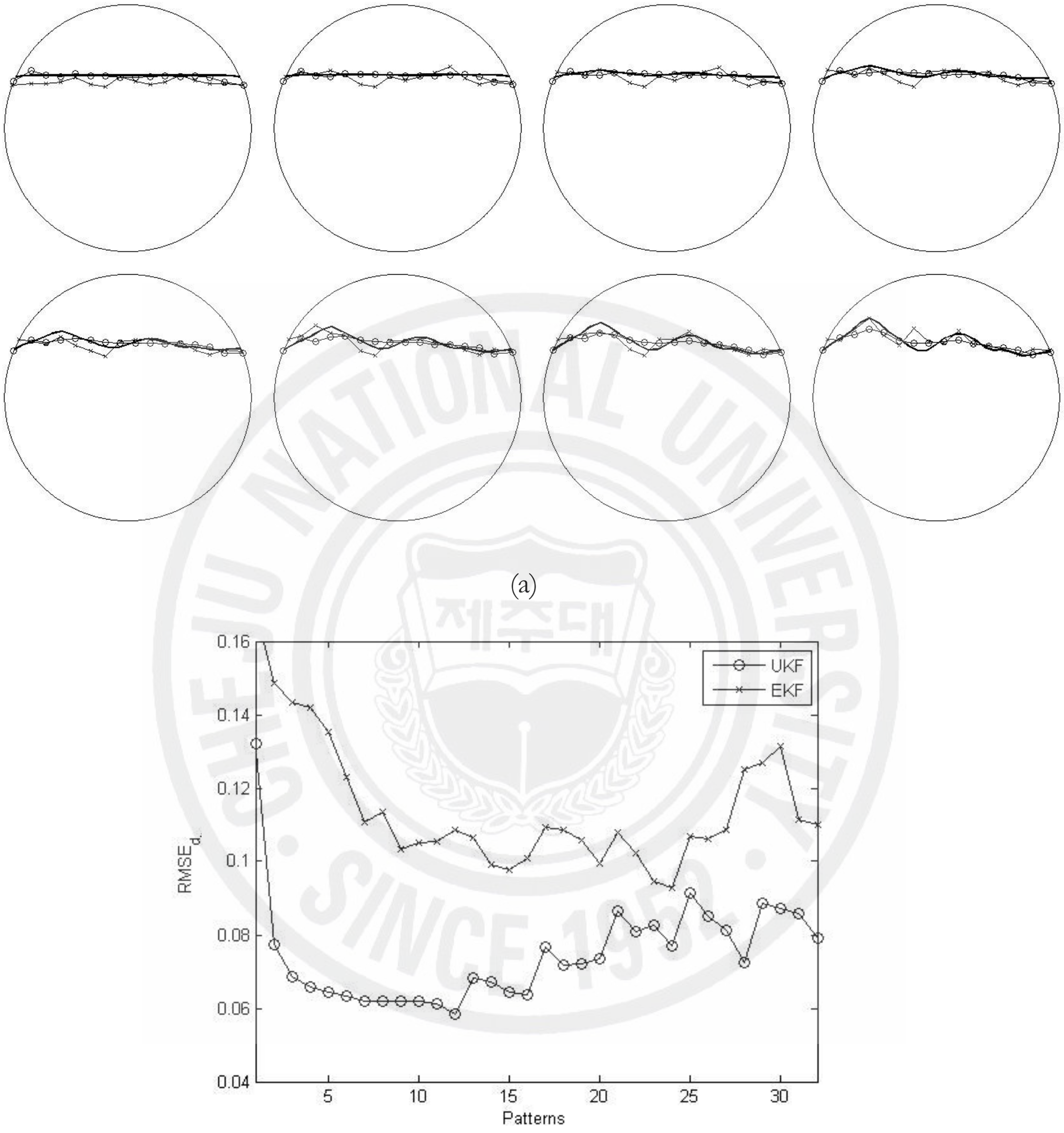
(a)

(b)

Figure 5.31. Results with 16 front points for scenario 4 with 1% noise and contrast ratio of 100:1: (a) reconstructed boundaries after every 4 current pattern. True profile (-), EKF (-x-), and UKF (-o-); (b) RMSE comparison between EKF and UKF.

6 GAUSS-NEWTON UNSCENTED KALMAN FILTER APPROACH TO NONSTATIONARY PHASE BOUNDARY ESTIMATION

Recently, it was discovered that the measurement updates of EKF and UKF are algebraically equivalent to a single iteration of the online Gauss-Newton method for solving the nonlinear least squares problem. However, for nonlinear problems, the measurement updates of EKF and UKF that do not iterate cannot be expected to achieve the maximum likelihood solution, especially, in the case of significant nonlinearity in measurement function. However, the iterative methods are provably convergent and have a rich convergence theory (Dennis JE and Schnabel 1996). Fortunately, one can easily extend the measurement updates of EKF and UKF to Gauss-Newton iterative measurement updates. The resulting new methods are called Gauss-Newton EKF and Gauss-Newton UKF respectively (Bell and Cathey 1993, Van der Merwe 2004, Sibley *etal.* 2006).

Compared to Gauss-Newton EKF, the Gauss-Newton UKF (GNUKF) removes the requirement to analytically calculate Jacobians in both time and measurement updates. Therefore, in this section GNUKF is used as an inverse solver as an improvement over UKF. For the sake of simplicity we assume additive white Gaussian noise in both process and measurement model.

6.1 Gauss-Newton unscented Kalman filter

We assume the state-space model as follows:

$$x_k = F_{k-1} x_{k-1} + w_{k-1} \tag{6.1}$$

$$V_k = U_k(x_k) + v_k \tag{6.2}$$

where $w_k \in \mathbb{R}^{N \times 1}$ and $v_k \in \mathbb{R}^{L \times 1}$ are assumed to be white Gaussian noise with covariances $Q_k = E[w_k w_k^T]$ and $R_k = E[v_k v_k^T]$, respectively. Also, $U_k(\boldsymbol{x}_k)$ is the forward solver to obtain boundary voltages. In the previous chapter, the augmented form of state-vector was assumed by including process noise and measurement noise vector. However, a much simpler version of UKF can also be derived which precludes the need of using augmented form.

Most of GNUKF is similar to conventional UKF. Firstly, the UKF time update is performed, which uses the sigma-point technique to select from the distribution on x_{k-1} a set of sigma points, $\{\chi_i\}_{i=0}^{2N_s}$ where N_s is the dimension of state vector. The sigma points are then assigned different weights, $\left\{W_i^{(m)}, W_i^{(c)}\right\}_{i=0}^{2N_s}$. The sigma points are selected to lie on the principle component axes of the covariance $C_{x_{k-1}}$, plus one extra point for the mean $\bar{x}_{k-1}$ of the distribution:

$$\chi_0 = \bar{x}_{k-1} \tag{6.3}$$

$$\gamma_s = \sqrt{N_s + \lambda_s} \tag{6.4}$$

$$\chi_i = \bar{x}_{k-1} + (\gamma_s \sqrt{C_{x_{k-1}}})_i \quad i = 1, \ldots, N_s \tag{6.5}$$

$$\chi_i = \bar{x}_{k-1} - (\gamma_s \sqrt{C_{x_{k-1}}})_i \quad i = N_s + 1, \ldots, 2N_s \tag{6.6}$$

$$W_o^{(m)} = \frac{\lambda_s}{N_s + \lambda_s} \tag{6.7}$$

$$W_o^{(c)} = \frac{\lambda_s}{N_s + \lambda_s} + (1 - \alpha_s^{\,2} + \beta_s) \tag{6.8}$$

$$W_i^{(m)} = W_i^{(c)} = \frac{1}{2(N_s + \lambda_s)} \quad i = 1, \ldots, 2N_s \tag{6.9}$$

where γ_s is a scaling parameter and $\lambda_s = \alpha_s^{\,2}(N_s + \kappa_s) - N_s$. The typical values of parameters α_s, β_s, and κ_s are set to 10^{-3}, 2, and 0, respectively.

These sigma points are then propagated through the state transition function (6.1) which is identity matrix here considering the random-walk model. The propagated sigma points are then combined with associated weights to produce the predicted state and covariance, i.e.,

$$\chi_k^{*(i)} = F_k \chi_i \quad i = 0, \ldots, 2N_s \tag{6.10}$$

$$\hat{x}_k = \sum_{i=0}^{2N_s} W_i^{(m)} \chi_k^{*(i)} \tag{6.11}$$

$$\hat{C}_{x_k} = \sum_{i=0}^{2N_s} W_i^{(c)} [\chi_k^{*(i)} - \hat{x}_k][\chi_k^{*(i)} - \hat{x}_k]^T + Q_k \tag{6.12}$$

In order to incorporate the effect of the process noise on the sigma points, we redraw a new set of sigma points from the Gaussian time-updated covariance $\hat{C}_{x_k}$,

$$\chi_k = \left[\hat{x}_k \quad \hat{x}_k + \gamma_s \sqrt{\hat{C}_{x_k}} \quad \hat{x}_k - \gamma_s \sqrt{\hat{C}_{x_k}} \right] \tag{6.13}$$

Next, the required measurement covariance $\hat{C}_{U_k}$ and cross-correlation covariance $\hat{C}_{x_k U_k}$ are calculated from the weighted sigma points, by

$$\hat{U}_k = \sum_{i=0}^{2N_s} W_i^{(m)} U_k(\chi_k^{(i)}) \tag{6.14}$$

$$\hat{C}_{U_k} = \sum_{i=0}^{2N_s} W_i^{(c)} [U_k(\chi_k^{(i)}) - \hat{U}_k][U_k(\chi_k^{(i)}) - \hat{U}_k]^T \tag{6.15}$$

$$\hat{C}_{x_k U_k} = \sum_{i=0}^{2N_s} W_i^{(c)} [\chi_k^{(i)} - \hat{x}_k][U_k(\chi_k^{(i)}) - \hat{U}_k]^T \tag{6.16}$$

Next, the Gauss-Newton measurement update is considered as

$$x_k^{j+1} = \hat{x}_k + \hat{C}_{x_k U_k} (\hat{C}_{U_k} + R_k)^{-1} (V_k - U_k(x_k^j) - \hat{C}_{x_k U_k}^T \hat{C}_{U_k}^{-1} (\hat{x}_k - x_k^j)) \quad j = 1, 2, \ldots \tag{6.17}$$

Here, $\hat{C}_{x_k U_k} (\hat{C}_{U_k} + R_k)^{-1}$ is the Kalman gain and V_k is the measured voltage data available in each iteration. The GNUKF iteratively updates the current state x_k^j until convergence. After the convergence, the state mean $\bar{x}_k$ is set to x_k^j, and the covariance is updated as

$$C_{x_k} = \hat{C}_{x_k} - \hat{C}_{x_k U_k} (\hat{C}_{U_k} + R_k)^{-1} \hat{C}_{x_k U_k}^T \tag{6.18}$$

If we set $x_k^j = \hat{x}_k$ and do not iterate, the GNUKF reduces to the UKF.

6.2 Numerical results for front points

For the simulation purposes, the front points approach is considered to evaluate the performance of GNUKF. As in the previous section, a stratified flow of two conducting immiscible liquids is considered through a cylindrical pipe of diameter 28*cm* with 16 electrodes of width 2.5*cm* each around its periphery. A total of 32 frames are considered with the contrast of 100:1 for 10 front points shown in Figure 6.1. Here, only one current pattern is considered in each frame. The data generated is then perturbed with 1%, 2%, and 3% white Gaussian noise respectively. For comparison purposes, GNUKF is compared with UKF and the parameters used are shown in Table 6.1.

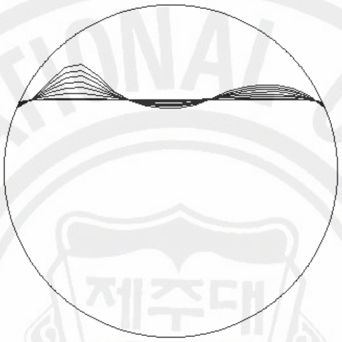

Figure 6.1. Evolution of the interface.

Table 6.1. Parameters used in simulations for both GNUKF and UKF.

	UKF/GNUKF Parameters		
Parameters	1% white Gaussian Noise	2% white Gaussian Noise	3% white Gaussian Noise
Q_k	$0.01\, I_N$	$0.01\, I_N$	$0.01\, I_N$
R_k	$4\times10^3 I_E$	$2\times10^4 I_E$	$3\times10^4 I_E$
C_0	$0.01\, I_N$	$0.01\, I_N$	$0.01\, I_N$
α_s	0.4	0.6	0.6
β_s	2	2	2
κ_s	0	0	0

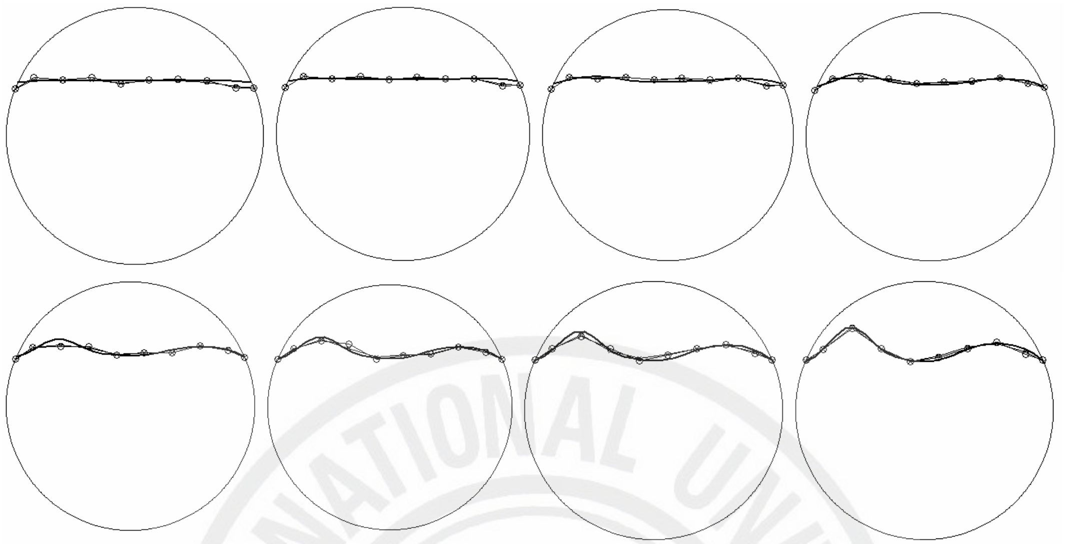

(a)

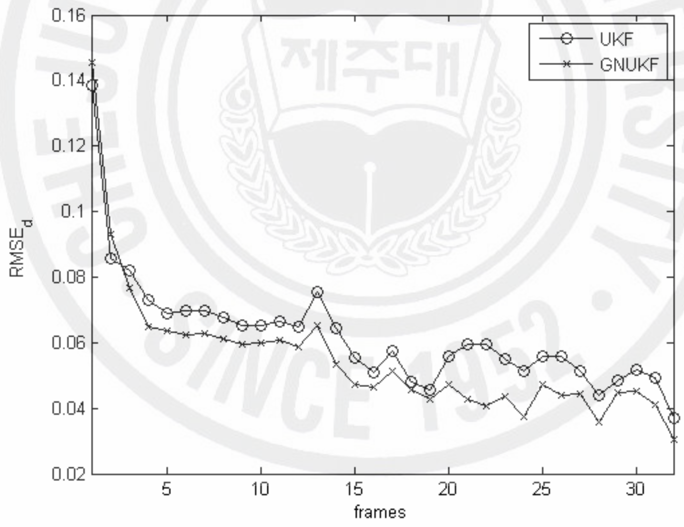

(b)

Figure 6.2. Results for 10 front points with 1% noise and contrast ratio of 100:1: (a) reconstructed boundaries after every 4 current patterns. True profile (-), GNUKF (-x-), and UKF (-o-); (b) RMSE comparison between GNUKF and UKF.

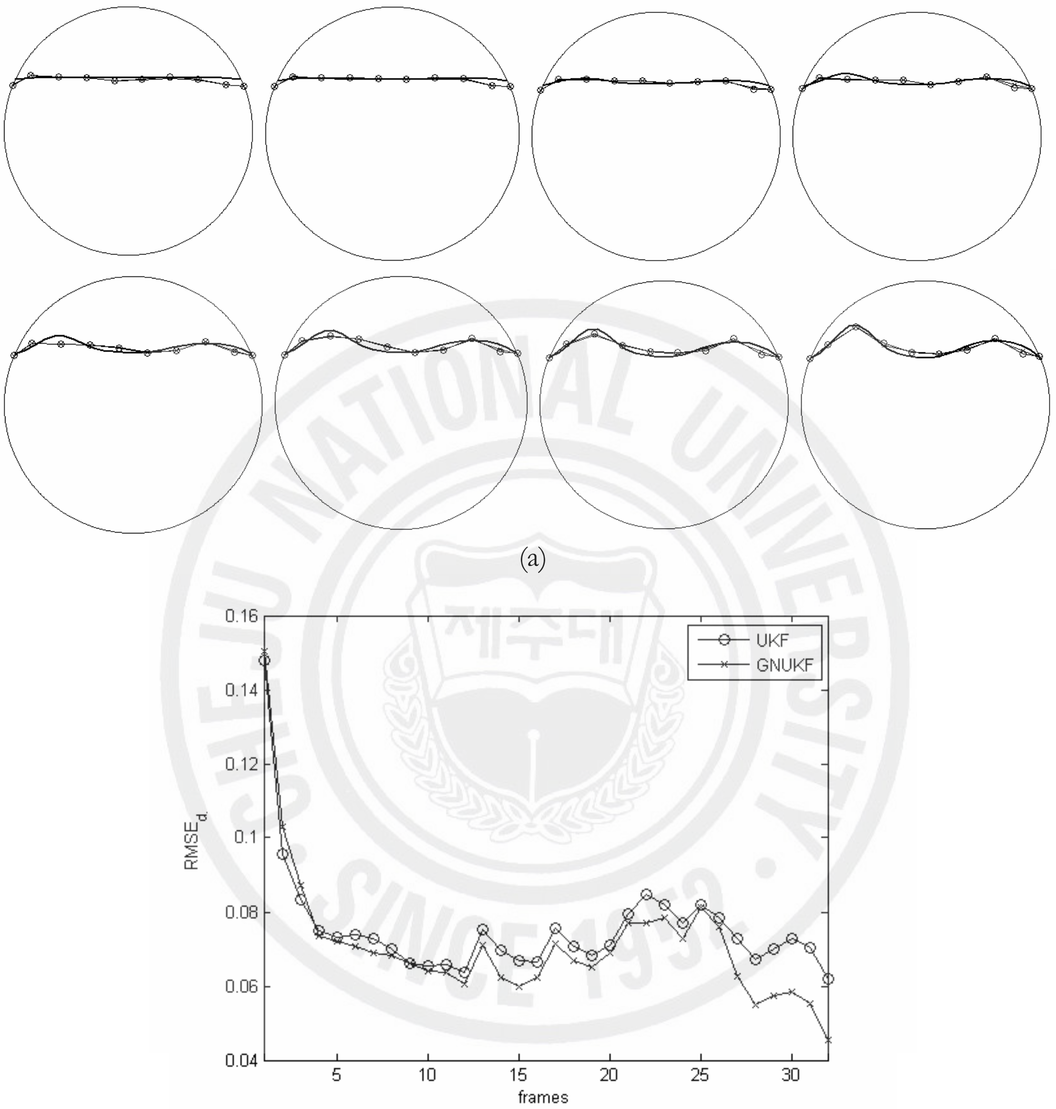

(a)

(b)

Figure 6.3. Results for 10 front points with 2% noise and contrast ratio of 100:1: (a) reconstructed boundaries after every 4 current patterns. True profile (-), GNUKF (-x-), and UKF (-o-); (b) RMSE comparison between GNUKF and UKF.

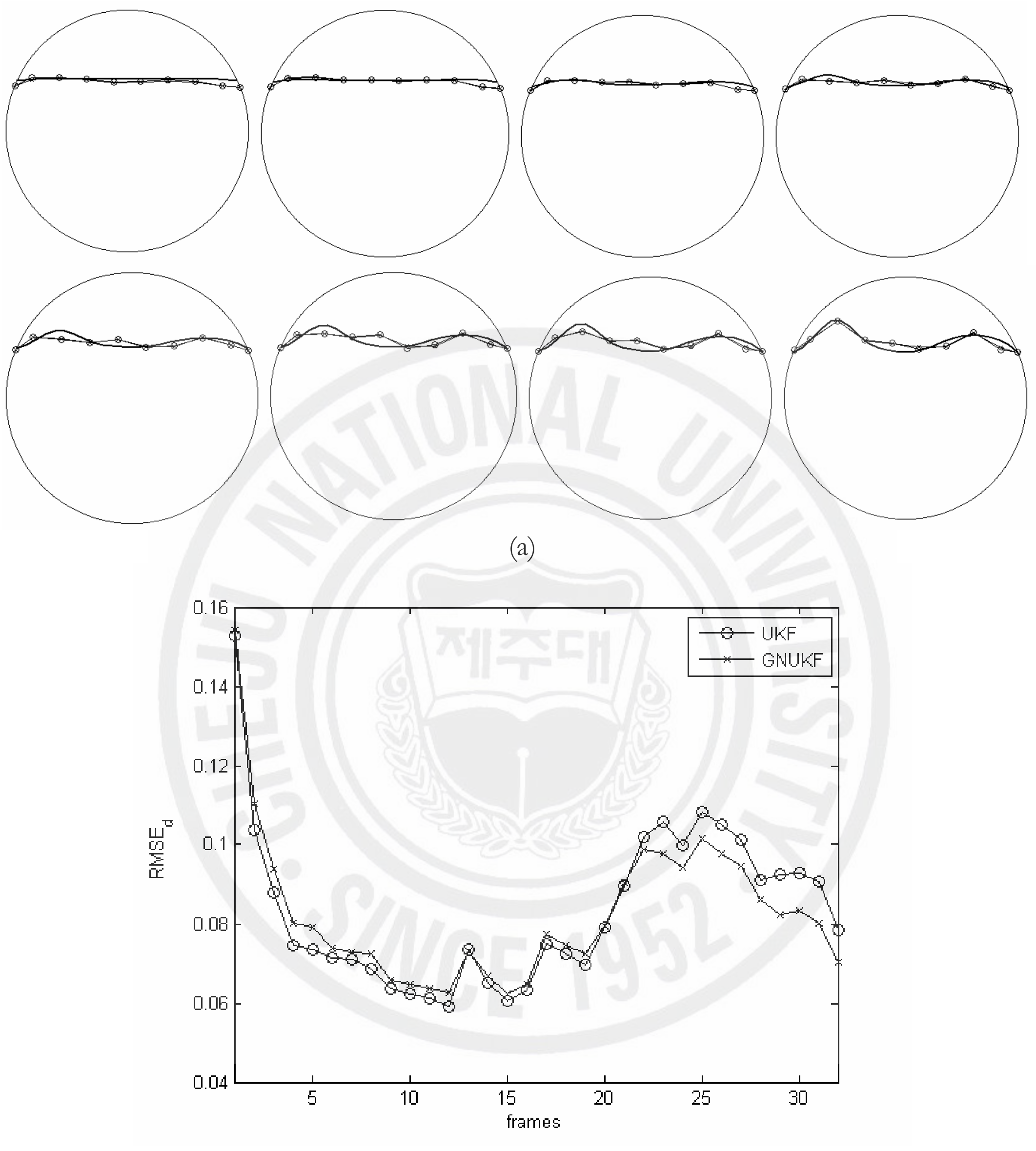

(a)

(b)

Figure 6.4. Results for 10 front points with 3% noise and contrast ratio of 100:1: (a) reconstructed boundaries after every 4 current patterns. True profile (-), GNUKF (-x-), and UKF (-o-); (b) RMSE comparison between GNUKF and UKF.

It should be mentioned here, that for the generation of measurement data, the first two modes of sine and cosine current patterns are used alternatively. For comparison purposes, the RMSE for the parameter *d*, $RMSE_d$, is considered. The simulation results are shown in Figures 6.2-6.4. From the reconstructed results it can be seen that the performance of GNUKF is better than UKF in terms of RMSE, especially in the later part of the simulations, i.e., from 22nd frame to 32nd frame in the case of 1% measurement noise and from 25th frame to 32nd frame in the case of 2% and 3% measurement noise. Since equation (6.17) is iterative in nature, therefore, in order to save some computational burden in the overall process, a much simpler version of UKF is considered which does not use the augmented form and also uses reduced number of sigma points in every iteration. For example, with 10 front points and 16 electrodes configuration, the total number of sigma points generated using augmented approach is 73 sigma points whereas in the current simulations, only 21 sigma points are generated in each iteration.

CONCLUSIONS

In this thesis, electrical impedance tomography (EIT) is introduced for phase boundary recovery. It is assumed that the domain goes through a fast transient change and that the region occupied by each phase or the conductivity distribution is time varying during the time taken to collect a full set of independent measurement data. In order to track the varying interfacial boundary, the interface is parameterized with truncated Fourier coefficients (for closed boundary representation), and discrete front points (for open boundary representation). A special class of EIT inverse problem is addressed, in which the position and shape of the objects were the unknowns to be identified while conductivities (conversely, resistivities) of the objects are known *a priori*. The unknown boundary shape is regarded as a state variable and the EIT problem is transformed into a state estimation problem. Then, the unknown state variables are estimated with the aid of Kalman-type filters. For the verification of the proposed algorithms extensive numerical simulations and experimental studies are performed and computational issues have been discussed. The issues include the avoidance of inverse crime, the calculation of Jacobian, the data collection method, model parameters, the effect of measurement noise, the effect of contrast ratio, and so on.

The IMM based nonstationary boundary estimation technique is proposed which consists of a bank of model-conditioned extended Kalman filters connected in parallel, a model probability evaluator, an estimate mixer at the input of each Kalman filter and an estimate combiner at the output of the parallel filters. Such a configuration is used with different process noise covariances to alleviate the modelling uncertainty of the random-walk model in extended Kalman filter. For the case where one can make a guess on the evolution of interfacial boundary, different kinematic models can be incorporated into the extended Kalman filter. In this thesis, the kinematic models are considered for elliptic region boundary represented with Fourier coefficients. The movement and expansion of an air bubble is considered with constant velocity and constant acceleration. The estimation performance of extended Kalman filter with kinematic model is better than random-walk model in most cases.

By using unscented Kalman filter as an inverse solver, there are several performance gains over conventional extended Kalman filter. In the case of unscented Kalman filter, the mean and covariance of the state estimate is calculated to second order or better as opposed to the first-order in extended Kalman filter, therefore, unscented Kalman filter always gives better results. Also, no analytical Jacobian is required as the key point is unscented transform which uses the measurement equation as such. In the past there were several attempts on more complicated problems in EIT where the internal dynamic equations were difficult to derive, and so inaccurate numerical methods (like perturbation method) were used to derive Jacobian. Unscented Kalman filter generates sigma points and can be computationally intensive, however, the realizable hardware implementation can take advantage of the modern hardware extensions pertaining to vectorization to run some of the code in parallel.

The advantage of Kalman-type filters is that they employ the minimum mean squared error criterion and enable accurate modeling of nonlinear transitions in the boundary interfaces using a limited set of voltage data. They can optimally estimate the boundary interfaces in the presence of noisy voltage data. In this thesis, a 3% relative white Gaussian measurement noise is successfully handled. Furthermore, these algorithms iteratively repeat themselves for each new measurement vector, using only values stored from the previous cycle. Thus, as soon as the voltage data becomes available for a single current pattern, an iteration can be run. This distinguishes itself from batch-processing algorithms, which must save all the data for a current frame consisting of multiple current patterns. With unscented Kalman filter, abrupt changes in boundary interfaces are successfully handled even using voltage data from a single current pattern. Contrast ratio also plays an important role in determining the performance of the reconstruction algorithm. It is generally difficult to handle high contrasts in the target and the background. In this thesis a higher contrast ratio of $10^9:1$ is successfully handled in closed boundary approach and $10^4:1$ is successfully handled in the open boundary approach for given scenarios. These can further increase if the boundary interfaces change slowly or remain static in the application of few current patterns. In this thesis, a smooth elliptic boundary is represented with only 6 Fourier coefficients. With increase in the number of coefficients, a complex shape could also be represented and reconstructed with the Kalman-type algorithms, however, the higher order coefficients are more sensitive to estimation. In the case of front points approach, 16 front points are successfully handled to visualize many ripples in the interface. Thus, it can be concluded that the use of Kalman-type filters as inverse algorithm suggest a practical implication of this research in estimating the fast changes in the interfacial boundaries in industrial processes.

SUMMARY

Electrical impedance tomography is used for boundary estimation in binary mixtures. Two types of problems are considered: open boundary problems in which the object domain can be divided into two disjoint regions which are separated by an open boundary parameterized with front points; and closed boundary problems in which the anomalies are parameterized with truncated Fourier coefficients and are enclosed by the background substance. The finite element method solution of forward problem using complete electrode model is discussed for 2D geometry and is modified as a set of boundary parameters. Also, the analytical Jacobian (linearization of the measurement equation) is derived for both front points and Fourier coefficients approach.

Different types of Kalman-type filters are investigated that can be used as inverse solvers for phase boundary estimation in electrical impedance tomography. Firstly, we use extended Kalman filter to recover the front points that represent the interfacial boundary in stratified flows of two immiscible liquids. After that interacting multiple model algorithm is introduced as an inverse algorithm for the recovery of front points and consists of banks of extended Kalman filter each using different process noise covariance model. Then kinematic models for extended Kalman filter are discussed which are constructed using first- and second-order Markov models. Then, unscented Kalman filter is suggested as an improvement over extended Kalman filter that uses the nonlinear measurement equation and hence does not require the Jacobian. Finally, the Gauss-Newton measurement update in the unscented Kalman filter is employed which improves the performance due to iterative nature of the measurement update. Extensive numerical simulations and experimental results are provided to validate the performance of the above mentioned Kalman-type algorithms and to suggest their practical usage.

REFERENCES

Bar-Shalom Y and Li X R 1993 *Estimation and Tracking: Principles, Techniques and software* (MA: Artech House)

Bell B and Cathey F 1993 The iterated Kalman filter update as a Gauss-Newton method *IEEE Trans. Autom. Control* **38(2)** 294-297

Blom H A P and Bar-Shalom Y 1998 The Interacting Multiple Model Algorithm for Systems with Markovian Switching Coefficients *IEEE Trans. Autom. Control* **33** 780-3

Butler J E and Bonnecaze R T 2000 Inverse method for imaging a free surface using electrical impedance tomography *Chem. Eng. Sci.* **55** 1193-204

Cheney M and Isaacson D 1986 Distinguishability of conductivities by electric current computed tomography *IEEE Trans. Medical Imaging* **5** 91-95

Chung E T, Chan T F and Tai X C 2005 Electrical impedance tomography using level set representation and total variational regularization *J. Comput. Phys.* **205** 357-72

Dennis J E and Schnabel R B 1996 *Numerical methods for unconstrained optimization and nonlinear equations* (Soc for Industrial & Applied Math, NJ: Prentice-Hall, Inc.)

Fairuzov Y V 2000 Numerical simulation of transient flow of two immiscible liquids in pipeline *AIChe J.* **46** 1332-9

Gelb A 1974 *Applied Optimal Estimation* (Cambridge, MA: MIT Press)

Gisser D C, Isaacson D and Newell J C 1988 Theory and performance of adaptive current tomography system *Clinical Physics and Physiological Meas.* **9** 35-42

Gladden L F and Alexander P 1996 Application of nuclear magnetic resonance imaging in process engineering *Meas. Sci. Technol.* **7** 423-435

Han D K and Prosperetti A 1999 A shape decomposition technique in electrical impedance tomography *J. Comput. Phys.* **155** 75-95

Holand F A and Bragg R 1995 *Fluid Flow for Chemical Engineers* (London: Edward Arnold Publisher)

Isaacson D 1988 Distinguishability of conductivities by electric current computed tomography *IEEE Trans. Medical Imaging* **M1-5** 91-95

Jeon H J, Kim J H, Choi B Y, Kim K Y, Kim M C, and Kim S 2005 Electrical Impedance Imaging of Binary Mixtures with Boundary Estimation Approach Based on Multilayer Neural Network *IEEE Sensors Journal* **5(2)** 313-319

Jones O C, Lin J T, Ovacik L and Shu H 1993 Impedance imaging relative to gas-liquid systems *Nucl. Eng. Des.* **141** 159-176

Julier S J and Jeffery K U 1997 A New Extension of the Kalman Filter to nonlinear Systems. In *The Proceedings of AeroSense: The 11th International Symposium on Aerospace/Defense Sensing, Simulation and Controls, Multi Sensor Fusion, Tracking and Resource Management* II, SPIE.

Julier S J and Uhlmann J K 2004 Unscented filtering and nonlinear estimation *Proceedings of the IEEE* **92(3)** 401-422.

Kim M C, Kim S and Kim K Y 2004 Estimation of phase boundaries in two-phase systems by electrical impedance tomography technique *J. Ind. Eng. Chem.* **10** 710-716

Kim M C, Kim K Y and Kim S 2005 Improvement of impedance imaging for two-phase systems with boundary estimation approach in electrical impedance tomography *The Canadian Journal of Chemical Engineering* **83** 55-63

Kim K Y, Kim B S, Kim M C, Lee Y J, Vauhkonen M 2001 Image reconstruction in time-varying electrical impedance tomography based on the extended Kalman filter *Meas. Sci. Technol.* **12** 1-8

Kim B S, Ijaz U Z, Kim J H, Kim M C, Kim and Kim K Y 2007 Nonstationary phase boundary estimation in electrical impedance tomography based on the interacting multiple model scheme *Meas. Sci. Technol.* **18** 62-70

Kim J H, Kang B C, Choi B Y, Kim M C, Kim S and Kim K Y 2006a Phase boundary estimation in electrical resistance tomography with weighted multilayer neural networks *IEEE Transaction on Magnetics* **42(4)** 1191-1194

Kim M C, Kim S, Kim K Y, Seo K H, Jeon H J, Kim J H and Choi B Y 2006b Estimation of phase boundary by front points method in electrical impedance tomography *Inverse Problems Sci. Eng.* **14** 455-66

Kim J H, Kang B C, Lee S H, Choi B Y, Kim M C, Kim B S, Ijaz U Z, Kim K Y and Kim S 2006c Phase boundary estimation in electrical resistance tomography with weighted multi-layered neural networks and front point approach *Meas. Sci. Technol.* **17** 2731-2739

Kim S, Ijaz U Z, Khambampati A K, Kim K Y, Kim M C, and Chung S I 2007 Moving interfacial boundary estimation in stratified flow of two immiscible liquids using electrical resistance tomography *Meas. Sci. Technol.* **18** 1257-1269

Kolehmainen V, Arridge S R, Lionheart W R B, Vauhkonen M and Kaipio J P 1999 Recovery of region boundaries of piecewise constant coefficients of elliptic PDE from boundary data *Inverse Problems* **15** 1375-91

Kolda T G, Lewis R M and Torczon V 2003 Optimization by direct search: new perspectives on some classical and modern methods *SIAM REVIEW*, **45(3)** 385-482

Kortschak B and Brandstätter B 2005 A FEM-BEM approach using level-sets in electrical capacitance tomography *COMPEL* **24** 591-605

Kwon O, Yoon J R, Seo J K and Woo E J 2003 Estimation of Anomaly Location and Size using Electrical Impedance Tomography *IEEE Transactions on Biomedical Engineering* **50(1)** 2003

Lionheart W R B 2004 EIT reconstruction algorithms: pitfalls, challenges and recent developments *Physiol. Meas.* **23** 125-42

Mazor E, Averbuch A, Bar-Shalom Y and Dayan J 1998 Interacting multiple model methods in target tracking: a survey *IEEE Trans. Aerosp. Electron. Syst.* **34** 103-23

Minhas A S and Reddy M R 2005 Neural network based approach for anomaly detection in the lungs region by electrical impedance tomography *Physiol. Meas.* 26 489-502

Newell J C, Gisser D C and Isaacson D 1988 An electric current tomograph *IEEE Trans. Biomed. Eng.* **35** 823-833

Nunez P L 1981 *Electric fields of the brain: the neurophysics of EEG* (New York: Oxford University Press)

Perry R H, Green D W,and Maloney J O 1997 *Perry's Chemical Engineers Handbook* (New York: McGraw-Hill)

Shollenberger K A, Torczynski J R, Adkin D R, O'hern T J and Jackson N B 1997 Gamma-densitometry tomography of gas holdup spatial distribution and industrial-scale bubble colum *Chem. Eng. Sci.* **52** 2037-2048

Sibley G, Sukhatme G and Matthies L 2006 The iterated sigma point kalman filter with applications to long range stereo. In *Proceedings of Robotics: Science and Systems*, Philadelphia, USA

Simon D and Chia T 2002 Kalman Filtering with State Equality Constraint *IEEE Transactions on Aerospace and Electronic Systems* **39** 128-136

Somersalo E, Cheney M and Isaacson D 1992 Existence and uniqueness for electrode models for electric current computed tomography *SIAM Journal on Applied Mathematics* **52** 1023-1040

Shumway R H and Stoffer D S 1982 An Approach to Time Series Smoothing and Forecasting using the EM Algorithm *Journal of time series analysis* **3(4)** 253-263

Tossavainen O-P, Kolehmainen V and Vauhkonen M 2006 Free-surface and admittivity estimation in electrical impedance tomography *Int. J. Numer. Meth. Eng.* **66** 1991-2013

Tossavainen O P, Vauhkonen M, Kolehmainen V and Kim K Y 2006 Tracking of moving interfaces in sedimentation processes using electrical impedance tomography *Chemical Engineering Journal* **61** 7717-7729

Tossavainen O-P, Vauhkonen M, Heikkinen L M and Savolainen T 2004 Estimating shape and free surfaces with electrical impedance tomography *Meas. Sci. Technol.* **15** 1402-1411

Trelea I C 2003 The particle swarm optimization algorithm: convergence analysis and parameter selection *Information Processing Letters* **85** 317-325

Trigo F C, Gonzalez-Lima R and Amato M B P 2004 Electrical impedance tomography using the extended Kalman filter *IEEE Trans. Biomed. Eng.* **51** 72-81

Van der Merwe R and Wan E R 2001 The square-root unscented Kalman filter for state and parameter estimation In *The Proceedings of ICASSIP'01: 2001 IEEE International Conference on Acoustics, Speech, and Signal Processing,* Salt Lake City, UT, USA

Van der Merwe R 2004 Sigma-point Kalman filters for probabilistic inference in dynamic state-space models *PhD Thesis* OGI School of Science & Engineering, Oregon Health & Science University, USA

Vauhkonen M 1997 Electrical impedance tomography and prior information *PhD Thesis* University of Kuopio, Finland

Vauhkonen M, Karjalainen P A and Kaipio J P 1998a A Kalman filter approach to track fast impedance changes in electrical impedance tomography *IEEE Trans. Biomed. Eng.* **45** 486-493

Vauhkonen M, Vadász D, Karjalainen P, Somersalo E and Kaipio J P 1998b Tikhonov regularization and prior information in electrical impedance tomography *IEEE Transactions on Medical Imaging* **17** 285-293

Vauhkonen M, Lionhart W R B, Heikkinen L M, Vauhkonen P J and Kaipio J P 2001 A MATLAB package for the EIDORS project to reconstruct two-dimensional EIT images *Physiol. Meas.* **22** 107-111

Webster J G 1990 *Electrical Impedance Tomography* (Bristol: Hilger)

Yorkey T J, Webster J G and Tompkins W J 1988 Comparing reconstruction algorithms for electrical impedance tomography *IEEE Trans. Biomed. Eng.* **34** 843-52

Xu L, Han Y, Xu L A and Yang J 1997 Application of ultrasonic tomography to monitoring gas/liquid flow *Chem. Eng. Sci.* **52** 2171-2183